Modeling of Amoeboid Swimming at Low Reynolds Number

A DISSERTATION
SUBMITTED TO THE FACULTY OF THE GRADUATE SCHOOL
OF THE UNIVERSITY OF MINNESOTA
BY

Qixuan Wang

IN PARTIAL FULFILLMENT OF THE REQUIREMENTS
FOR THE DEGREE OF
Doctor of Philosophy

Hans G. Othmer

August, 2012

Acknowledgements

I would like to express my most sincere gratitude and appreciation to my thesis adviser, Professor Hans G. Othmer for his invaluable guidance, inspiration, patience and support through these years of my PhD study. I would like to thank Dr. Mark P. Curtis, Dr. Weiwei Wu, Professor Eamonn A. Gaffney, Professor Tianjun Li and Professor Yoichiro Mori for their discussion and help throughout the process. I would like to thank all the members of Hans Othmers group for their comments and support.

Dedication

To my parents and my husband.

Abstract

Cells adopt various strategies to migrate across 2D substrates or through 3D extracellular matrix. Recently it is reported that fibroblast cells and Dictyostelium amoebae can swim in low Reynolds number fluids by rapid shape deformations. We are interested in the question: "how do shape deformations of the cell translate into locomotion through the fluid"?

In this dissertation we first introduce a mechanical model inspired by a particular biological phenomenon called "blebbing". We try to mimic the processes of mass transportation among the cell body and multiple blebs in our model, and illustrate that such processes may lead to locomotion in low Reynolds number Newtonian fluids. We start from linear models then move on to planar ones, examine the rigid motions and efficiency resulted from prescribed shape deformations. While in experiments it is observed that multiple blebbing may lead to an oscillatory motion, we predict that if shape deformations are coordinated appropriately they could actually result in directed motion. Later we try to apply these models to a linear viscoelastic fluid, and as a starting point we discuss the mechanics of a translating deformable sphere in a linear viscoelastic fluid.

We also investigate the swimming behavior of Dictyostelium amoebae that swim by initiating traveling protrusions. We use techniques of complex analysis to build up 2D models which allow us to study the cell-fluid interaction. We simulate the swimming processes of observed swimming Dictyostelium amoebae, and discuss how the slenderness of the cell body and the shapes of the protrusion effect the swimming of the Dictyostelium cell. Moreover, we examine a large variety of mathematically prescribed general symmetric shape deformations, from which we observe certain intrinsic behaviors in low Reynolds number swimming. Such observations provide us with potential necessary conditions in optimal swimming, which may give us guidance in designing low Reynolds number swimming models.

Contents

List of Tables

List of Figures

Chapter 1

Introduction

1.1 Migration of amoeboid cells

Cell locomotion is crucial in many biological process. There are two basic modes of cell locomotion, one is usually referred to as "walking" or "crawling" which depends strongly on the attachment to some substrate or the tissue network, i.e., the extracellular matrix (ECM) [3, 4, 5] and sometimes even on the degradation of the ECM as well [6, 7], the other is usually referred to as "swimming", during which the cell propels itself by deforming its body in a periodic way through a viscous or viscoelastic fluid environment. In fact, the "swimming" mode is not a privilege for cells only, and such mode have been studied a lot for various ciliated microorganisms: sperms use one flexible filament [8], *E. coli* run or tumble by rotation of flagella bundles [9, 10], and some single-cell microorganism swims by coordinately beating a thin layer of cilia [11, 12], etc.

To date, most mathematical studies of cell locomotion have been focused on the "swimming" by flagella or cilia mode and the "crawling" mode. Yet recently it is observed from experiments that some tumor cells and a number of eukaryotic cells without flagella or cilia could still migrate using an amoeboid mode through the ECM or even in liquid when adhesion is reduced or removed that disables crawling. Evidence for amoeboid migration through the ECM includes the "mesenchymal-to-amoeboid transition" for tumor cells [14, 15], dendritic cells without integrins squeezing themselves through the ECM [16], zebrafish primordial germ cells undergoing a series of morphological changes which allows them to respond to attractive cues [17, 18], etc. Figure 1.1

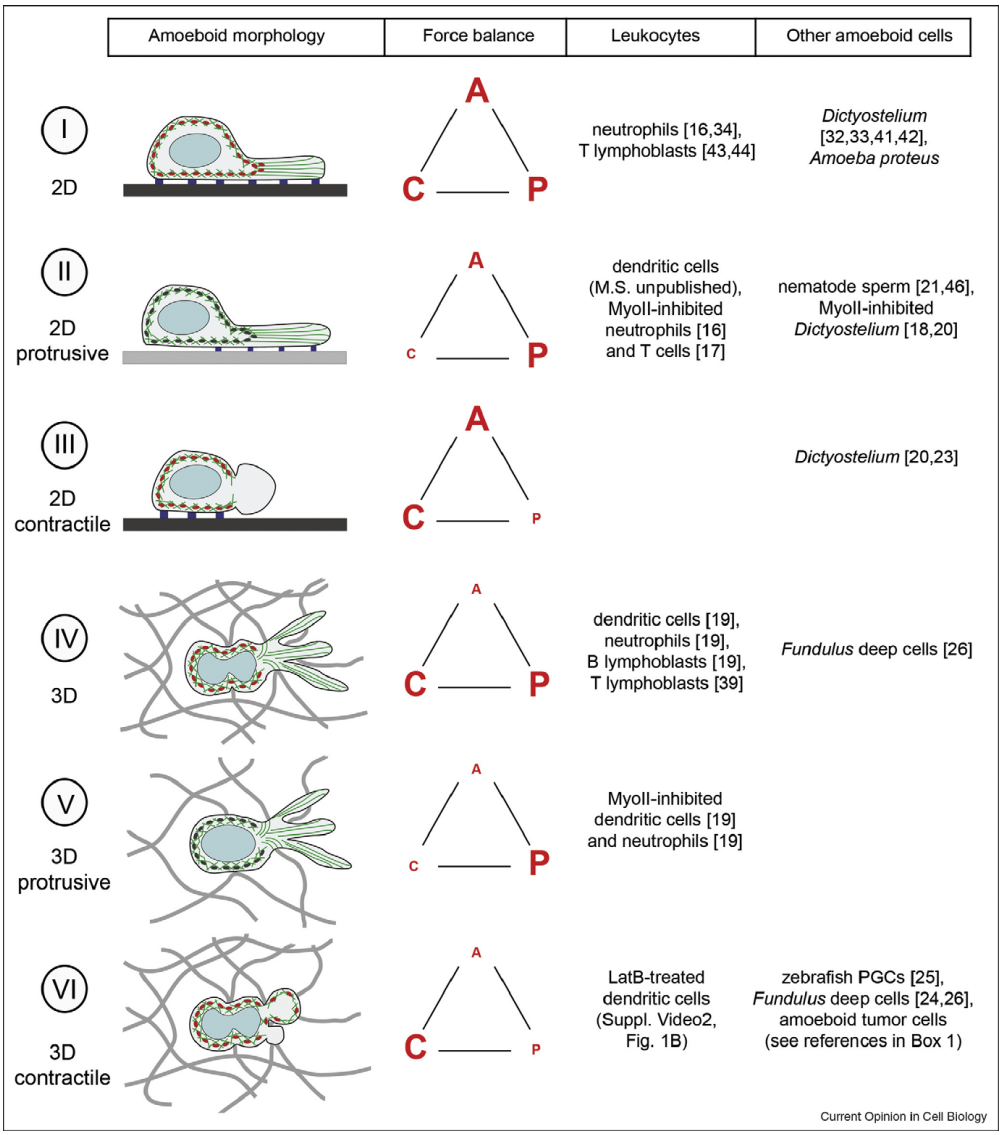

Figure 1.1: Amoeboid modes on 2D substrate and in 3D ECM [13].

[13] presents a summary of the amoeboid migration modes on a 2D substrate and in 3D ECM.

Yet there is one mode missing from Figure 1.1, that is, the amoeboid swimming mode. In this mode large amoeboid-like protrusions are usually involved, and unlike the other amoeboid migration modes shown in Figure 1.1, here there is no attachment or interaction with any substrate or network, motility only comes from the interaction with the surrounding fluid. In [19] it is reported that freely suspended Swiss-3T3 fibroblast cells without cell-substrate adhesion may exhibit oscillatory shape dynamics, and some of them may also exhibit periodic bleb dynamics correlating with the oscillations, where blebs are hemispherical membrane blisters induced by cortical contraction [20, 21]. Such a combination of both dynamics may result in a random oscillation of the cell in space. Similar oscillatory motions can also be observed in the cellular apoptosis process, in which usually multiple blebbing are involved. In comparison with such random motion, Dictyostelium and neutrophils may adopt amoeboid swimming mode so to achieve directed movement toward chemoattractant with a similar speed to that of walking [2, 22, 1]. While in the fibroblast cells, the cell is more rounded with multiple blebs pervaded on the cell surface as shown in Figure 1.2 (a), in Dictyostelium amoebae the cell body is elongated and only $1-3$ protrusions are observed as shown in Figure 1.2 (b), and they can move down the length of the elongated cell which provides the drag force needed for the directed movement [2]. We are interested in the amoeboid swimming mode and our object is to discover how the amoeboid deformation of the cell translates into migration.

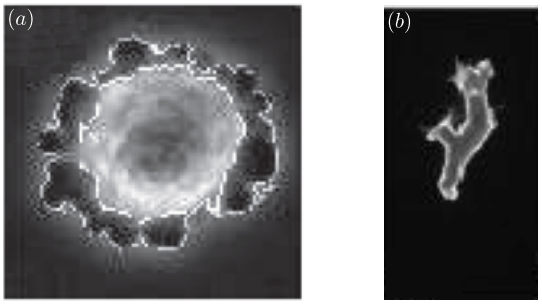

Figure 1.2: Amoeboid swimming cells: (a) fibroblast cells showing both shape oscillations and blebbing [19]; (b) the shape of a swimming Dictyostelium [2].

1.2 Mechanics of swimming at low Reynolds number

We briefly discuss the mechanics for flows at low Reynolds number, for more details we refer to [23, 24, 25, 26]. Also we refer to [27] for a detailed review of the current state of knowledge of low Reynolds number swimming microorganisms.

Suppose that an organism swims in an incompressible Newtonian fluid with density ρ and viscosity μ, then the mechanics of the fluid is governed by the Navier-Stokes equations

$$\rho\Big(\frac{\partial}{\partial t} + \mathbf{u}\cdot\nabla\Big)\mathbf{u} = -\nabla p + \mu\nabla^2\mathbf{u}, \qquad \nabla\cdot\mathbf{u} = 0 \tag{1.1}$$

where $\mathbf{u}$ is the velocity field of the fluid and p the pressure. For a steady flow with characteristic length scale L and velocity scale U, the Reynolds number is a dimensionless quantity defined as $Re = \rho LU/\mu$. In the large Reynolds number regime inertia dominates, while at low Reynolds number, the effects of inertia can be ignored and viscosity dominates. As for swimming Dictyostelium amoebae as we mentioned in Section 1.1, they swim with $U \sim 3\mu$m/min with a typical length $L \sim 25\mu$m [1], we consider them swimming in water ($\rho \sim 10^3$kg m^{-3}, $\mu \sim 10^{-3}$Pa s) and therefore $Re \sim O(10^{-6})$. In such a regime, the Navier-Stokes equations 1.1 reduce to the linear Stokes equations

$$-\nabla p + \mu\nabla^2\mathbf{u} = 0, \qquad \nabla\cdot\mathbf{u} = 0 \tag{1.2}$$

Suppose that at time t, the microorganism occupies a simply-connected compact region $\Omega = \Omega(t)$ in $\mathbb{R}^2$ or $\mathbb{R}^3$ and is immersed in an infinite fluid domain, and so the corresponding fluid domain should be $\Omega(t)^c = \mathbb{R}^2/\Omega(t)$ or $\mathbb{R}^3/\Omega(t)$ with the boundary given by $\partial\Omega(t)$. The hydrodynamic force $\mathbf{F}$ and torque $\mathbf{T}$ acting on the body are given by

$$\mathbf{F}(t) = \int_{\partial\Omega(t)} \sigma\cdot\mathbf{n}\, dS, \qquad \mathbf{T}(t) = \int_{\partial\Omega(t)} \mathbf{x}\times\big(\sigma\cdot\mathbf{n}\big)\, dS \tag{1.3}$$

where $\mathbf{x}\in\partial\Omega(t)$ and $\mathbf{n}$ is the outward unit vector on $\partial\Omega(t)$, and σ is the stress tensor given by

$$\sigma = -p\mathbf{I} + \mu\big[\nabla\mathbf{u} + \big(\nabla\mathbf{u}\big)^T\big] \tag{1.4}$$

with $\mathbf{I}$ the identity tensor. At low Reynolds number, Newton's law can be expressed as

$$\mathbf{F}_{\text{ext}} + \mathbf{F} \equiv 0, \qquad \mathbf{T}_{\text{ext}} + \mathbf{T} \equiv 0 \tag{1.5}$$

where $\mathbf{F}_{\text{ext}}$ and $\mathbf{T}_{\text{ext}}$ stand for the external force and torque. As for microorganism swimming problems, as we mentioned in Section 1.1, the microorganism is self-propelled. Moreover, we are considering an infinite fluid domain without any wall or boundary, hence there are no external forces or torques, which indicates that $\mathbf{F}_{\text{ext}} \equiv 0$ and $\mathbf{T}_{\text{ext}} \equiv 0$. Thus equations (1.5) reduce to

$$\mathbf{F} \equiv 0, \qquad \mathbf{T} \equiv 0 \tag{1.6}$$

In the following discussion, we will refer to the $\mathbf{F} \equiv 0$ condition as the *force-free condition*, and $\mathbf{T} \equiv 0$ as the *torque-free condition*.

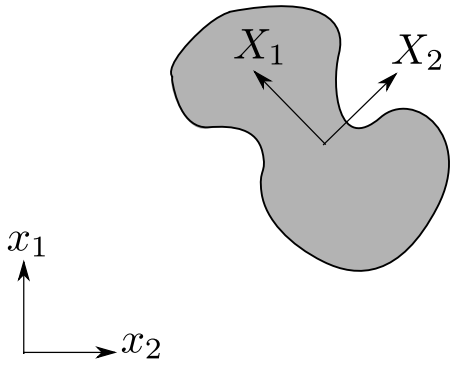

Figure 1.3: 2D illustration of reference frame $(\mathbf{x}, t)$ and body frame $(\mathbf{X}, t)$

We consider a fixed global reference frame $(\mathbf{x}, t)$ and a body frame $(\mathbf{X}, t)$ attached to the microswimmer as shown in Figure 1.3 for a 2D example, where t measures time and it is scaled the same in both frames. For the shape deformations of the microswimmer, when observed from the body frame, they can be described by the velocity field along its boundary surface: $\mathbf{u}_{\text{shape}}(\mathbf{X}, t)$ for $\mathbf{X} \in \partial\Omega_{\mathbf{X}}(t)$, where we use $\partial\Omega_{\mathbf{X}}(t)$ to denote the boundary of the microswimmer when observed in the body frame. Moreover, in low Reynolds number swimming problems we are interested in cyclic shape deformations, i.e., $\mathbf{u}_{\text{shape}}(\mathbf{X}, t)$ should be periodic with respect to t. Due to the fluid-structure interaction, shape deformations of the microorganisms may result in rigid motions of the microswimmer with velocity $\mathbf{U}(t)$ and rotation rate $\mathbf{\Omega}(t)$ when observed from the global frame. Hence the instantaneous velocity on the swimmer's surface $\partial\Omega(t)$ (observed from the body frame) should be

$$\mathbf{u} = \mathbf{U} + \mathbf{\Omega} \times \mathbf{x} + \mathbf{u}_{\text{shape}} \tag{1.7}$$

and $\mathbf{u}$ should satisfy equation (1.6).

A *swimming stroke* is specified by a time-dependent sequence of shapes, and it is *cyclic* if the initial and final shapes are identical. A canonical low Reynolds number swimming problem can be described as follows: given a cyclic swimming stroke by specifying $\mathbf{u}_{\text{shape}}$ along the boundary $\partial\Omega_{\mathbf{X}}$ of the microswimmer, solve the Stokes equations (1.2) for the velocity field $\mathbf{u}$ subject to the force-free and torque-free conditions given by equation (1.6), and then obtain $\mathbf{U}$ and $\mathbf{\Omega}$.

To date most of current works related to low Reynolds number swimming are restricted to Newtonian fluids. Yet recently it is argued that "biological fluids are often laden with polymers and therefore have non-Newtonian rheology" [27]. Hence we need to consider complex fluids and we start by considering a viscoelastic fluid in Chapter 4.

1.3 Historical studies

Our object is to discover how shape deformations translate into locomotion. We notice that time does not appear in the Stokes equations (1.2) explicitly, which indicates that in the low Reynolds number regime the net rigid motions resulted from a cyclic stroke is independent of the rate at which the stroke is executed [28]. This naturally leads to the famous "scallop theorem" which can be generalized as: at low Reynolds number, a time-reversible stroke produces no net motion. This principal was first advanced by Purcell in [28], where he illustrated the idea using a simple example of a scallop who has only one degree of freedom (opening or closing the shell), hence naturally it could only deform itself in a time-reversible fashion. Purcell demonstrated that a scallop could not swim at low Reynolds number, though it is well known that such mechanism indeed results in net motion at high Reynolds number [28].

Since the rigid motions that result from a sequence of shape deformations do not depend on the rate at which the swimmer is deformed, but only on the geometrical sequence of shape, the low Reynolds number swimming problem can be addressed as a pure geometrical problem. The gauge theoretic nature of this problem was first addressed by Shapere and Wilczek [29, 30]. Application of gauge theory to low Reynolds number swimming problems can be found in [29, 30, 31] involving analysis of some simple examples. Later Alouges *et.al.* combine gauge theory with modern numerical

methods that allows them to successfully analyze the optimization problems for a variety of designed low Reynolds number swimming models [32, 33, 34, 35]. For more discussion of the geometric structure of low Reynolds number swimming problems, we refer to [36, 37, 38, 39, 40].

However we are more interested in studying the detailed behavior of real biological microswimmers, rather than the general abstract mathematical principal behind swimming. To date, a lot has been done for microorganisms swimming by a single thin long flagella, including the development of *slender-body theory* [41, 42, 43, 44, 45, 46, 47]. Microorganisms that swim using a thin layer of cilia were first studied by Lighthill for squirming motion of nearly spherical deformable bodies [48] and later corrected by Blake [49], together with a parallel study of the cylindrical case [50]. Since then, a lot of mechanical and mathematical low Reynolds number swimming models have been developed and investigated so to help us in both understanding the swimming behavior of a variety of microorganisms and designing mini-robots that swim at low Reynolds number. The first low Reynolds number model is *Purcell's two-hinge swimmer*, sometimes also referred to as *Purcell's three-link swimmer* [28] (Figure 1.4 (a)). Despite its simple geometry, the mechanics of Purcell's three-link swimmer interacting with a surrounding viscous fluid is very complicated [51, 52]. Later a large family of linked-spheres models were proposed and analyzed. Due to the advantage that both their geometry and mechanics are easy to deal with, we can easily obtain both analytical and computational results that greatly help us understand the low Reynolds number swimming problems. The first linked-spheres model is *Golestanian's three linked spheres model* [53, 54, 55] (Figure 1.4 (b)), which comprises three rigid spheres connected by two slender arms aligned along the x-direction that can stretch and contract in a prescribed form so to produce non-reciprocal motion. Golestanian's three linked spheres model is a linear model and it can only result in translation. A sibling of Golestanian's three linked spheres model is the *generalized Golestanian's three linked spheres model* [56] (Figure 1.4 (c)), whose motions include both translation and rotation. Also there is *Purcell's rotator* [57] (Figure 1.4 (d)) which comprises three spheres and three linked arms, each sphere has one arm connected to the fixed center, and it can result in rotation only. More complicated variations of linked-spheres models include the *pushmepullyou* model [58] (Figure 1.4 (e)) and the *four linked-spheres model* [32] (Figure 1.4 (f)). For

the former, unlike in the other linked-spheres models where the spheres are supposed to be rigid, the pushmepullyou model consists of two spheres that can expand or shrink only in the radial direction, with one connecting arm that can stretch or contract; as for the latter, it is the first model ever designed to swim in 3D space while all the previous ones could only swim along a line or in a plane. There are still several other existing low Reynolds number swimming models like *Najafi's two-sphere low Reynolds' propeller* [59] (Figure 1.4 (g)) and the *stick and donut swimmer* [33] (Figure 1.4 (h)), here we will not go over them in detail.

1.4 Outline of the dissertation

We are interested in the amoeboid swimming of cells and our current work involves modeling, analysis and computation of amoeboid swimming cells. As mentioned in Section 1.1, in experiments we observe two kinds of amoeboid mode swimming: one with a rounded body cell and multiple blebs, which always exhibits a random oscillatory motion (Figure 1.2 (a)); the other has an elongated and polarized cell body with only several side-bumps traveling down the length of the elongated cell resulting in a directed motion (Figure 1.2 (b)).

Our current work basically consists of two parts: the first half (Chapter 2 - Chapter 4) includes construction and analysis of a mechanical model dedicated to the study of the multiple-blebbing mode of swimming, and we show that if we could appropriately arrange the processes of multiple blebbing, the random oscillation could actually be transformed into directed motion; in the second half (Chapter 5 - Chapter 8), we use a combination of classic fluid mechanics and complex analysis so to model the traveling-protrusions mode of swimming in 2D. Part of the first half of this work has been published in [60].

We organize the dissertation as follows:

- In Chapter 2 we develop a linear linked-spheres low Reynolds number swimming model so as to mimic a simple linear case of amoeboid mode swimming involving multiple blebs. In most of the existing linked-spheres models as we introduced in Section 1.3 the length of the connecting arms are allowed to change. However we

(a) Purcell's three-link swimmer

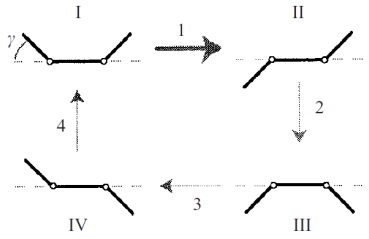

(b) Golestanian's three linked spheres model

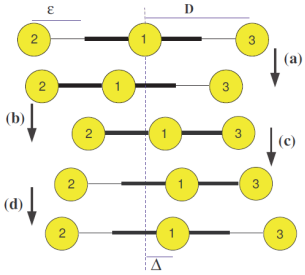

(c) Generalized Golestanian's three linked spheres model

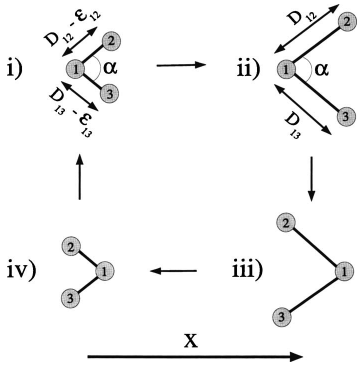

(d) Purcell's rotator

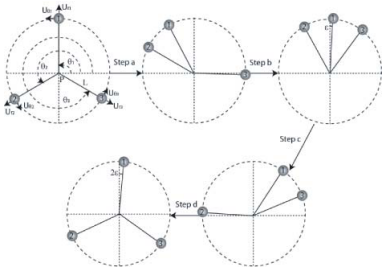

(e) Pushmepullyou

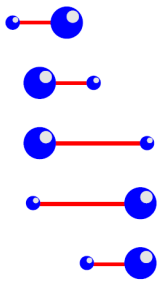

(f) Four linked-spheres model

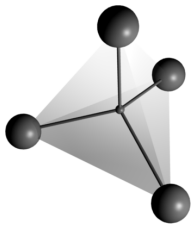

(g) Najafi's two-sphere low Reynolds' propeller

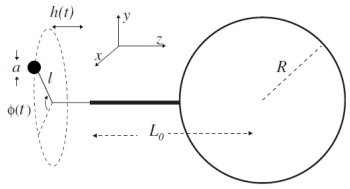

(h) Stick and donut swimmer

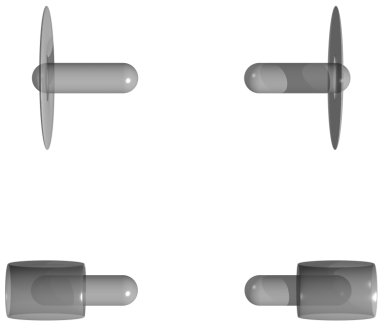

Figure 1.4: Low Reynolds number swimming models: (a) Purcell's three-link swimmer [28]; (b) Golestanian's three linked spheres model [53]; (c) generalized Golestanian's three linked spheres model [56]; (d) Purcell's rotator [57]; (e) pushmepullyou [58]; (f) four linked-spheres model [32]; (g) Najafi's two-sphere low Reynolds' propeller [59]; (h) stick and donut swimmer [33].

observe that in swimming cells, the mechanism mainly comes from mass transportation among the cell body and blebs, rather than significant changes in the cell length. Hence in our model we assume that all connecting arms have fixed length and all the degrees of freedom only come from mass exchange between adjacent spheres. We start from a linear three-sphere model, we study the translation and efficiency for a prescribed cyclic swimming stroke and examine how different factors effect the swimming behavior. Later we consider a linear model consisting of more spheres.

- In Chapter 3 we develop a variation of the linear three-sphere swimmer as introduced in Chapter 2. In this planer linked-spheres model, the spheres no longer lie along a line, instead they lie in a plane. Such asymmetry naturally leads to both translation and rotation.

- We want to apply our linked-spheres models to complex fluids. We start by considering linear Maxwell viscoelastic flows. In Chapter 4 we examine a translating and expanding sphere in linear Maxwell viscoelastic fluid. We derive the transformation relations between a global reference frame and a body frame for such mechanism, and investigate how the viscoelasticity of the fluid effects the force exerted on the sphere.

- Our next step is to employ seek mathematical methods that enable us study the swimming behavior that result from more general shape deformations than those achievable with simple mechanical models. We start from planer low Reynolds number Newtonian fluids. Muskhelishvili established a method that allows us use complex analysis to deal with planar Stokes flows [61], and Shapere and Wilczek [29, 30] first applied it to low Reynolds number swimming problems. In Chapter 5 we briefly review their work and present some analytical proofs that are missing from existing literature. In Chapter 6 we discuss how to solve the swimming problems for certain kinds of shapes and analyze some simple examples.

- With the analytical framework established in Chapter 5 and Chapter 6, we computationally examine a large variety of sequences of shapes generated mathematically so as to discover some intrinsic properties in low Reynolds number swimming.

Then we validate our computational results in certain simple examples for which we could actually obtain some analytical results.

- In Chapter 8 we apply the strategy established in Chapter 5 and Chapter 6 to the swimming Dictyostelium amoebae. Our numerical simulations are based on observations from [2, 1]. We compare our computational results with the original experimental data and examine how cell shapes effect the swimming behavior of Dictyostelium.

- In Chapter 9 we point out possible future work aimed at understanding the amoeboid mode of low Reynolds number swimming.

Chapter 2

Linear Linked-spheres Swimmer

Some cells produce hemispherical membrane blisters called blebs, in which the membrane detaches from the cortex locally and the excess internal pressure forces fluid into the blebbing [20, 21]. Such blebbing dynamics may result in an oscillatory motion of cell especially when associated with shape oscillation (a cell dynamics also intrigued by cortical acto-myosin contractility [21, 19]). In such dynamics usually the cell body is rounded, and the blebs are hemispherical as we mentioned. Due to such spherical geometry of different cell parts, linked-spheres models appear to be good choices in our study of this kind of dynamics. However most existing linked-spheres models require great changes in the length of the linking arms as we introduced in Chapter 1, which is not so realistic in blebbing cells: in blebbing cells, the shape changes mainly come from mass exchange within the cell body and the blebs other than significant stretching and contracting of the whole cell. Thus we need to bring up a new model that better describes such multiple blebbing dynamics.

Inspired by Golestanian's three linked spheres model [53], we also consider three spheres linked by two slender massless arms imagining that the central sphere is the cell body and the two aside are blebs. Yet unlike in Golestanian's model where the spheres are assumed to be rigid and the length of both connecting arms are allowed to change, in our model we require that the connecting arms have fixed length and the spheres could expand or contract only in the radial direction so that each sphere could exchange mass with its neighbors. The analysis, simulation and conclusion of this linked three-spheres model are presented in Section 2.1 - 2.3. Later we consider a linear $(n+1)$-spheres

model in Section 2.4 - 2.5, which can be imagined as a "breathing" elongated cell with mass transportation up and down the length of the cell body.

So far there is no evidence showing that swimming cells have large quantities of material exchanging with surrounding fluid, hence we assume them to be incompressible. Thus in our linked-spheres model we require mass conservation on the whole object. We are interested in the fluid-structure interaction and at this point we do not care too much about the dynamics inside the cell, hence for simplicity we may assume the density in all three spheres in our model to be a same constant, in which case the mass conservation is equivalent to volume conservation. With such constraint, it is easily seen from the "scallop theorem" [28] that a cyclic two-sphere model cannot swim since it has only one degree of freedom. Therefore a minimal model must comprise at least three spheres.

2.1 Linear three-spheres model

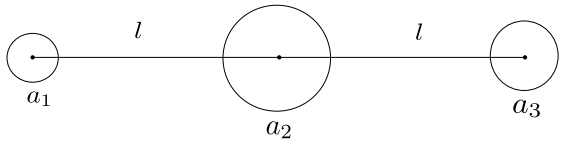

Figure 2.1: Linear three sphere swimmer

We consider a linked three-spheres model shown in Figure 2.1, immersed in viscous Newtonian fluid with no-slip boundary conditions. The connecting rods are massless, the distance l between the centers of two adjacent spheres is constant, and for simplicity we assume that during the mass exchange process between adjacent spheres, the volumes remain spherical. Let a_i be the radius of the ith sphere and assume that $\varepsilon \sim a_i/l \ll 1$, so that we may obtain asymptotic solutions.

2.1.1 Analysis of the model

The asymptotic solution to Stokes equations (1.2) for a flow around a single sphere of radius a dragged by a force $\mathbf{f}$ and, in addition, dilated at rate $\dot{v}$ is:

$$\mathbf{u}\big(\mathbf{r}; a, \mathbf{f}, \dot{v}\big) = \frac{1}{24\pi\mu r}\Big[\big(3+\xi^2\big)\mathbf{f} + 3\big(1-\xi^2\big)\big(\mathbf{f}\cdot\widehat{\mathbf{r}}\big)\widehat{\mathbf{r}}\Big] + \frac{\dot{v}}{4\pi r^2}\widehat{\mathbf{r}} \tag{2.1}$$

where $\mathbf{u}(\mathbf{x}; a, \mathbf{f}, \dot{v})$ is the velocity field at a position $\mathbf{x}$ from the center of the sphere and $\xi \equiv a/r$ [58]. The first term on the right hand side of equation (2.1) is the Stokes solution and the second term is a source term.

In the linear case, by symmetry, both the net velocities of the spheres and the net forces acting on each sphere should be parallel to the symmetry axis, thus can be taken as scalars. Let f_i be the net force acting on the ith sphere by the surrounding Stokes fluid. The (approximate) solution determines the velocities U_i of the centers of the three spheres are:

$$\begin{cases} U_1 = u[a_1; a_1, f_1, 0] + u[-l; a_2, f_2, \dot{v}_2] + u[-2l; a_3, f_3, \dot{v}_3] \\ U_2 = u[a_2; a_2, f_2, 0] + u[l; a_1, f_1, \dot{v}_1] + u[-l; a_3, f_3, \dot{v}_3] \\ U_3 = u[a_3; a_3, f_3, 0] + u[2l; a_1, f_1, \dot{v}_1] + u[l; a_2, f_2, \dot{v}_2] \end{cases} \tag{2.2}$$

As illustrated in [58], the $u[a_i; a_i, f_i, 0]$ terms describe how each sphere moves relative to the fluid according to Stokes' law as a result of the force f_i acting on it. The other two terms in each line (which is typically smaller) describes the velocity of the fluid surrounding the sphere (at distances $\gg a$ but $\ll l$) as a result of the movement of the other spheres. To leading order in $\varepsilon \sim a_i/l$, equations (2.2) reduce to

$$\begin{cases} U_1 = \dfrac{f_1}{6\pi\mu a_1} + \dfrac{f_2}{4\pi\mu l} + \dfrac{f_3}{8\pi\mu l} - \dfrac{\dot{v}_2}{4l^2} - \dfrac{\dot{v}_3}{16l^2} \\ U_2 = \dfrac{f_1}{4\pi\mu l} + \dfrac{f_2}{6\pi\mu a_2} + \dfrac{f_3}{4\pi\mu l} + \dfrac{\dot{v}_1}{4l^2} - \dfrac{\dot{v}_3}{4l^2} \\ U_3 = \dfrac{f_1}{8\pi\mu l} + \dfrac{f_2}{4\pi\mu l} + \dfrac{f_3}{6\pi\mu a_3} + \dfrac{\dot{v}_1}{16l^2} + \dfrac{\dot{v}_2}{4l^2} \end{cases} \tag{2.3}$$

It is reasonable to assume that $O(f_1) \sim O(f_2) \sim O(f_3)$, hence equations (2.3) can be further simplified to

$$\begin{cases} U_1 \sim \dfrac{f_1}{6\pi\mu a_1} - \dfrac{\dot{v}_2}{4l^2} - \dfrac{\dot{v}_3}{16l^2} \\ U_2 \sim \dfrac{f_2}{6\pi\mu a_2} + \dfrac{\dot{v}_1}{4l^2} - \dfrac{\dot{v}_3}{4l^2} \\ U_3 \sim \dfrac{f_3}{6\pi\mu a_3} + \dfrac{\dot{v}_1}{16l^2} + \dfrac{\dot{v}_2}{4l^2} \end{cases} \tag{2.4}$$

The swimming velocity of the whole object is the mean translational velocity, i.e., $\overline{U} = \dfrac{1}{3}(U_1 + U_2 + U_3)$. Since the length of the two connecting arms is the constant l, we have $\dot{l} = U_2 - U_1 = U_3 - U_2 = 0$, and therefore

$$U_1 = U_2 = U_3 = \overline{U} \tag{2.5}$$

The system is force-free, hence

$$f_1 + f_2 + f_3 = 0 \tag{2.6}$$

We require that the total mass of all spheres is conserved and assume that all spheres have a same constant density, hence the mass conservation constraint can be transformed to volume conservation constraint:

$$\dot{v}_1 + \dot{v}_2 + \dot{v}_3 = 0 \qquad \text{or} \qquad a_1^2\dot{a}_1 + a_2^2\dot{a}_2 + a_3^2\dot{a}_3 = 0 \tag{2.7}$$

From equations $(2.4, 2.5, 2.6, 2.7)$ we obtain

$$\bar{U} = \frac{(a_1 + a_2 - \frac{3}{4}a_3)\dot{v}_1 - (a_3 + a_2 - \frac{3}{4}a_1)\dot{v}_3}{4l^2(a_1 + a_2 + a_3)} \tag{2.8}$$

where $a_2 = \Big(\frac{3}{4\pi}V_{\text{total}} - a_1^3 - a_3^3\Big)^{1/3}$

Next, let us consider the power P required to propel the swimmer. The stress on the surface of the expanding sphere is $\sigma = \mu\dot{v}/(\pi a^3)$ [58], thus the power requisite to expand one sphere is

$$4\pi a^2\sigma\dot{a} = \sigma\dot{v} = \frac{4\mu}{3v}\dot{v}^2 \tag{2.9}$$

From equation (2.9), in order to drive the controls v_1 and v_3, our swimmer needs to invest the power

$$P = \frac{4\mu}{3}\Big[\frac{\dot{v}_1^2}{v_1} + \frac{\dot{v}_2^2}{v_2} + \frac{\dot{v}_3^2}{v_3}\Big]$$

With $v_i = 4\pi a_i^3/3$ and $\dot{v}_2 = -\dot{v}_1 - \dot{v}_3$, we obtain

$$P = \frac{\mu}{\pi}\Big[\Big(\frac{1}{a_1^3} + \frac{1}{a_2^3}\Big)\dot{v}_1^2 + \frac{2}{a_2^3}\dot{v}_1\dot{v}_3 + \Big(\frac{1}{a_2^3} + \frac{1}{a_3^3}\Big)\dot{v}_3^2\Big] \tag{2.10}$$

Finally we define the efficiency of a stroke γ as:

$$\frac{1}{3}e(\gamma) := \frac{6\pi\mu X^2(\gamma)}{\tau\int_0^\tau P dt} \tag{2.11}$$

This definition was originally adopted by Lighthill [48] and later widely used in low Reynolds number swimming problems for nearly spherical swimmers and linked-spheres models [30, 31, 62, 54]. In equation (2.11), the term $6\pi\mu X^2\tau^{-1}$ measures the energy

required for an external force to move a sphere by the distance $X(\gamma)$ in a stroke period τ and the integral term $\int_0^\tau P dt$ measures the work done by the swimmer in performing the corresponding cyclic shape change. Hence if each sphere has radius a, a pure dragging of the linked three-spheres model by an external force has efficiency $e = 1/a$. e has the dimension of length^{-1}.

2.1.2 Simulation results of the model

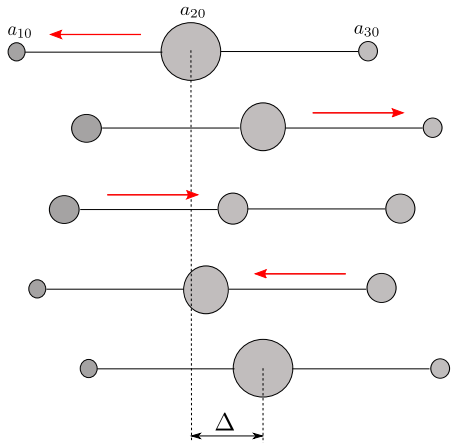

Figure 2.2: A cycle of the linear 3-sphere swimmer: (1) $\delta v_1 = -\delta v_2 = \delta_1 > 0$ while $\delta v_3 \equiv 0$; (2) $\delta v_3 = -\delta v_2 = \delta_2 > 0$ while $\delta v_1 \equiv 0$; (3) $\delta v_1 = -\delta v_2 = -\delta_1 < 0$ while $\delta v_3 \equiv 0$; (4) $\delta v_3 = -\delta v_2 = -\delta_2 < 0$ while $\delta v_1 \equiv 0$. Δ is the net translation of the swimmer after a full cycle. The red arrows indicate the mass exchange direction.

We consider a prescribed cycle of shape changes as depicted in Figure 2.2. Suppose that at the beginning of each cycle, the radius of the ith sphere is a_{i0}. We make some further simplifying assumption that each step lasts for a same time T, hence it takes $4T$ to complete one full cycle. In each step, either the first or the third sphere will expand or contract with $\dot{a}_1 = \pm u$ or $\dot{a}_3 = \pm u$, where u is a constant velocity. We may assume that $u > 0$, which indicates an expansion.

The total net translation Δ after one full cycle is given by

$$\Delta = \int_0^T (\overline{U}_1 + \overline{U}_2 + \overline{U}_3 + \overline{U}_4) \mathrm{d}t$$

where $\overline{U}_i$ is the mean translational velocity for the ith step, as given in equation (2.8). In this linear case, the signed distance $X(\gamma)$ resulting from a stroke γ is given as $X(\gamma) =$

$\Delta(\gamma)$, while later in Chapter 3 when we consider the planar model, we take the unsigned distance $X(\gamma)$ as $X(\gamma) = |\mathbf{\Delta}(\gamma)|$, since in the planar case $\mathbf{\Delta}$ is a vector while in the current linear case Δ is a scalar.

First let us consider a simple example: $a_{10} = a_{30} = a$, $a_{20} = sa$, and $uT = a$. The two side spheres start with equal sizes and s measures the size of the central sphere. To ensure that none of the spheres vanishes, we require that $s^3 \geq 14$. The relation between $l^2\Delta/(\pi a^3)$ and s is depicted in Figure 2.3 with $s \in [2.41, 5]$ and with $s \in [2.41, 1000]$.

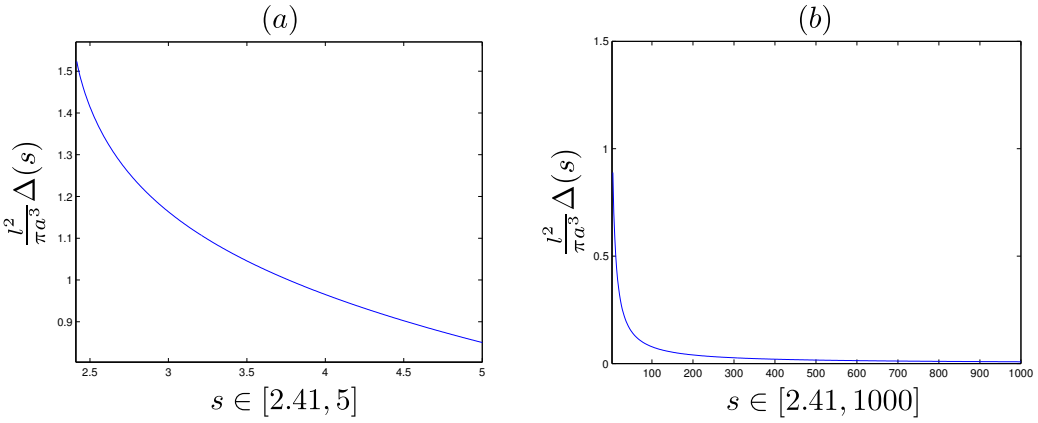

Figure 2.3: The relation between the net translation $l^2\Delta/(\pi a^3)$ and the initial size s of the center sphere: (a) $l^2\Delta/(\pi a^3)$ with $s \in [2.41, 5]$; (b) $l^2\Delta/(\pi a^3)$ with $s \in [2.41, 1000]$.

In the case that s is not so large, say, $s \sim O(1)$, we have $l^2\Delta/(\pi a^3) \sim O(1)$, i.e. $\Delta \sim a\varepsilon^2$, where $\varepsilon = a/l \ll 1$. However, as s increases, the net translation Δ decreases quickly, as is shown in Figure 2.3 (a), from which we may also see that $l^2\Delta/(\pi a^3) \to 0$ as $s \to \infty$.

Next let us consider a more general case. Suppose that in each step lasting for time T, either the first sphere expands or contracts with $\dot{a}_1 = \pm u_1$, or the third sphere expands or contracts with $\dot{a}_3 = \pm u_3$, where $u_1 > 0$ and $u_3 > 0$ are constants. Let $a_{10} = a$, $a_{20} = s_2 a$, $a_{30} = s_3 a$, and $u_1 T = r_1 a$, $u_3 T = r_3 a$, with the condition:

$$s_2^3 \geq (1 + r_1)^3 - 1 + (s_3 + r_3)^3 - s_3^3$$

s_2, s_3 measure the initial sizes of the 2nd and 3rd spheres, respectively. r_1, r_3 measure the amplitude of radius changes of 1st and 3rd spheres.

Let us consider two cases:

1. In the case that $r_1 = r_3 := r$, namely the two side spheres have the same rate of radius change, the relation between $l^2\Delta/(\pi a^3)$ and r with $s_3 = 1, 2, 3, 4$ are depicted in Figure 2.4 (a). Here $s_2 = 7$ in each trial. From Figure 2.4 (a) we see that increasing either the ratio $s_3 = a_{30}/a_{10}$ or the the change of spheres' radii r will increase the net translation efficiently.

2. Next consider the case when $s_3 = 1$, namely the two side spheres start with equal sizes. The relation between $l^2\Delta/(\pi a^3)$ and (r_1, r_3) is depicted in Figure 2.4 (b). Here we take $s_2 = 8$. From Figure 2.4 (b) we see that the net translation increases as either r_1 or r_3 increases. Moreover, we notice from Figure 2.4 (b) that when $r_1 = 0$ or $r_3 = 0$, the net translation $\Delta = 0$, which coincides with the "scallop theorem" [28].

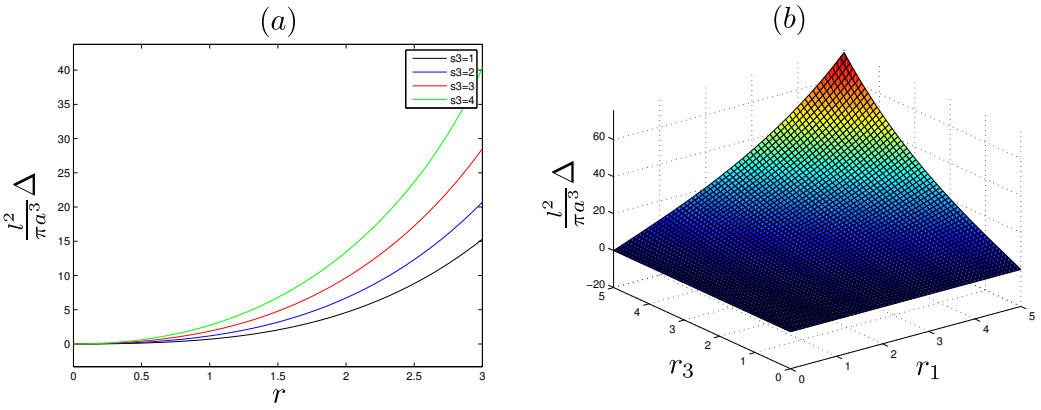

Figure 2.4: The relation between the net translation $l^2\Delta/(\pi a^3)$ and the stroke amplitude: (a) $l^2\Delta/(\pi a^3)$ as a function of r with $s_2 = 7$ and $s_3 = 1, 2, 3, 4$; (b) $l^2\Delta/(\pi a^3)$ as a function of (r_1, r_3) with $s_2 = 8$.

As for efficiency of the swimmer, first we consider a stroke with each step lasting for time T, with the initial status $a_{10} = a_{30} = a$, $a_{20} = sa$ ($s > 2.4101$) and $u_1 T = u_3 T = a$. With efficiency given by equation (2.11), the relation between $l^4 e/(3\pi^2 a^3)$ and s is shown in Figure 2.5 for $s \in [2.41, 5]$ and $s \in [2.41, 100]$. We see that there is a maximum of efficiency around $s = 2.6$, and after that the efficiency decreases quickly as s increases.

Next we take $a_{10} = a_{30} = a$, $a_{20} = s_2 a$, $u_1 T = u_3 T = ra$, the relation between

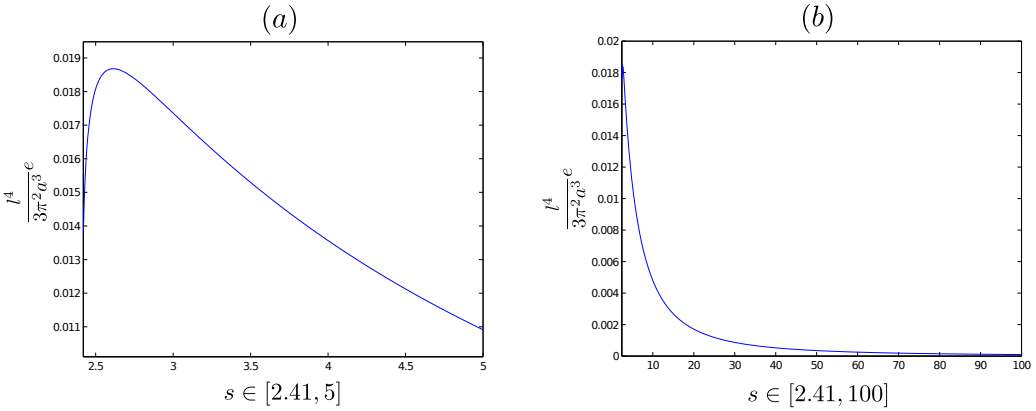

Figure 2.5: The relation between the efficiency $l^4e/(3\pi^2a^3)$ and the initial size s of the center sphere: (a) $l^4e/(3\pi^2a^3)$ with $s \in [2.41, 5]$; (b) $l^4e/(3\pi^2a^3)$ with $s \in [2.41, 1000]$.

$l^4e/(3\pi^2a^3)$ and r is given in Figure 2.6 for $s_2 = 7$ and $s_2 = 15$. Figure 2.6 shows that the efficiency increases as the stroke amplitude increases. Moreover, if we compare Figure 2.6 (a) and (b), we see that the efficiency for models with smaller center spheres (Figure 2.6 (a)) increases faster than those with bigger center spheres (Figure 2.6 (b)).

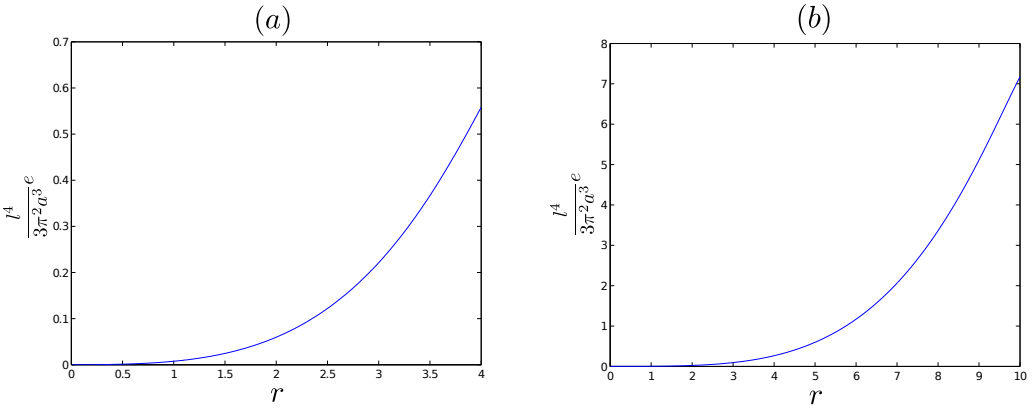

Figure 2.6: The relation between the efficiency $l^4e/(3\pi^2a^3)$ and the stroke amplitude: (a) $l^4e/(3\pi^2a^3)$ with $s_2 = 7$; (b) $l^4e/(3\pi^2a^3)$ with $s_2 = 15$.

2.1.3 Conclusions

From the experiment results above, we observe that increasing the change of radii (i.e., u_1T and u_3T) in each step of the cycle will increase both the net translation of the

swimmer after a full cycle and its efficiency, while increasing the initial size of the central sphere will decrease them. In the following, I will show parts of these relations analytically.

Notice that a swimming stroke is a closed path in the $v_1 - v_3$ plane (since we have the volume constraint equation (2.7)), or equivalently, a closed path in the $a_1 - a_3$ plane. From equation (2.8), we have the relation between the differential displacement $\bar{\mathsf{d}}x$ and the (differential) controls $(\mathsf{d}a_1, \mathsf{d}a_3)$:

$$\bar{\mathsf{d}}X = \frac{\pi}{l^2}\Big[a_1^2\big(1 - \frac{7}{4}\frac{a_3}{a_1+a_2+a_3}\big)\mathsf{d}a_1 - a_3^2\big(1 - \frac{7}{4}\frac{a_1}{a_1+a_2+a_3}\big)\mathsf{d}a_3\Big] \tag{2.12}$$

Here $\bar{\mathsf{d}}X > 0$ represents an infinitesimal displacement to the right in Figure 2.2. The bar in $\bar{\mathsf{d}}X$ stresses that the differential displacement does not integrate to a function $X(a_1, a_3)$. Keep in mind that total the displacement $X(\gamma) \equiv \int_\gamma \bar{\mathsf{d}}X$ after one cycle depends on the path γ in the the space of controls, represented by a curve in the $a_1 - a_3$ plane.

First for the swimming direction, from equation (2.12), without loss of generality, we may assume that $da_3 = 0$ and $da_1 > 0$, which means that sphere 3 does not change, and sphere 1 is expanding while sphere 2 is contracting. For a_2 large enough so that $1 - \frac{7}{4}\frac{a_3}{a_1+a_2+a_3} > 0$ always holds, we have $\bar{\mathsf{d}}X > 0$, which means that the swimming direction is pointing from sphere 1 to sphere 2. Hence we have the following conclusion which coincides with the conclusion in [58]:

Conclusion 1. *When only one pair of adjacent spheres is involved in volume exchange, under the condition that the middle sphere is large enough, the swimming direction of the swimmer is always directed from the expanding sphere to the contracting one.*

Next, using Stokes' theorem of elementary calculus, the translation δX to an infinitesimal closed loop is

$$\delta X = \frac{7\pi}{4l^2}\Big[a_1^2\partial_{a_3}\frac{a_3}{a_1+a_2+a_3} + a_3^2\partial_{a_1}\frac{a_1}{a_1+a_2+a_3}\Big]da_1 \wedge da_3 \tag{2.13}$$

where $da_1 \wedge da_3$ denotes the signed area enclosed by the loop. We claim that:

Conclusion 2. *For strokes such that γ is homotopic to the unit circle S^1, increasing the stroke amplitude will increase the net translation of the stroke, while increasing the*

initial radius a_{20} of the central sphere (with a_{10} and a_{30} unchanged) will decrease the net translation. Moreover, we have the approximation

$$|X(\gamma)| \sim \frac{\varepsilon}{l} Area(\Omega)$$

where $\varepsilon \sim a_i/l$ and Ω is the region enclosed by γ and $Area(\Omega)$ is its signed area.

Proof. For infinitesimal strokes the first part of is obvious from equation (2.13). For strokes such that $|\int_\gamma d\gamma| \sim a$, we consider two strokes γ and $\widetilde{\gamma}$, such that $\Omega \subset \widetilde{\Omega}$. We assume that γ and $\widetilde{\gamma}$ have the same direction, so that the signed areas $\mathrm{Area}(\Omega)$ and $\mathrm{Area}(\tilde{\Omega})$ have the same sign. Without loss of generality, we may assume that $\mathrm{Area}(\Omega) > 0$ and $\mathrm{Area}(\widetilde{\Omega}) > 0$, which indicates that $\mathrm{Area}(\widetilde{\Omega} \setminus \Omega) > 0$. We have

$$X(\widetilde{\gamma}) - X(\gamma) = \frac{7\pi}{4l^2}\psi(\zeta_1, \zeta_3)\mathrm{Area}(\widetilde{\Omega} \setminus \Omega)$$

for some $(\zeta_1, \zeta_3) \in \widetilde{\Omega} \setminus \Omega$, where

$$\psi(a_1, a_3) = \frac{a_1^2 a_3^2}{(a_1 + a_2 + a_3)^2}\Big[\frac{a_2 + a_3}{a_1^2} + \frac{a_1 + a_3}{a_2^2} + \frac{a_1 + a_2}{a_3^2}\Big]$$

Since ψ is always positive, so $X(\widetilde{\gamma}) > X(\gamma)$.

For the second part, first we calculate that:

$$a_1^2\partial_{a_3}\frac{a_3}{a_1 + a_2 + a_3} + a_3^2\partial_{a_1}\frac{a_1}{a_1 + a_2 + a_3} = \frac{a_1^2 a_3^2}{(a_1 + a_2 + a_3)^2}\Big[\frac{a_2 + a_3}{a_1^2} + \frac{a_1 + a_3}{a_2^2} + \frac{a_1 + a_2}{a_3^2}\Big] \quad (2.14)$$

It is obvious from equation (2.14) that increasing the a_{20} with a_{10} and a_{30} unchanged will increase $a_1^2\partial_{a_3}\dfrac{a_3}{a_1 + a_2 + a_3} + a_3^2\partial_{a_1}\dfrac{a_1}{a_1 + a_2 + a_3}$, which in return will increase δX.

Finally, from equation (2.14), we have

$$\Big|a_1^2\partial_{a_3}\frac{a_3}{a_1 + a_2 + a_3} + a_3^2\partial_{a_1}\frac{a_1}{a_1 + a_2 + a_3}\Big| \sim a_i$$

Here we assume that a_i's have the same order. Then from equation (2.13), we have

$$|\delta X| \sim \frac{a_i}{l^2}|da_1 \wedge da_3| \sim \frac{\varepsilon}{l}|da_1 \wedge da_3|$$

□

Finally, for the efficiency of the swimmer, we claim that

Conclusion 3. *Increasing the initial radius a_{20} of the central sphere (with a_{10} and a_{30} unchanged) will decrease the efficiency. Also, for infinitesimal strokes, increasing the stroke amplitude $|da_1 \wedge da_3|$ symmetrically by some rate r (i.e., $\widetilde{da_1} = rda_1$ and $\widetilde{da_3} = rda_3$) will increase the efficiency by r^2. Especially, if we assume that $a_i \sim a$ and $da_i \sim da$, then we have the approximation:*

$$\bar{de} \sim \frac{a|da|^2}{l^4}$$

Proof. From equation (2.10), we have

$$\bar{dP} = 16\pi\mu\Big[a_1^4\big(\frac{1}{a_1^3} + \frac{1}{a_2^3}\big)(da_1)^2 + \frac{2a_1^2a_3^2}{a_2^3}da_1da_3 + a_3^4\big(\frac{1}{a_2^3} + \frac{1}{a_3^3}\big)da_3^2\Big] \tag{2.15}$$

When we increase the stroke so that $\widetilde{da_1} = rda_1$ and $\widetilde{da_3} = rda_3$, for infinitesimal stroke, from equation (2.13) and equation (2.15), we have $|\widetilde{\delta X}| = r^2|\delta X|$ and $\widetilde{\bar{dP}} = r^2\bar{dP}$. From the definition of efficiency equation (2.11), we have $\tilde{e} = r^2e$. Here notice that since the integral in equation (2.11) is with respect to time instead of specified stroke path, so the integral will not result in extra terms of r.

To prove the relation between the efficiency and a_{20}, notice that from equations (2.13,2.14,2.15), the efficiency of an infinitesimal stroke (da_1, da_3) within an infinitesimal stroke time dt can be written as:

$$\bar{de} = \frac{C}{l^4}\frac{a_1^4a_3^4\big[\frac{a_3}{a_1^2} + \frac{a_1}{a_3^2} + \big(\frac{1}{a_1^2} + \frac{1}{a_3^2}\big)a_2 + \frac{a_1+a_3}{a_2^2}\big]^2\big|da_1 \wedge da_3\big|^2}{\big(a_1+a_2+a_3\big)^4\big[a_1(da_1)^2 + a_3(da_3)^2 + \frac{1}{a_2^3}\big(a_1^2da_1 + a_3da_1\big)^2\big]} \tag{2.16}$$

where C is some unitless constant. Notice that equation (2.16) is of the form

$$\bar{de} = \frac{C}{l^4}\frac{\Phi_1\big(\Phi_2a_2^3 + \Phi_3a_2^2 + \Phi_4\big)^2}{a_2\big(a_2+\Phi_5\big)^4\big(\Phi_6a_2^3 + \Phi_7\big)}$$

with Φ_i $(i = 1, 2, \cdots, 7)$ functions of a_1, a_3, da_1 and da_3 only and independent of a_2. Obviously, $\bar{de}$ decreases when increasing a_2 while holding other parameters unchanged.

Finally, from equation (2.16), it is obvious that $\bar{de} \sim a|da|^2/l^4$. □

The relation between the stroke amplitude and the efficiency is difficult to generalize, since it relies too much on the choice of the stroke path γ. However, from equation (2.15), we may see that if the stroke is "good" enough, then increasing the stroke amplitude (i.e., increasing in both a and $|da|$ in this case) leads to an increase in the efficiency.

Finally we make a comparison between our linked three-spheres model and Golestanian's linked three-spheres model. From Figure 2.5 and Figure 2.6, the efficiency e scales like a^3/l^4, while it is reported for Golestanian's linked three-spheres model[1] that the efficiency e scales like ad^2/l^4 where d is the amplitude of length variation of the linking arms [54]. To make a reasonable comparison we may assume that d has the same scale as a, hence approximately these two kinds of linked three-spheres models have the same efficiency.

2.2 Linear multiple spheres model

In this section we consider a $(n+1)$-sphere swimmer as shown in Figure 2.7. This micro-structure consists of $n+1$ spheres and n massless connecting rods. Each rod connects two adjacent spheres, and the distance between any two adjacent spheres is fixed as l. Similar to Section 2.1, we assume that the spheres are elastic bodies and apply no-slip boundary conditions on them. Each pair of adjacent spheres can exchange mass. The total volume of all spheres, V_{total}, is conserved. Let a_i be the radius of the ith sphere, $v_i = 4\pi a_i^3/3$ is the volume of the ith sphere. Each sphere exerts a force f_i on (and experiences a force $-f_i$ from) the fluid that is parallel the symmetry axis.

Figure 2.7: Linear $(n+1)$-sphere swimmer

2.2.1 Analysis of the model

We still assume that $\varepsilon \sim a_i/l \ll 1$ as in the linear three-spheres model. The solution determines the velocity U_i of the center of the ith sphere is:

$$U_i = u[a_i; a_i, f_i, 0] + \sum_{j=1}^{i-1} u[(i-j)l; a_j, f_j, \dot{v}_j] + \sum_{k=i+1}^{n+1} u[-(k-i)l; a_k, f_k, \dot{v}_k] \qquad (2.17)$$

[1] In [54] the efficiency is defined as $e_L = ae$, where e is given by equation (2.11). And it is reported in [54] that e_L scales like a^2d^2/l^4.

where u is given by equation (2.1). Keep in mind that in the linear case, the velocity of each sphere and the forces on them are parallel to the symmetry axis.

Assume that f_i's have the same order, then to leading order of ε, equation (2.17) reduces to

$$U_i \sim \frac{f_i}{6\pi\mu a_i} + \frac{1}{4l^2}\Big[\sum_{j=1}^{i-1}\frac{\dot{v}_j}{(i-j)^2} - \sum_{k=i+1}^{n+1}\frac{\dot{v}_k}{(k-i)^2}\Big] \tag{2.18}$$

The swimming velocity of the whole object (i.e., the mean translational velocity) is

$$\bar{U} = \frac{\sum_{i=1}^{n+1} U_i}{n+1} \tag{2.19}$$

From equation (2.18) and equation (2.19), we obtain

$$\begin{aligned}(n+1)\bar{U} &= \frac{1}{6\pi\mu}\sum_{i=1}^{n+1}\frac{f_i}{a_i} + \frac{1}{4l^2}\sum_{i=1}^{n+1}\Big[\sum_{j=1}^{i-1}\frac{\dot{v}_j}{(i-j)^2} - \sum_{k=i+1}^{n+1}\frac{\dot{v}_k}{(k-i)^2}\Big] \\ &= \frac{1}{6\pi\mu}\sum_{i=1}^{n+1}\frac{f_i}{a_i} + \frac{1}{4l^2}\sum_{i=1}^{n+1}\Big(\sum_{j=1}^{n+1-i}\frac{1}{j^2} - \sum_{k=1}^{i-1}\frac{1}{k^2}\Big)\dot{v}_i \end{aligned} \tag{2.20}$$

The swimmer is assumed to be autonomous, so the whole system should be force-free:

$$\sum_{i=1}^{n+1} f_i = 0 \tag{2.21}$$

And the total volume V_{total} is conserved:

$$\sum_{i=1}^{n+1}\dot{v}_i = 0 \qquad \text{or} \qquad \sum_{i=1}^{n+1} a_i^2\dot{a}_i = 0 \tag{2.22}$$

The other constraints come from the assumption that the length between any two nearby spheres is fixed as l, thus we have

$$U_1 = U_2 = \cdots = U_{n+1} = \overline{U} \tag{2.23}$$

From equations (2.20), (2.21), (2.22) and (2.23), we obtain the mean translational velocity $\overline{U}$ as a function of $\dot{v}_1,\ \dot{v}_2,\ \cdots,\ \dot{v}_n$ as:

$$\begin{aligned}\bar{U} &= \frac{1}{4l^2\sum_{i=1}^{n+1}a_i}\sum_{i=1}^{n+1}\Big[\sum_{k=i+1}^{n+1}\frac{a_k}{(k-i)^2} - \sum_{j=1}^{i-1}\frac{a_j}{(i-j)^2}\Big]\dot{v}_i \\ &= \frac{1}{4l^2\sum_{i=1}^{n+1}a_i}\sum_{i=1}^{n}\Big(\sum_{k=i+1}^{n+1}\frac{a_k}{(k-i)^2} - \sum_{j=1}^{i-1}\frac{a_j}{(i-j)^2} + \sum_{m=1}^{n}\frac{a_m}{(n+1-m)^2}\Big)\dot{v}_i \end{aligned} \tag{2.24}$$

where $a_{n+1} = \Big(\frac{3}{4\pi}V_{\text{total}} - \sum_{i=1}^{n} a_i^3\Big)^{1/3}$.

The power P needed to propel the swimmer is

$$P = \frac{4\mu}{3}\sum_{i=1}^{n+1}\frac{\dot{v}_i^2}{v_i} = \frac{\mu}{\pi}\Big[\sum_{i=1}^{n}\Big(\frac{1}{a_i^3} + \frac{1}{a_{n+1}^3}\Big)\dot{v}_i^2 + \frac{2}{a_{n+1}^3}\sum_{i,j=1,\ i\neq j}^{n}\dot{v}_i\dot{v}_j\Big] \tag{2.25}$$

And in correspondence of equation (2.11), we define the efficiency of a linear $(n+1)$-sphere swimmer of a stroke γ as

$$e(\gamma; n) = \frac{6\pi\mu(n+1)X^2(\gamma)}{\tau\int_0^\tau P\ dt} \tag{2.26}$$

2.2.2 Simulation results and conclusions

Now let us consider a simple cycle of motion of this model. Suppose that at the beginning of the cycle, the ith sphere has radius $a_i = a$, and volume $v_i = v = 4\pi a^3/3$. The cycle consists of $2n$ steps. To simplify the computation, instead of considering the rate of change of the radius, we consider the rate of change of the volume. Assume that in the i-th step the i-th and $(i+1)$-th spheres exchange mass:

$$\dot{v}_i = -u, \qquad \dot{v}_{i+1} = u, \qquad \text{and } \dot{v}_j = 0,\ j \neq i, i+1 \tag{2.27}$$

and that in the $(n+i)$-th step the i-th and $(i+1)$-th spheres exchange back the same amount of mass as in the ith step:

$$\dot{v}_i = u, \qquad \dot{v}_{i+1} = -u, \qquad \text{and } \dot{v}_j = 0,\ j \neq i, i+1 \tag{2.28}$$

where $u > 0$ is a constant. The motion defined by equation (2.27) and equation (2.28) completes a full cycle, as illustrated in Figure 2.8.

Here we are interested in how the number of spheres n effects the swimming behavior of the model, that is, how the length of the elongated "cell" effects the swimming. Let $uT = sv$, here s measures the amount of mass exchange in each step. The simulation results for the net translation $\Delta(n)$ and the efficiency $e(n)$ with different values of s are given in Figure 2.9 and Figure 2.10, respectively. From Figure 2.9 we see that increasing the amount of mass exchange in each step (measured by s) may increase the net translation (here notice that the direction of the swimming is to the left). Also, increasing the number of spheres will lead to an increase in the net translation. However,

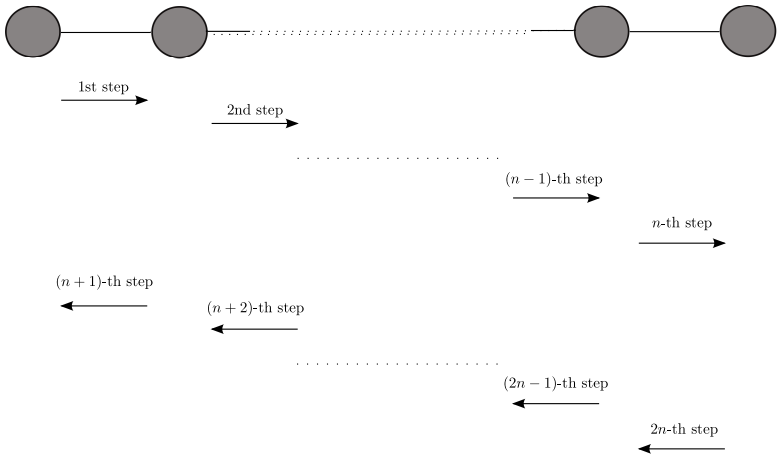

Figure 2.8: A cycle of the linear $(n+1)$-sphere swimmer prescribed by equation (2.27) and equation (2.28).

for fixed s, as the number of spheres n increases, the net translation quickly approaches a maximum that depends on s.

As for efficiency, increasing the change of volume in each step will increase the efficiency, however as the number of spheres increases, the efficiency decreases rapidly, as is shown in Figure 2.10.

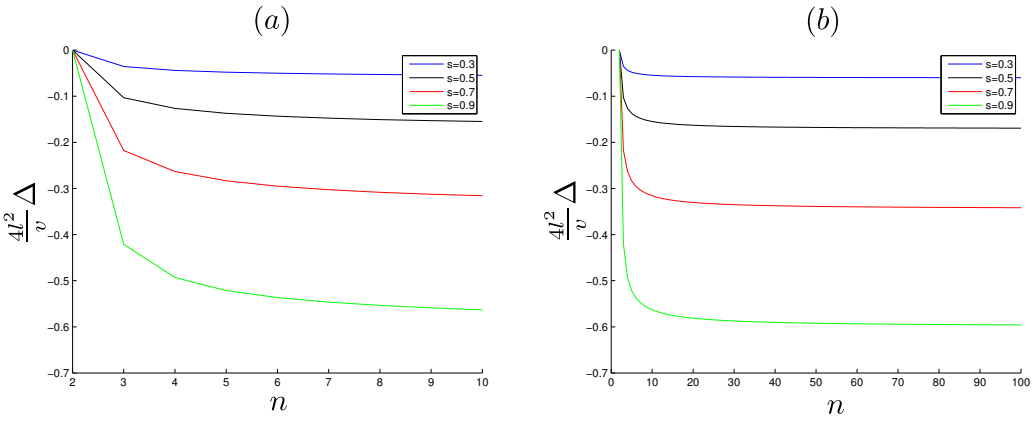

Figure 2.9: The relation between the net translation $4l^2\Delta/v$ and the number of spheres n: (a) $4l^2\Delta/v$ of n with different values of s; (b) $4l^2\Delta/v$ of n with different values of s.

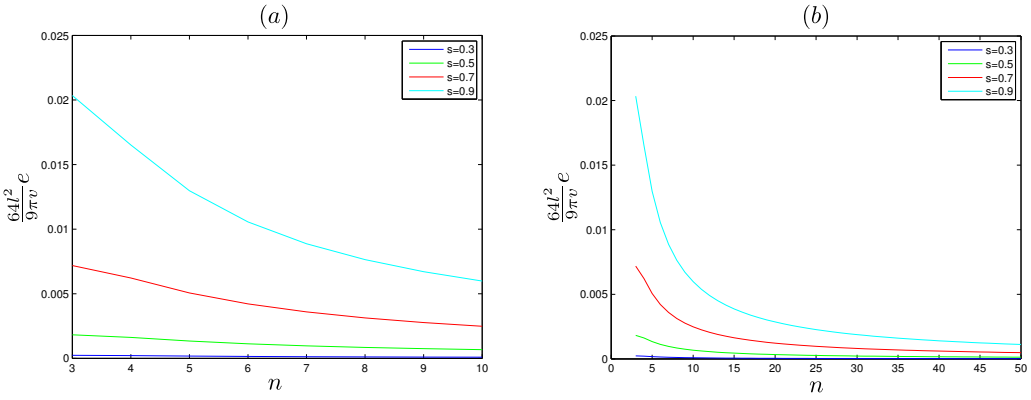

Figure 2.10: The relation between the efficiency $64l^2e/9\pi v$ and the number of spheres n: (a) $64l^2e/9\pi v$ of n with different values of s; (b) $64l^2e/9\pi v$ of n with different values of s.

Chapter 3

Planar Three-spheres Swimmer

In this chapter we consider a planar 3-sphere swimmer that can move in the plane as shown in Figure 3.1. Instead of all spheres and linking arms lie in a line as in the linear three-spheres model, in this planar model the two linking arms are separated by an angle α. The first and second spheres can exchange mass with the central zeroth sphere while preserving the total mass. We follow the notations and assumptions given in Chapter 2 unless specified otherwise.

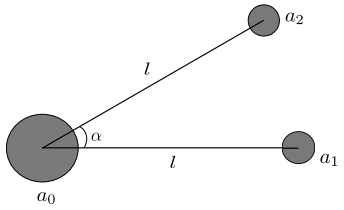

Figure 3.1: General 3-sphere swimmer

3.1 Analysis of the model

For each sphere, we define a local cylindrical coordinate system $(\mathbf{e}_{r_i}, \mathbf{e}_{\theta_i})$, such that $\mathbf{e}_{r_i}$ $(i = 1, 2)$ is the unit vector pointing from the center of the zeroth sphere to the center of the i-th sphere. And for the central zeroth sphere we set $\mathbf{e}_{r_0} = \mathbf{e}_{r_1}$, $\mathbf{e}_{\theta_0} = \mathbf{e}_{\theta_1}$, as shown in Figure 3.2.

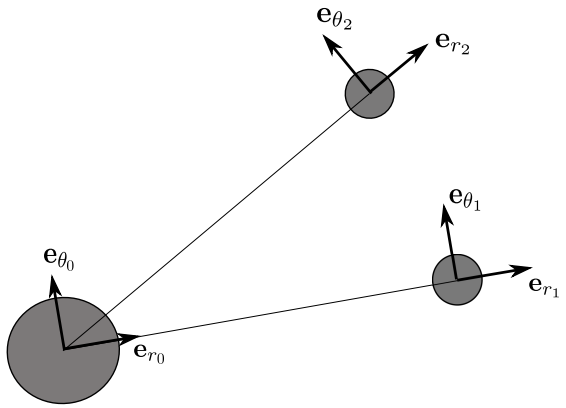

Figure 3.2: Local cylindrical coordinate systems.

The transformation relation between the two coordinates is given as:

$$\begin{cases} \mathbf{e}_{r_2} = \mathbf{e}_{r_1}\cos\alpha + \mathbf{e}_{\theta_1}\sin\alpha \\ \mathbf{e}_{\theta_2} = -\mathbf{e}_{r_1}\sin\alpha + \mathbf{e}_{\theta_1}\cos\alpha \end{cases} \tag{3.1}$$

To simplify the calculation, here we still require that the ratio of the radii of the spheres to the distances between each pair of adjacent spheres to be small enough. To fulfill this requirement, we need both $a_i/l \ll 1$ as discussed in Chapter 2 and $a_i/l\alpha \ll 1$ so to make sure that the first and second spheres do not come too close. From equation (2.1), the solution determines the velocities $\mathbf{U}_i$ of the centers of the spheres are:

$$\begin{cases} \mathbf{U}_0 = \mathbf{u}[a_0\mathbf{e}_{r_1}; a_0, \mathbf{f}_0, 0] + \mathbf{u}[-l\mathbf{e}_{r_1}; a_1, \mathbf{f}_1, \dot{v}_1] + \mathbf{u}[-l\mathbf{e}_{r_2}; a_2, \mathbf{f}_2, \dot{v}_2] \\ \mathbf{U}_1 = \mathbf{u}[a_1\mathbf{e}_{r_1}; a_1, \mathbf{f}_1, 0] + \mathbf{u}[l\mathbf{e}_{r_1}; a_0, \mathbf{f}_0, \dot{v}_0] + \mathbf{u}[-l(1-\cos\alpha)\mathbf{e}_{r_2} - l\sin\alpha\mathbf{e}_{\theta_2}; a_2, \mathbf{f}_2, \dot{v}_2] \\ \mathbf{U}_2 = \mathbf{u}[a_2\mathbf{e}_{r_2}; a_2, \mathbf{f}_2, 0] + \mathbf{u}[l\mathbf{e}_{r_2}; a_0, \mathbf{f}_0, \dot{v}_0] + \mathbf{u}[-l(1-\cos\alpha)\mathbf{e}_{r_1} + l\sin\alpha\mathbf{e}_{\theta_1}; a_1, \mathbf{f}_1, \dot{v}_1] \end{cases} \tag{3.2}$$

Assume that $O(|\mathbf{f}_1|) \sim O(|\mathbf{f}_2|) \sim O(|\mathbf{f}_3|)$, to leading order of $\varepsilon \sim a_i/l$ and $\epsilon \sim a_i/l\alpha$, equation system (3.2) becomes:

$$\begin{cases} \mathbf{U}_0 \sim \dfrac{1}{6\pi\mu a_0}\mathbf{f}_0 - \dfrac{\dot{v}_1}{4\pi l^2}\mathbf{e}_{r_1} - \dfrac{\dot{v}_2}{4\pi l^2}\mathbf{e}_{r_2} \\ \mathbf{U}_1 \sim \dfrac{1}{6\pi\mu a_1}\mathbf{f}_1 + \dfrac{\dot{v}_0}{4\pi l^2}\mathbf{e}_{r_1} + \dfrac{\dot{v}_2}{16\pi l^2\sin^2\frac{\alpha}{2}}\Big(-\sin\dfrac{\alpha}{2}\mathbf{e}_{r_2} - \cos\dfrac{\alpha}{2}\mathbf{e}_{\theta_2}\Big) \\ \mathbf{U}_2 \sim \dfrac{1}{6\pi\mu a_2}\mathbf{f}_2 + \dfrac{\dot{v}_0}{4\pi l^2}\mathbf{e}_{r_2} + \dfrac{\dot{v}_1}{16\pi l^2\sin^2\frac{\alpha}{2}}\Big(-\sin\dfrac{\alpha}{2}\mathbf{e}_{r_1} + \cos\dfrac{\alpha}{2}\mathbf{e}_{\theta_1}\Big) \end{cases} \tag{3.3}$$

We still require that the system is force free and the total volume V_{total} is conserved. Since here the model is no longer symmetric, we need to consider the torque of the

system as well. Let $\mathbf{O}_i(t)$ be the position of the center of sphere i at time t measured from a fixed point in the fixed global reference frame. The torque acting on the i-th sphere $\mathbf{T}_i$ has the form $\mathbf{T}_i = \mathbf{O}_i \wedge \mathbf{f}_i$. The system is torque-free, so we have

$$\mathbf{T}_0 + \mathbf{T}_1 + \mathbf{T}_2 \equiv 0 \tag{3.4}$$

and from the geometry of the swimmer we have

$$\mathbf{O}_1 = \mathbf{O}_0 + l\mathbf{e}_{r_1}, \qquad \mathbf{O}_2 = \mathbf{O}_0 + l\mathbf{e}_{r_2}$$

If we substitute these expressions into equation (3.4) and be aware of the force-free condition

$$\mathbf{f}_0 + \mathbf{f}_1 + \mathbf{f}_2 \equiv 0 \tag{3.5}$$

then equation (3.4) reduces to

$$\mathbf{e}_{r_1} \wedge \mathbf{f}_1 + \mathbf{e}_{r_2} \wedge \mathbf{f}_2 = 0 \tag{3.6}$$

Set a global Cartesian coordinate system $\{\mathbf{0}; \mathbf{e}_x, \mathbf{e}_y\}$. Since the distance between the zeroth and first spheres, the distance between the zeroth and second spheres and the angle between the two arms are all fixed, the motion of the structure can be determined by $(X_0(t), Y_0(t), \omega(t))$, where $\mathbf{O}_0 = X_0\mathbf{e}_x + Y_0\mathbf{e}_y$ gives of the center of the zeroth sphere in the reference frame $\{\mathbf{0}; \mathbf{e}_x, \mathbf{e}_y\}$. (X_0, Y_0) measures the translation of the swimmer, and ω is the angle between $\mathbf{e}_x$ and $\mathbf{e}_{r_1}$ that measures the rotation of the structure with respect to the zeroth sphere, as illustrated in Figure 3.3.

We assume the initial state to be $X_0(0) = Y_0(0) = \omega(0) = 0$. The velocity of the first and second sphere in this fixed global frame is given by:

$$\mathbf{U}_i \;\; = \;\; \mathbf{U}_0 + l\frac{d\omega}{dt}\mathbf{e}_{\theta_i} \tag{3.7}$$

From equation (3.3) and equation (3.7) together with the volume conservation constraint equation (2.7), $\mathbf{f}_0$, $\mathbf{f}_1$ and $\mathbf{f}_2$ can be written as:

$$\begin{cases} \dfrac{1}{6\pi\mu}\mathbf{f}_0 = a_0\Big[\mathbf{U}_0 + \dfrac{\dot{v}_1}{4\pi l^2}\mathbf{e}_{r_1} + \dfrac{\dot{v}_2}{4\pi l^2}\mathbf{e}_{r_2}\Big] \\ \dfrac{1}{6\pi\mu}\mathbf{f}_1 = a_1\Big[\mathbf{U}_0 + \dfrac{\dot{v}_1 + \dot{v}_2}{4\pi l^2}\mathbf{e}_{r_1} + l\dot{\omega}\mathbf{e}_{\theta_1} + \dfrac{\dot{v}_2}{16\pi l^2 \sin^2\frac{\alpha}{2}}\big(\sin\dfrac{\alpha}{2}\mathbf{e}_{r_2} + \cos\tfrac{\alpha}{2}\mathbf{e}_{\theta_2}\big)\Big] \\ \dfrac{1}{6\pi\mu}\mathbf{f}_2 = a_2\Big[\mathbf{U}_0 + \dfrac{\dot{v}_1 + \dot{v}_2}{4\pi l^2}\mathbf{e}_{r_2} + l\dot{\omega}\mathbf{e}_{\theta_2} + \dfrac{\dot{v}_1}{16\pi l^2 \sin^2\frac{\alpha}{2}}\big(\sin\dfrac{\alpha}{2}\mathbf{e}_{r_1} - \cos\tfrac{\alpha}{2}\mathbf{e}_{\theta_1}\big)\Big] \end{cases} \tag{3.8}$$

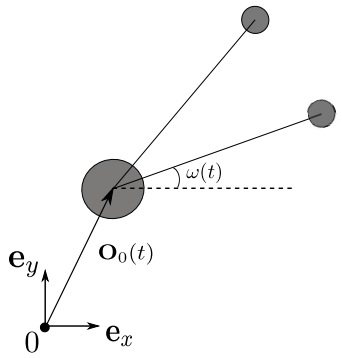

Figure 3.3: Position and polarization of the planar 3-sphere swimmer

From the above equations and the force-free condition equation (3.5), $\mathbf{U}_0$ can be written as:

$$\begin{aligned}\mathbf{U}_0 &= -\frac{1}{a_0+a_1+a_2}\Big[\frac{1}{4\pi l^2}\big[(a_0+a_1+\frac{a_2}{4\sin\frac{\alpha}{2}})\dot{v}_1+a_1\dot{v}_2\big]\mathbf{e}_{r_1}+\big[a_1l\dot{\omega}-\frac{a_2\dot{v}_1\cos\frac{\alpha}{2}}{16\pi l^2\sin^2\frac{\alpha}{2}}\big]\mathbf{e}_{\theta_1}\\ &\quad+\frac{1}{4\pi l^2}\big[a_2\dot{v}_1+(a_0+a_2+\frac{a_1}{4\sin\frac{\alpha}{2}})\dot{v}_2\big]\mathbf{e}_{r_2}+\big[a_2l\dot{\omega}+\frac{a_1\dot{v}_2\cos\frac{\alpha}{2}}{16\pi l^2\sin^2\frac{\alpha}{2}}\big]\mathbf{e}_{\theta_2}\Big] \qquad (3.9)\end{aligned}$$

Notice that

$$\mathbf{e}_{r_i}\wedge\mathbf{e}_{r_i}=\mathbf{e}_{\theta_i}\wedge\mathbf{e}_{\theta_i}=0$$
$$\mathbf{e}_{r_i}\wedge\mathbf{e}_{\theta_i}=\mathbf{e}_z \qquad \mathbf{e}_{\theta_i}\wedge\mathbf{e}_{r_i}=-\mathbf{e}_z$$

we use equation (3.6), equation (3.8) and equation (3.9) and the transformation relation equation system (3.1) and obtain:

$$\dot{\omega}=\frac{a_0\big(a_2\dot{v}_1-a_1\dot{v}_2\big)\sin\alpha}{4\pi l^3\big[a_0\big(a_1+a_2\big)+2a_1a_2\big(1-\cos\alpha\big)\big]}\Big(\frac{1}{8\sin^3\frac{\alpha}{2}}-1\Big) \qquad (3.10)$$

The assumption that $a_i/l\alpha \ll 1$ ensures that $\dfrac{1}{8\sin^3\frac{\alpha}{2}}-1$ will not be too large. Moreover we have the transformation relation

$$\begin{aligned}\mathbf{e}_{r_1}(t) &= \cos\omega(t)\mathbf{e}_x+\sin\omega(t)\mathbf{e}_y\\ \mathbf{e}_{\theta_1}(t) &= -\sin\omega(t)\mathbf{e}_x+\cos\omega(t)\mathbf{e}_y\end{aligned}$$

Then from equation (3.9), $\mathbf{U}_0$ can be written as:

$$\begin{aligned}
\mathbf{U}_0 &= -\Big[\frac{\dot{v}_1}{4\pi l^2}\big[a_0+a_1+a_2\big(\cos\alpha+\frac{1}{4\sin\frac{\alpha}{2}}\big)\big]+\frac{\dot{v}_2}{4\pi l^2}\big[a_0\cos\alpha+a_1\big(1-\frac{1}{4\sin\frac{\alpha}{2}}\big)+a_2\cos\alpha\big] \\
&\quad -a_2 l\dot{\omega}\sin\alpha\Big]\frac{\mathbf{e}_{r_1}}{a_0+a_1+a_2}-\Big[\frac{a_2\dot{v}_1}{4\pi l^2}\sin\alpha\big(1-\frac{1}{8\sin^3\frac{\alpha}{2}}\big)+\frac{\dot{v}_2}{4\pi l^2}\big(a_0\sin\alpha+a_2\sin\alpha \\
&\quad +\frac{a_1}{4\sin\frac{\alpha}{2}\tan\frac{\alpha}{2}}\big)+\big(a_1+a_2\cos\alpha\big)l\dot{\omega}\Big]\frac{\mathbf{e}_{\theta_1}}{a_0+a_1+a_2} \\
&= -\Big[\frac{\dot{v}_1}{4\pi l^2}\big[a_0+a_1+a_2\big(\cos\alpha+\frac{1}{4\sin\frac{\alpha}{2}}\big)\big]+\frac{\dot{v}_2}{4\pi l^2}\big[a_0\cos\alpha+a_1\big(1-\frac{1}{4\sin\frac{\alpha}{2}}\big)+a_2\cos\alpha\big] \\
&\quad -a_2 l\dot{\omega}\sin\alpha\Big]\frac{\cos\omega\mathbf{e}_x+\sin\omega\mathbf{e}_y}{a_0+a_1+a_2} \\
&\quad -\Big[\frac{a_2\dot{v}_1}{4\pi l^2}\sin\alpha\big(1-\frac{1}{8\sin^3\frac{\alpha}{2}}\big)+\frac{\dot{v}_2}{4\pi l^2}\big(a_0\sin\alpha+a_2\sin\alpha+\frac{a_1}{4\sin\frac{\alpha}{2}\tan\frac{\alpha}{2}}\big) \\
&\quad +\big(a_1+a_2\cos\alpha\big)l\dot{\omega}\Big]\frac{-\sin\omega\mathbf{e}_x+\cos\omega\mathbf{e}_y}{a_0+a_1+a_2} \qquad (3.11)
\end{aligned}$$

where $\omega(t)=\int_0^t\dot{\omega}\;dt$, and $\dot{\omega}$ is given in equation (3.10).

3.2 Simulation results of rotation and translation

Consider a full cycle consisting of four steps:

1. the zeroth and first spheres exchange volume with $\dot{v}_0=-\dot{v}_1=u_1$, where $u_1>0$ is some constant independent of t, and $\dot{v}_2=0$;
2. the zeroth and second spheres exchange volume with $\dot{v}_0=-\dot{v}_2=u_2$, where $u_2>0$ is some constant independent of t, and $\dot{v}_1=0$;
3. the zeroth and first spheres exchange volume with $\dot{v}_0=-\dot{v}_1=-u_1$, and $\dot{v}_2=0$;
4. the zeroth and second spheres exchange volume with $\dot{v}_0=-\dot{v}_2=-u_2$, and $\dot{v}_1=0$.

Assume that each step lasts for time T. Suppose that the initial conditions of the radii of the spheres are

$$a_1^0=a_2^0=a,\qquad a_0^0=r^{1/3}a\qquad\text{and}\qquad v=\frac{4\pi a^3}{3}$$

Also assume that $u_1T=s_1v$ and $u_2T=s_2v$. Figure 3.4 shows the rotation $4\pi l^3\omega(\bar{t})/v$ within one full cycle with $r=2$ and $s_1=s_2=0.9$ for different values of α, where

$\bar{t} = t/T$ is the scaled time. And in Figure 3.5 we show the relation between the net rotation Ω after a full cycle and the angle α between the two arms for $\alpha \in [\pi/6, \pi]$, also with $r = 2$ and $s_1 = s_2 = 0.9$.

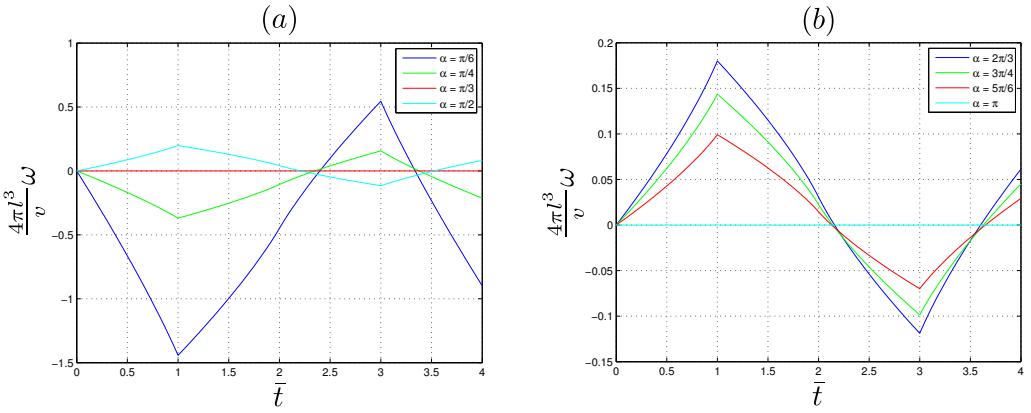

Figure 3.4: The rotation $4\pi l^3\omega(\bar{t})/v$ within one cycle with $r = 2$ and $s_1 = s_2 = 0.9$ for different values of α.

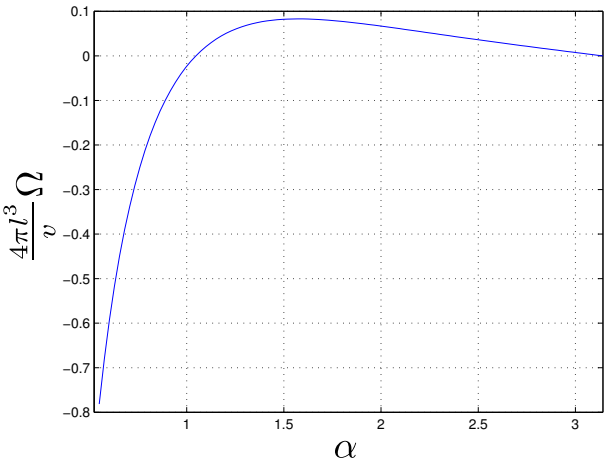

Figure 3.5: Net rotation $4\pi l^3\Omega(\alpha)/v$ with $r = 2$ and $s_1 = s_2 = 0.9$.

Next, let $\mathbf{\Delta}$ be the position of the center of sphere 0 after a cycle, i.e., $\mathbf{\Delta} = \int_0^{4T} \mathbf{U}_0\, dt$. From Figure 3.4 we see that ω scales like $v/l^3 \sim a^3/l^3$ which is of order ε^3, thus in equation (3.11) we may have the approximation:

$$\cos\omega\mathbf{e}_x + \sin\omega\mathbf{e}_y \sim \mathbf{e}_x \qquad -\sin\omega\mathbf{e}_x + \cos\omega\mathbf{e}_y \sim \mathbf{e}_y$$

Transform the global Cartesian coordinate $\{\mathbf{0}; \mathbf{e}_x, \mathbf{e}_y\}$ into the global polar coordinate $\{\mathbf{0}; \mathbf{e}_r, \mathbf{e}_\theta\}$ and express $\mathbf{\Delta}$ in this polar coordinate system as $\mathbf{\Delta} = R\mathbf{e}_r + \Theta\mathbf{e}_\theta$. Figure 3.6 shows the relation between $\mathbf{\Delta}$ and α for $\alpha \in [\pi/6, \pi]$ with $r = 2$ and $s_1 = s_2 = 0.9$, where Figure 3.6 (a) gives $4\pi l^2 R(\alpha)/v$ and Figure 3.6 (b) gives $\Theta(\alpha)$. Here to guarantee the continuity of Θ, we take its value in $[-2\pi, 0]$.

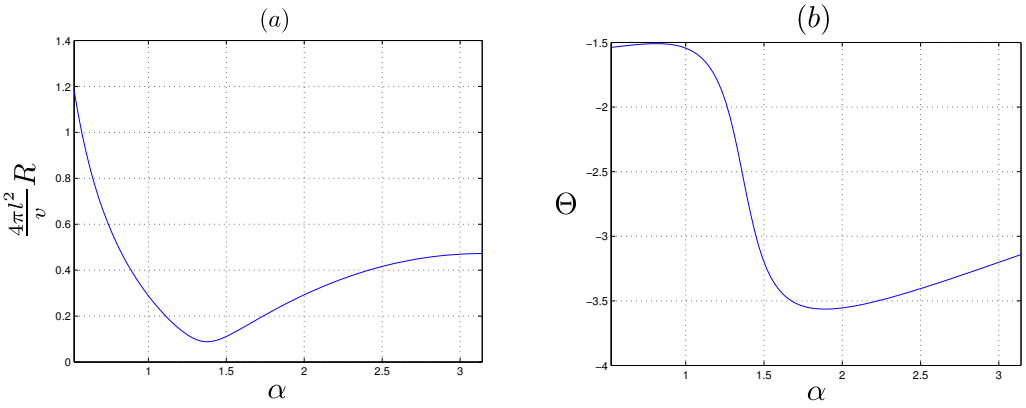

Figure 3.6: Net translation $\mathbf{\Delta}(\alpha) = R(\alpha)\mathbf{e}_r + \Theta(\alpha)\mathbf{e}_\theta$: (a) $4\pi l^2 R(\alpha)/v$; (b) $\Theta(\alpha)$.

3.3 Conclusions

From Figure 3.5 and Figure 3.6 we observe that:

1. There are two zeros of $\Omega(\alpha)$, one at $\alpha = \pi/3$ and the other at $\alpha = \pi$. For the former, the structure is an equilateral triangle. Hence we may draw an interesting conclusion for our model that *when the three spheres constitute an equilateral triangle, the swimmer does not rotate*; for the latter, the structure becomes linear and degenerates to the model we discussed in Chapter 2.

2. $\Omega < 0$ when $\alpha < \pi/3$, which indicates that the swimmer rotates clockwise, and $|\Omega|$ increases rapidly as α decreases, as long as $a_i/l\alpha \ll 1$; and $\Omega > 0$ when $\pi/3 < \alpha < \pi$, indicates that the swimmer rotates counterclockwise, and $4\pi l^3|\Omega|/v$ has a maximum value of about 0.0830 at $\alpha = \pi/2$.

3. Notice that the y-axis in Figure 3.5 is $4\pi l^3\Omega/v$, under the assumption that $\varepsilon \sim a_i/l \ll 1$, we concludes that $\Omega \sim O(\varepsilon^3)$ with α satisfying $a_i/l\alpha \ll 1$. This

implies that even the general 3-sphere model may indeed rotate in continuous cyclic deformations, however the effect of rotation is not obvious, comparing with the other rotating low Reynolds number swimmers, for example, the Purcell's rotater [57] and the generalized 3-sphere swimmer constructed in [56]. Moreover, comparing to that $\Theta \sim O(1)$ from Figure 3.6 (b), we conclude that though our model is a planar one, there is not much rotation involved in its swimming and the swimming trajectory is almost a line along the direction determined by Θ, while for other rotational swimmers, their motions involve large rotation. The reason lies behind might be that in our model we hold the angle α fixed, and the rotation of the swimmer only relies on the volume exchanging between spheres, while in their models α is allowed to change.

4. α has complicated effects on both the translation distance and the translation direction. $4\pi l^2 R/v$ has a minimum of about 0.0884 at around $\alpha = 1.3875(\approx 0.44\pi)$; while Θ has a maximum of about -0.48π at around $\alpha = 0.8116(\approx 0.26\pi)$, and a minimum of about -1.13π at around $\alpha = 1.8850(\approx 0.60\pi)$.

Though these four conclusions are derived from the prescribed swimming strokes given at the beginning of Section 3.2 with variables taken as $r = 2$ and $s_1 = s_2 = 0.9$, most part of these conclusions can be derived directly from equation (3.10) and equation (3.11) as shown below.

First from equation (3.10), we see that $\dot{\omega} \equiv 0$ when $\alpha = 0$ or $\alpha = \pi/3$, and from the initial condition $\omega(0) = 0$, we have $\omega \equiv 0$. Hence we conclude that:

Conclusion 4. *Any linear or equilateral triangular swimmer cannot rotate at any time.*

Next, equation (3.10) can be written as

$$\frac{d\omega}{dt} = \frac{\sin\alpha}{l^3}\Big(\frac{1}{8\sin^3\frac{\alpha}{2}} - 1\Big)\frac{a_0 a_1 a_2}{a_0(a_1+a_2) + 2a_1a_2(1-\cos\alpha)}\Big(a_1\frac{d}{dt}a_1 - a_2\frac{d}{dt}a_2\Big)$$

Thus we have the relation between the differential rotation $\bar{d}\omega$ and the differential controls (da_1, da_2):

$$\bar{d}\omega = \frac{\sin\alpha}{l^3}\Big(\frac{1}{8\sin^3\frac{\alpha}{2}} - 1\Big)\frac{a_0 a_1 a_2}{a_0(a_1+a_2) + 2a_1a_2(1-\cos\alpha)}\Big(a_1 da_1 - a_2 da_2\Big) \qquad (3.12)$$

Here $\bar{d}\omega > 0$ represents an infinitesimal rotation counterclockwise. The bar in $\bar{d}\omega$ stresses that the differential rotation does not integrate to a function $\omega(a_1, a_2)$. Using Stokes' theorem of elementary calculus, the swimming rotation $\delta\omega$ associated to an infinitesimal closed loop is

$$\delta\omega = \phi(a_1\partial_{a_2} + a_2\partial_{a_1})\psi \; da_2 \wedge da_1 \tag{3.13}$$

where

$$\begin{aligned} \phi(\alpha) &= \frac{\sin\alpha}{l^3}\Big(\frac{1}{8\sin^3\frac{\alpha}{2}} - 1\Big) \\ \psi(a_1, a_2; \alpha) &= \frac{a_0 a_1 a_2}{a_0(a_1 + a_2) + 2a_1 a_2(1 - \cos\alpha)} \end{aligned}$$

In equation (3.13), $da_2 \wedge da_1$ denotes the signed area enclosed by the loop. From equation (3.13), we see that the sign of $\delta\omega$ is decided by three parts: ϕ, $(a_1\partial_{a_2} + a_2\partial_{a_1})\psi$ and $da_2 \wedge da_1$. We claim that:

Conclusion 5. *If the loop is chosen so that $da_2 \wedge da_1 < 0$ and $|2(1-\cos\alpha)\frac{a_1^2 a_2^2}{a_0^4}| < 1$ always holds during the stroke, then the swimmer rotates clockwise when $\alpha < \pi/3$ (α should be chosen so that $a_i/l\alpha \ll 1$), and it rotates counterclockwise when $\pi/3 < \alpha < \pi$.*

Proof. Here we only need to show that $\partial_{a_2}(a_1\psi) + \partial_{a_1}(a_2\psi) > 0$ if $|2(1-\cos\alpha)\frac{a_1^2 a_2^2}{a_0^4}| < 1$ always holds during the stroke.

$$\begin{aligned} \partial_{a_2}(a_1\psi) &= \partial_{a_2}\frac{a_0 a_1^2 a_2}{a_0(a_1 + a_2) + 2(1-\cos\alpha)a_1 a_2} \\ &= \frac{1}{a_0(a_1 + a_2) + 2(1-\cos\alpha)a_1 a_2}\Big[-\frac{a_1^2 a_2^3}{a_0^2} + a_0 a_1^2 \\ &\quad -\frac{a_0 a_1^2 a_2}{a_0(a_1 + a_2) + 2(1-\cos\alpha)a_1 a_2}\big(-\frac{a_2^2}{a_0^2}(a_1 + a_2) + a_0 + 2(1-\cos\alpha)a_1\big)\Big] \end{aligned}$$

$$\begin{aligned} \partial_{a_1}(a_2\psi) &= \partial_{a_1}\frac{a_0 a_1 a_2^2}{a_0(a_1 + a_2) + 2(1-\cos\alpha)a_1 a_2} \\ &= \frac{1}{a_0(a_1 + a_2) + 2(1-\cos\alpha)a_1 a_2}\Big[-\frac{a_1^3 a_2^2}{a_0^2} + a_0 a_2^2 \\ &\quad -\frac{a_0 a_1 a_2^2}{a_0(a_1 + a_2) + 2(1-\cos\alpha)a_1 a_2}\big(-\frac{a_1^2}{a_0^2}(a_1 + a_2) + a_0 + 2(1-\cos\alpha)a_2\big)\Big] \end{aligned}$$

So we have

$$\begin{aligned} & \partial_{a_2}(a_1\psi) + \partial_{a_1}(a_2\psi) \\ = \quad & \frac{a_0^2(a_1+a_2)}{(a_0(a_1+a_2)+2(1-\cos\alpha)a_1a_2)^2}\Big[a_1^2+a_2^2-a_1a_2\big(1+2(1-\cos\alpha)\frac{a_1^2a_2^2}{a_0^4}\big)\Big] \quad (3.14) \end{aligned}$$

Obviously, when $|2(1-\cos\alpha)\frac{a_1^2a_2^2}{a_0^4}| < 1$, we have

$$\Big|a_1a_2\big(1+2(1-\cos\alpha)\frac{a_1^2a_2^2}{a_0^4}\big)\Big| < 2|a_1a_2| \le a_1^2+a_2^2$$

hence $\partial_{a_2}(a_1\psi) + \partial_{a_1}(a_2\psi) > 0$.

□

Conclusion 6. *With α satisfying $a_i/l\alpha \ll 1$, we have the approximation*

$$\delta\omega \sim \frac{\varepsilon}{l^2}\sin\alpha\Big(\frac{1}{8\sin^3\frac{\alpha}{2}}-1\Big)|da_2\wedge da_1| \quad (3.15)$$

Since we assume that $\varepsilon \ll 1$, equation (3.15) implies that the net rotation $\delta\omega$ after a stroke may be very small. However, either increasing a_i or increasing the stroke amplitude $|da_2\wedge da_1|$ will increase the net rotation $\delta\omega$ of a stroke.

Proof. From equation (3.14), we have $(a_1\partial_{a_2}+a_2\partial_{a_1})\psi \sim a^3$. Thus from equation (3.13), under the assumption $a/l \sim \varepsilon$, we have

$$\delta\omega \sim \frac{\varepsilon}{l^2}\sin\alpha\Big(\frac{1}{8\sin^3\frac{\alpha}{2}}-1\Big)|da_2\wedge da_1|$$

Under the assumption that $a_i/l\alpha \ll 1$, the function $\sin\alpha\Big(\frac{1}{8\sin^3\frac{\alpha}{2}}-1\Big)$ is bounded, so we have

$$|\delta\omega| < \frac{\varepsilon M}{l^2}|da_2\wedge da_1| < \varepsilon M\frac{a^2}{l^2} \sim O(\varepsilon^3) \quad (3.16)$$

which indicates that the net rotation $\delta\omega$ after a stroke is small. □

From Conclusion 6 we see that with $a/l \sim \varepsilon \ll 1$, the swimming trajectory of our planar swimmer is nearly a line. However equation (3.16) indicates that to exaggerate the rotation effect of the swimmer we should increase the ratio a/l, which may result in a curly trajectory that lies in a plane.

Finally we want to study the relation between the efficiency e defined by equation (2.11) and the angle α between the two connecting arms. As we mentioned in Chapter 2, in the planar case we have $X = |\mathbf{\Delta}|$. Hence $X = R$ which is given by Figure 3.6 (a), i.e.,

$$\frac{1}{3}e(\gamma;\alpha) = \frac{6\pi\mu R^2(\gamma;\alpha)}{\tau \int_0^\tau P(\gamma)dt} \tag{3.17}$$

Notice from equation (2.10) that the power P relies on the prescribed stroke γ and the angle α between the two connecting arms does not appear in equation (2.10) explicitly. Hence in equation (3.17) the only term that depends on α is R^2. This observation indicates that $e(\alpha)$ should have square behavior of $R(\alpha)$ up to a scale. Figure 3.7 shows the relation between efficiency e and the angle α for $r = 2$ and $s_1 = s_2 = 0.9$, and a comparison of Figure 3.7 with Figure 3.6 (a) may validate our conclusion.

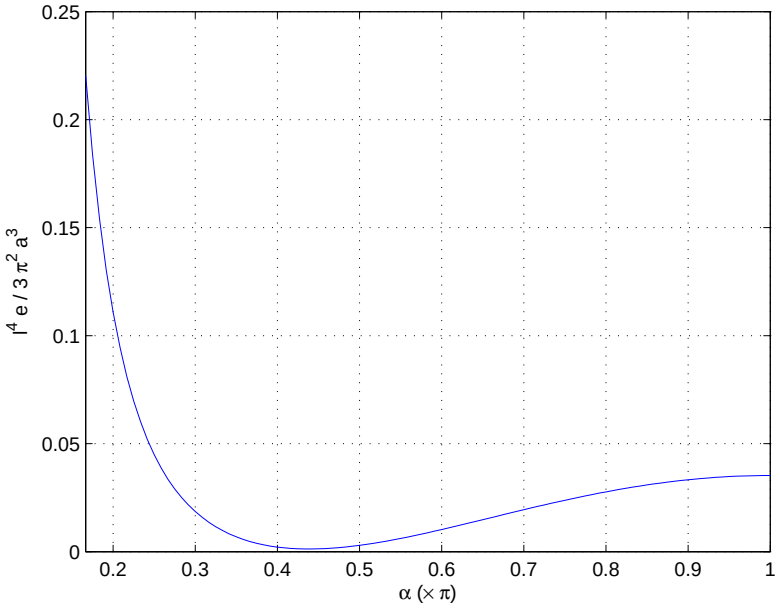

Figure 3.7: Relation between efficiency e and the angle α between the two connecting arms.

Chapter 4

A Deformable Sphere in Linear Maxwell Viscoelastic Flows

To date, a lot has been done to investigate the swimming behavior of various kinds of microorganisms in low Reynolds number Newtonian fluids. However as we briefly mentioned in Chapter 1, biological fluids are often laden with polymers. "When a polymer solution is subject to shear, the polymers stretch out. The resulting loss of entropy of the polymers leads to an effective elastic force tending to recover the initial configuration of the polymers [27]." We start by considering linear Maxwell viscoelastic (LMV) fluids, and we immerse our linked three-spheres models as introduced in Chapter 2 and Chapter 3 in a viscoelastic fluid so as to understand how viscoelasticity effects the swimming behavior of the microorganisms. The first step would be to understand the mechanics of a translating deformable sphere in an LMV flow and establish a reasonable analytical framework so that we could compare the swimming behaviors in a Newtonian Stokes fluid and an LMV fluid.

In Section 1.2 we discussed the mechanics of low Reynolds number Newtonian flows. In general, a low Reynolds number flow is governed by the Stokes equation:

$$\nabla \cdot \sigma(\mathbf{x}, t) = 0, \qquad \nabla \cdot \mathbf{u}(\mathbf{x}, t) = 0 \tag{4.1}$$

where $\mathbf{u}$ is the velocity field and σ the stress tensor. Here $\mathbf{x}$ is measured in a fixed global Cartesian reference frame $\{\mathbf{0}; \mathbf{e}_{x_1}, \mathbf{e}_{x_2}, \mathbf{e}_{x_3}\}$. The stress tensor σ is given by

$$\sigma(\mathbf{x}, t) = -p(\mathbf{x}, t)\mathbf{I} + \tau(\mathbf{x}, t)$$

where $p(\mathbf{x},t)$ is the pressure, $\mathbf{I}$ is the identity matrix and $\tau(\mathbf{x},t)$ is the deviatoric stress tensor. In Newtonian fluids, τ is given as

$$\tau = \mu\big[\nabla\mathbf{u} + (\nabla\mathbf{u})^T\big] \tag{4.2}$$

To make reasonable comparison between Newtonian fluids and LMV fluids, we follow the strategy established by Curtis and Gaffney [63]. Define an operator $\mathcal{L}$ as

$$\mathcal{L} := \mathbf{I}\big(1 + \lambda\frac{\partial}{\partial t}\big) \tag{4.3}$$

where λ is the viscoelastic relaxation time. The linear Maxwell viscoelasticity model is defined by the relation

$$\mathcal{L}\big[\tau\big] = \mu\big[\nabla\mathbf{u} + (\nabla\mathbf{u})^T\big] \tag{4.4}$$

Notice that when $\lambda = 0$, equation (4.4) reduces to equation (4.2) and equations (4.1) reduce to the Stokes equations (1.2) for Newtonian fluids. Now apply the operator $\mathcal{L}$ to the first equation in equation (4.1) for σ to obtain

$$-\mathcal{L}\big[\nabla p\big] + \mu\nabla^2\mathbf{u} = 0, \qquad \nabla\cdot\mathbf{u} = 0 \tag{4.5}$$

Curtis and Gaffney introduced Newtonian variables [63]:

$$\begin{cases} \mathbf{u}(\mathbf{x},t) = \mathbf{u}^{\mathrm{Newt}}(\mathbf{x},t) \\ \mathcal{L}\big[p(\mathbf{x},t)\big] = p^{\mathrm{Newt}}(\mathbf{x},t) \\ \mathcal{L}\big[\sigma(\mathbf{x},t)\big] = -\mathcal{L}\big[p\big]\mathbf{I} + \mathcal{L}\big[\tau\big] = \sigma^{\mathrm{Newt}}(\mathbf{x},t) \end{cases} \tag{4.6}$$

which allow us to map the LMV flow onto a Newtonian Stokes flow with the same dynamic viscosity and fluid density that is moving with velocity $\mathbf{u}^{\mathrm{Newt}}$ and pressure p^{Newt} satisfying the Stokes equations for a Newtonian Stokes flow.

Suppose that a deformable sphere is immersed in an LMV Stokes flow which is static at infinity, i,e,

$$\mathbf{u}(\mathbf{x}\to\infty,t) = 0 \tag{4.7}$$

Suppose that the sphere starts at the origin and moves along the $\mathbf{e}_{x_1}$ direction with the velocity given by $\mathbf{U}(t) = U(t)\mathbf{e}_{x_1}$. Thus at time t, the center of the sphere is at

$\mathbf{x}_0(t) = \int_0^t \mathbf{U}(\xi)d\xi$. Moreover, we suppose that the sphere is deformable but only in the radial direction, and that at time t the radius of the deformable sphere is $a(t)$. Hence the boundary condition is given as:

$$\mathbf{u}(\mathbf{x}, t) = \mathbf{U}(t) + \dot{a}(t)\mathbf{n} \qquad \text{at} \qquad \left|\mathbf{x} - \mathbf{x}_0(t)\right| = a(t) \tag{4.8}$$

where

$$\mathbf{n} = \frac{\mathbf{x} - \mathbf{x}_0(t)}{|\mathbf{x} - \mathbf{x}_0(t)|}$$

is the outward normal vector on the boundary. Equations (4.5, 4.7, 4.8) together constitute the no-slip boundary condition problem.

A problem arises when we try to solve this boundary value problem: integrals with respect to time t are necessarily involved in the solution to the Stokes equations (4.5), hence we need to ensure that the integrals are always kept in the fluid domain so that they are well-defined. Yet here the fluid domain is always changing and if we consider the problem in the fixed reference frame $(\mathbf{x}, t)$ it would be ill-posed. Instead we consider a body frame $(\mathbf{X}, s)$ that is fixed to the sphere as shown in Figure 4.1, where s measures time in the body frame. The reason why we use a different notation for time in the body frame will be clear in Section 4.1, where we discuss the transformation relation between the two frames following the framework established in [64]. With the mechanics properly settled in the body frame $(\mathbf{X}, s)$, we move on to investigate how the viscoelasticity of the flow affects the mechanical behavior of this translating deformable sphere. As we said earlier, equations (4.6) set up a criteria that allow us to compare Newtonian fluids and LMV fluids. As for this particular translating deformable sphere problem, we are interested in the forces that the fluids exert on the sphere. In Section 4.2 we give the criteria of force comparison based on the relations given in the equation system (4.6).

At this point, for study of swimming in LMV flows we only accomplish the setup of the analytical framework as we introduced above. Other work will be discussed in Chapter 9.

4.1 Transformation of the flows

According to the geometry of the problem, we fix the origin of the body frame to the center of the sphere $\mathbf{x}_0$ as shown in Figure 4.1. The transformation relation between

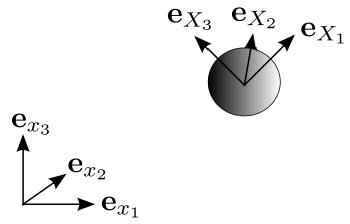

Figure 4.1: Global reference frame $(\mathbf{x}, t)$ and the body frame $(\mathbf{X}, s)$ on the deformable sphere.

the body frame $(\mathbf{X}, s)$ and the reference frame $(\mathbf{x}, t)$ is:

$$\begin{cases} s = t \\ \mathbf{X} = \dfrac{\mathbf{x} - \mathbf{x}_0(t)}{a(t)} = \dfrac{\mathbf{x} - \int_0^t \mathbf{U}(\xi)\ d\xi}{a(t)} \end{cases} \tag{4.9}$$

and the transformation relation between the spatial and time derivatives are given by [64]:

$$\begin{cases} \dfrac{\partial}{\partial t} = \dfrac{\partial}{\partial s} + \dfrac{\partial \mathbf{X}}{\partial t} \cdot \nabla_{\mathbf{X}} = \dfrac{\partial}{\partial s} - \dfrac{1}{a}\big(\mathbf{U} + \dot{a}\mathbf{X}\big) \cdot \nabla_{\mathbf{X}} \\ \nabla = \dfrac{1}{a}\nabla_{\mathbf{X}} \end{cases} \tag{4.10}$$

Notice from equation systems (4.9,4.10) that though time is scaled the same in both frames, the time derivatives are different up to a convective term. Hence to avoid non-necessary misunderstandings and confusions, we use different notations for time in the two frames. And the operator $\mathcal{L}$ defined in equation (4.3) transforms into:

$$\mathcal{L}_{\mathbf{X}} = \mathcal{L}_s - \frac{\lambda}{a}\mathbf{I}\Big[\big(\mathbf{U} + \dot{a}\mathbf{X}\big) \cdot \nabla_{\mathbf{X}}\Big] \tag{4.11}$$

where $\mathcal{L}_s = \mathbf{I}(1 + \lambda\partial_s)$.

Hereafter a physical quantity with superscript "$*$" refers to the flow in the body frame $(\mathbf{X}, s)$, while one without the superscript means it is directly transformed from the reference frame $(\mathbf{x}, t)$. For example, the velocity field of the fluid $\mathbf{u}(\mathbf{x}, t)$, when transformed into the body frame $(\mathbf{X}, s)$ according to the equation system (4.9), becomes

$$\mathbf{u}(\mathbf{X}, s) := \mathbf{u}\big(\mathbf{x}(\mathbf{X}, s), t(\mathbf{X}, s)\big) = \mathbf{u}\big(\mathbf{x}(\mathbf{X}, s), s\big)$$

However if we consider the flow in the body frame $(\mathbf{X}, s)$, its velocity field should be

$$\begin{aligned} \mathbf{u}^*(\mathbf{X}, s) &= \frac{d\mathbf{X}}{ds} = \frac{d\mathbf{X}}{dt}\frac{dt}{ds} + \nabla\mathbf{X}\cdot\frac{d\mathbf{x}}{ds} \\ &= \frac{d}{dt}\mathbf{X}(\mathbf{x}, t) = \frac{\mathbf{u}(\mathbf{X}, s) - \mathbf{U}}{a} - \frac{\dot{a}}{a}\mathbf{X} \end{aligned} \tag{4.12}$$

or equivalently

$$\mathbf{u}(\mathbf{X}, s) = a\mathbf{u}^*(\mathbf{X}, s) + \dot{a}\mathbf{X} + \mathbf{U}$$

Therefore the boundary condition equations (4.7, 4.8) become

$$\begin{cases} \mathbf{u}^*(\mathbf{X}, s) = 0 \qquad \text{at} \qquad |\mathbf{X}| = 1 \\ \mathbf{u}^*(\mathbf{X} = \infty, s) = -\dfrac{1}{a}\mathbf{U}(s) - \dfrac{\dot{a}}{a}\mathbf{X} \end{cases} \tag{4.13}$$

Now we consider the transformation of the pressure p, stress tensor σ and the deviatoric stress tensor τ. For pressure, naturally we have $p^*(\mathbf{X}, s) = p(\mathbf{X}, s)$. For the deviatoric stress tensor τ, according to equation (4.4), to determine the transformation of τ we only need to consider the right hand-side of equation (4.4), i.e., $\mu[\nabla\mathbf{u} + (\nabla\mathbf{u})^T]$. We have

$$\nabla\mathbf{u}\big(\mathbf{x}, t\big) = \frac{1}{a}\nabla_{\mathbf{X}}\Big[a\mathbf{u}^*\big(\mathbf{X}, s\big) + \dot{a}\mathbf{X} + \mathbf{U}(s)\Big] = \nabla_{\mathbf{X}}\mathbf{u}^*\big(\mathbf{X}, s\big) + \frac{\dot{a}}{a}\mathbf{I}$$

where $\mathbf{I}$ is the identity matrix. Hence

$$\begin{aligned} \mathcal{L}\big[\tau(\mathbf{x}, t)\big] &= \mu\Big[\nabla\mathbf{u}\big(\mathbf{x}, t\big) + \Big(\nabla\mathbf{u}\big(\mathbf{x}, t\big)\Big)^T\Big] = \mu\Big[\nabla_{\mathbf{X}}\mathbf{u}^*\big(\mathbf{X}, s\big) + \Big(\nabla_{\mathbf{X}}\mathbf{u}^*\big(\mathbf{X}, s\big)\Big)^T\Big] + 2\mu\frac{\dot{a}}{a}\mathbf{I} \\ &= \mathcal{L}_{\mathbf{X}}\big[\tau^*\big(\mathbf{X}, s\big)\big] + 2\mu\frac{\dot{a}}{a}\mathbf{I} \end{aligned} \tag{4.14}$$

which naturally leads to the transformation of the stress tensor σ:

$$\begin{aligned} \mathcal{L}\big[\sigma(\mathbf{x}, t)\big] &= -\mathcal{L}\big[p(\mathbf{x}, t)\big]\mathbf{I} + \mathcal{L}\big[\tau(\mathbf{x}, t)\big] = -\mathcal{L}_{\mathbf{X}}\big[p^*\big(\mathbf{X}, s\big)\big]\mathbf{I} + \mathcal{L}_{\mathbf{X}}\big[\tau^*\big(\mathbf{X}, s\big)\big] + 2\mu\frac{\dot{a}}{a}\mathbf{I} \\ &= \mathcal{L}_{\mathbf{X}}\big[\sigma^*\big(\mathbf{X}, s\big)\big] + 2\mu\frac{\dot{a}}{a}\mathbf{I} \end{aligned} \tag{4.15}$$

Finally we consider the transformation of equation (4.5). A direct calculation shows that:

$$-\mathcal{L}_{\mathbf{X}}\big[\frac{1}{a}\nabla_{\mathbf{X}}p^*\big] + \frac{\mu}{a}\nabla^2_{\mathbf{X}}\mathbf{u}^*(\mathbf{X}, s) = 0 \tag{4.16}$$

$$\nabla_{\mathbf{X}}\cdot\mathbf{u}^*(\mathbf{X}, s) = -3\frac{\dot{a}}{a} \tag{4.17}$$

In particular, notice that the right hand-side of equation (4.17) does not vanish, which indicates that the velocity field $\mathbf{u}^*(\mathbf{X}, s)$ does not satisfy the incompressibility condition. This can be easily understood from the boundary condition equation (4.13), where the $-\dot{a}a^{-1}\mathbf{X}$ term necessarily leads to the compressibility.

At the end of this Chapter we list all the transformation relations in Table 4.1 and the comparisons between the reference frame $(\mathbf{x}, t)$ and the body frame $(\mathbf{X}, s)$ in Table 4.2.

4.2 Forces in Newtonian and LMV Stokes flows

Equation system (4.6) sets up a criteria that allows us to compare Newtonian flows with LMV flows. Now let us consider the forces that the fluid exert on the translating deformable sphere. Let $\mathbf{F}$ be the force that an LMV flow moving with velocity field $\mathbf{u}$ and pressure p exerting on the sphere, and $\mathbf{F}^{\text{Newt}}$ the one that a Newtonian flow with the same dynamic viscosity and fluid density moving with velocity $\mathbf{u}^{\text{Newt}}$ and pressure p^{Newt}, where $\mathbf{u}$, p, $\mathbf{u}^{\text{Newt}}$ and p^{Newt} are related by equation system (4.6). We have

$$\mathbf{F}(t) = \int_{\partial B(\mathbf{x}_0(t);a(t))} \sigma(\mathbf{x}, t) \cdot \mathbf{n} \, dS_{\mathbf{x}} \tag{4.18}$$

$$\mathbf{F}^{\text{Newt}}(t) = \int_{\partial B(\mathbf{x}_0(t);a(t))} \sigma^{\text{Newt}}(\mathbf{x}, t) \cdot \mathbf{n} \, dS_{\mathbf{x}} \tag{4.19}$$

or when evaluated in the body frame $(\mathbf{X}, s)$:

$$\mathbf{F}(s) = 4\pi a^2(s) \int_{\partial B(0;1)} \sigma(\mathbf{X}, s) \cdot \mathbf{n} \, dS_{\mathbf{X}} \tag{4.20}$$

$$\mathbf{F}^{\text{Newt}}(s) = 4\pi a^2(s) \int_{\partial B(0;1)} \sigma^{\text{Newt}}(\mathbf{X}, s) \cdot \mathbf{n} \, dS_{\mathbf{X}} \tag{4.21}$$

where $B(\mathbf{x}_0(t); a(t))$ is the ball in the reference frame that is centered at $\mathbf{x}_0(t)$ and has radius $a(t)$, $S_{\mathbf{x}}$ is the area element on the sphere $\partial B(\mathbf{x}_0(t); a(t))$, and σ, σ^{Newt} are the stress tensors of the LMV Stokes flow and the Newtonian Stokes flow. The relation between the forces is given in the follow Lemma:

Lemma 1.

$$\mathcal{L}\big[\mathbf{F}(t)\big] = \mathbf{F}^{Newt}(t) \tag{4.22}$$

Proof. Since the integrals in equations (4.20, 4.21) are changing with time t, which is involved in the operator $\mathcal{L}$ that is acting on the integrals, we consider the problem in the body frame $(\mathbf{X}, s)$ so to transform the integrals into integrals on a fixed boundary.

By equation (4.11), we have

$$\mathcal{L}_{\mathbf{X}}\big[\mathbf{F}(s)\big] = \mathcal{L}_s\big[\mathbf{F}(s)\big] - \frac{\lambda}{a}\mathbf{I}\Big[\big(\mathbf{U} + \dot{a}\mathbf{X}\big)\cdot\nabla_{\mathbf{X}}\Big]\circ\big[\mathbf{F}(s)\big]$$

Since $\mathbf{F}$ depends on time s only, the second term on the right hand-side of the above equation necessarily vanishes and

$$\begin{aligned}\mathcal{L}_{\mathbf{X}}[\mathbf{F}(s)] = \mathcal{L}_s[\mathbf{F}(s)] &= \mathbf{I}\big(1+\lambda\frac{\partial}{\partial s}\big)\circ\Big[4\pi a^2(s)\int_{\partial B(0,1)}\sigma\big(\mathbf{X},s\big)\cdot\mathbf{n}\;dS_{\mathbf{X}}\Big]\\ = \quad 4\pi a^2\int_{\partial B(0,1)}\sigma\cdot\mathbf{n}\;dS_{\mathbf{X}} &+ 8\pi a\dot{a}\lambda\int_{\partial B(0,1)}\sigma\cdot\mathbf{n}\;dS_{\mathbf{X}} + 4\pi a^2\int_{\partial B(0,1)}\big[\lambda\frac{\partial}{\partial s}\sigma\big]\cdot\mathbf{n}\;dS_{\mathbf{X}}\end{aligned}$$

The sum of the first and third terms in the above equation can be written as

$$4\pi a^2\int_{\partial B(0,1)}\mathcal{L}_s\big[\sigma\big]\cdot\mathbf{n}\;dS_{\mathbf{X}}$$

hence

$$\mathcal{L}_s\big[\mathbf{F}\big] = 4\pi a^2\int_{\partial B(0,1)}\mathcal{L}_s\big[\sigma\big]\cdot\mathbf{n}\;dS_{\mathbf{X}} + 8\pi a\dot{a}\lambda\int_{\partial B(0,1)}\sigma\cdot\mathbf{n}\;dS_{\mathbf{X}}$$

From equation (4.20) we notice that the second therm in the right hand-side of the above equation is

$$8\pi a\dot{a}\lambda\int_{\partial B(0,1)}\sigma\cdot\mathbf{n}\;dS_{\mathbf{X}} = 2\frac{\dot{a}}{a}\lambda\mathbf{F}$$

hence

$$\Big(\mathcal{L}_s - 2\frac{\dot{a}}{a}\lambda\mathbf{I}\Big)\circ\big[\mathbf{F}\big] = 4\pi a^2\int_{\partial B(0,1)}\mathcal{L}_s\big[\sigma\big]\cdot\mathbf{n}\;dS_{\mathbf{X}} \tag{4.23}$$

Moreover, again by equation (4.11) we have

$$\begin{aligned}&\int_{\partial B(0,1)}\mathcal{L}_s\big[\sigma\big]\cdot\mathbf{n}\;dS_{\mathbf{X}}\\ = \quad &\int_{\partial B(0,1)}\mathcal{L}_{\mathbf{X}}\big[\sigma\big]\cdot\mathbf{n}\;dS_{\mathbf{X}} + \frac{\lambda}{a}\int_{\partial B(0;1)}\Big[\mathbf{I}\Big(\big(\mathbf{U}+\dot{a}\mathbf{X}\big)\cdot\nabla_{\mathbf{X}}\Big)\sigma\Big]\cdot\mathbf{n}\;dS_{\mathbf{X}}\end{aligned} \tag{4.24}$$

For the first term in equation (4.24), from equations (4.6,4.21),

$$\int_{\partial B(0,1)} \mathcal{L}_{\mathbf{X}}\big[\sigma\big]\cdot\mathbf{n}\ dS_{\mathbf{X}} = \int_{\partial B(0,1)} \sigma^{\text{Newt}}\cdot\mathbf{n}\ dS_{\mathbf{X}} = \frac{\mathbf{F}^{\text{Newt}}}{4\pi a^2}$$

Hence equations (4.23,4.24) reduce to

$$\Big(\mathcal{L}_s - 2\frac{\dot a}{a}\lambda\mathbf{I}\Big)\circ\big[\mathbf{F}\big] = \mathbf{F}^{\text{Newt}} + 4\pi a\lambda\int_{\partial B(0;1)}\Big[\mathbf{I}\Big(\big(\mathbf{U}+\dot a\mathbf{X}\big)\cdot\nabla_{\mathbf{X}}\Big)\sigma\Big]\cdot\mathbf{n}\ dS_{\mathbf{X}} \quad (4.25)$$

Now let us consider the integral in equation (4.25). Let

$$I_1 = \int_{\partial B(0;1)}\Big[\mathbf{I}(\mathbf{U}\cdot\nabla_{\mathbf{X}})\sigma\Big]\cdot\mathbf{n}\ dS_{\mathbf{X}},\quad I_2 = \int_{\partial B(0;1)}\Big[\mathbf{I}(\mathbf{X}\cdot\nabla_{\mathbf{X}})\sigma\Big]\cdot\mathbf{n}\ dS_{\mathbf{X}}$$

Thus

$$\int_{\partial B(0;1)}\Big[\mathbf{I}\Big(\big(\mathbf{U}+\dot a\mathbf{X}\big)\cdot\nabla_{\mathbf{X}}\Big)\sigma\Big]\cdot\mathbf{n}\ dS_{\mathbf{X}} = I_1 + \dot a I_2 \quad (4.26)$$

First for I_1, we have

$$\mathbf{U}(s)\cdot\nabla_{\mathbf{X}} = \sum_{k=1}^{3} U_k(s)\frac{\partial}{\partial X_k}$$

so

$$I_1 = \sum_k U_k(s)\int_{\partial B(0;1)}\Big[(\mathbf{I}\frac{\partial}{\partial X_k})\sigma\Big]\cdot\mathbf{n}\ dS_{\mathbf{X}}$$

Consider the region $\Omega(0;R)$ enclosed by $\partial B(0;1)$ and $\partial B(0;R)$ for a large $R>1$ as shown in Figure 4.2. Apply the *Divergence Theorem* to the region $\Omega(0;R)$ and keep in mind that $\mathbf{n}$ always stands for the outward normal vector, hence for each k, we have

$$\begin{aligned}
&\int_{\partial B(0;1)}\Big[(\mathbf{I}\frac{\partial}{\partial X_k})\sigma\Big]\cdot\mathbf{n}\ dS_{\mathbf{X}}\\
=\ &-\int_{\Omega(0;R)}\nabla_{\mathbf{X}}\cdot\Big[(\mathbf{I}\frac{\partial}{\partial X_k})\sigma\Big]\ dV_{\mathbf{X}} + \int_{\partial B(0;R)}\Big[(\mathbf{I}\frac{\partial}{\partial X_k})\sigma\Big]\cdot\mathbf{n}\ dS_{\mathbf{X}}\\
=\ &-\int_{\Omega(0;R)}(\mathbf{I}\frac{\partial}{\partial X_k})\big(\nabla_{\mathbf{X}}\cdot\sigma\big)\ dV_{\mathbf{X}} + \int_{\partial B(0;R)}\Big[(\mathbf{I}\frac{\partial}{\partial X_k})\sigma\Big]\cdot\mathbf{n}\ dS_{\mathbf{X}}
\end{aligned}$$

Stokes equations ensure that $\nabla_{\mathbf{X}}\cdot\sigma\equiv 0$, hence the body integral on $\Omega(0;R)$ holds for arbitrarily large R. Let $R\to\infty$,

$$\int_{\partial B(0;1)}\Big[(\mathbf{I}\frac{\partial}{\partial X_k})\sigma\Big]\cdot\mathbf{n}\ dS_{\mathbf{X}} = \lim_{R\to\infty}\int_{\partial B(0;R)}\Big[(\mathbf{I}\frac{\partial}{\partial X_k})\sigma\Big]\cdot\mathbf{n}\ dS_{\mathbf{X}}$$

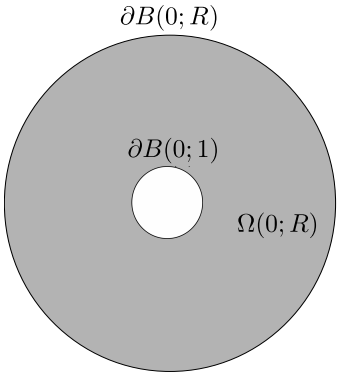

Figure 4.2: Illustration of the domain $\Omega(0;R)$.

To show that the integral on $\partial B(0;R)$ vanishes as $R \to \infty$, let us consider the force $\mathbf{F}_R$ exerted on the sphere $\partial B(\mathbf{x}_0; aR)$ in the reference frame, whose transformation in the body frame is just $\partial B(0;R)$. It is easily seen that

$$\mathbf{F}_R = \int_{\partial B(\mathbf{x}_0;aR)} \sigma \cdot \mathbf{n}\ dS_{\mathbf{x}} = 4\pi a^2 \int_{\partial B(0;R)} \sigma \cdot \mathbf{n}\ dS_{\mathbf{X}}$$

$\lim_{R\to\infty} \mathbf{F}_R < \infty$ [29] indicates that $\sigma \sim O(R^{-2})$. Hence

$$(\mathbf{I}\frac{\partial}{\partial X_k})\sigma \sim O(\frac{X_k}{R^4}) \sim O(\frac{1}{R^3})$$

and hence

$$\lim_{R\to\infty} \int_{\partial B(0;R)} \Big[(\mathbf{I}\frac{\partial}{\partial X_k})\sigma\Big] \cdot \mathbf{n}\ dS_{\mathbf{X}} = 0$$

which results in that $I_1 = 0$.

Next let us consider I_2, also by *Divergence theorem*,

$$\begin{aligned} I_2 &= \int_{\partial B(0;1)} \Big[\mathbf{I}(\mathbf{X}\cdot\nabla_{\mathbf{X}})\sigma\Big] \cdot \mathbf{n}\ dS_{\mathbf{X}} \\ &= -\int_{\Omega(0;R)} \nabla_{\mathbf{X}} \cdot \Big[\mathbf{I}(\mathbf{X}\cdot\nabla_{\mathbf{X}})\sigma\Big]\ dV_{\mathbf{X}} + \int_{\partial B(0;R)} \Big[\mathbf{I}(\mathbf{X}\cdot\nabla_{\mathbf{X}})\sigma\Big] \cdot \mathbf{n}\ dS_{\mathbf{X}} \end{aligned}$$

For the body integral, we have

$$\int_{\Omega(0;R)} \nabla_{\mathbf{X}} \cdot \Big[\mathbf{I}(\mathbf{X}\cdot\nabla_{\mathbf{X}})\sigma\Big]\ dV_{\mathbf{X}} = \int_{\Omega(0;R)} \Big[\nabla_{\mathbf{X}}\cdot\sigma + \mathbf{I}(\mathbf{X}\cdot\nabla_{\mathbf{X}})\big(\nabla_{\mathbf{X}}\cdot\sigma\big)\Big]\ dV_{\mathbf{X}}$$

hence it vanishes by the Stokes equations. Also take $R \to \infty$ and we obtain

$$I_2 = \lim_{R\to\infty} \int_{\partial B(0;R)} \Big[\mathbf{I}(\mathbf{X}\cdot\nabla_{\mathbf{X}})\sigma\Big]\cdot\mathbf{n}\; dS_{\mathbf{X}}$$

From the earlier discussion of σ for I_1, we may assume that

$$\sigma = \frac{\mathbf{C}(\theta,\varphi;t)}{R^2} + \widetilde{\sigma}(R,\theta,\varphi;t)$$

where $\widetilde{\sigma} \sim O(R^{-3})$ and (R,θ,φ) is the spherical coordinate for $\mathbf{X}$, $\mathbf{C}$ is the tensor coefficient of the leading term R^{-2}. And so

$$\lim_{R\to\infty}\frac{\mathbf{F}_R}{4\pi a^2} = \lim_{R\to\infty}\int_{\partial B(0;R)}\sigma\cdot\mathbf{n}\; dS_{\mathbf{X}} = \lim_{R\to\infty}\int_{\partial B(0;R)}\frac{\mathbf{C}(\theta,\varphi;t)\cdot\mathbf{n}}{R^2}\; dS_{\mathbf{X}} < \infty \quad (4.27)$$

On the other hand, we have

$$\mathbf{I}\Big(\mathbf{X}\cdot\nabla_{\mathbf{X}}\Big)\widetilde{\sigma} \sim O(R^{-3})$$

which indicates that

$$\lim_{R\to\infty}\int_{\partial B(0;R)}\Big[\mathbf{I}\Big(\mathbf{X}\cdot\nabla_{\mathbf{X}}\Big)\widetilde{\sigma}\Big]\cdot\mathbf{n}\; dS_{\mathbf{X}} = 0$$

hence

$$\begin{aligned}
I_2 &= \lim_{R\to\infty}\int_{\partial B(0;R)}\Big[\mathbf{I}\Big(\mathbf{X}\cdot\nabla_{\mathbf{X}}\Big)\sigma\Big]\cdot\mathbf{n}\; dS_{\mathbf{X}} \\
&= \lim_{R\to\infty}\int_{\partial B(0;R)}\Big[\mathbf{I}\Big(\mathbf{X}\cdot\nabla_{\mathbf{X}}\Big)\frac{\mathbf{C}(\theta,\varphi;t)}{R^2}\Big]\cdot\mathbf{n}\; dS_{\mathbf{X}} \\
&= \lim_{R\to\infty}\int_{\partial B(0;R)}\Big(R\frac{\partial}{\partial R}(\frac{1}{R^2})\Big)\Big(\mathbf{C}\cdot\mathbf{n}\Big)\; dS_{\mathbf{X}} \\
&= \lim_{R\to\infty}\int_{\partial B(0;R)}\Big(-\frac{2}{R^2}\Big)\Big(\mathbf{C}\cdot\mathbf{n}\Big)\; dS_{\mathbf{X}}
\end{aligned}$$

Comparing this with equation (4.27), it is readily seen that

$$I_2 = \lim_{R\to\infty}\int_{\partial B(0;R)}\Big[\mathbf{I}\Big(\mathbf{X}\cdot\nabla_{\mathbf{X}}\Big)\sigma\Big]\cdot\mathbf{n}\; dS_{\mathbf{X}} = -2\lim_{R\to\infty}\frac{\mathbf{F}_R}{4\pi a^2} \quad (4.28)$$

Finally, once again by divergence theorem,

$$\frac{\mathbf{F}}{4\pi a^2} = \int_{\partial B(0;1)}\sigma\cdot\mathbf{n}\; dS_{\mathbf{X}} = -\int_{\Omega(0;R)}\Big(\nabla_{\mathbf{X}}\cdot\sigma\Big)\; dV_{\mathbf{X}} + \int_{\partial B(0;R)}\sigma\cdot\mathbf{n}\; dS_{\mathbf{X}}$$

The body integral vanishes by Stokes equations, and the second integral is just $\mathbf{F}_R/(4\pi a^2)$. Hence $\mathbf{F} = \mathbf{F}_R$ and equation (4.28) leads to

$$I_2 = \lim_{R\to\infty} \int_{\partial B(0;R)} \Big[\mathbf{I}\Big(\mathbf{X}\cdot\nabla_{\mathbf{X}}\Big)\sigma\Big]\cdot\mathbf{n}\; dS_{\mathbf{X}} = -2\frac{\mathbf{F}}{4\pi a^2}$$

Finally, we bring our calculation results for I_1 and I_2 to equations (4.25.4.26):

$$\Big(\mathcal{L}_s - 2\frac{\dot{a}}{a}\lambda\mathbf{I}\Big)\circ\big[\mathbf{F}(s)\big] = \mathbf{F}^{\mathrm{Newt}}(s) - 2\frac{\dot{a}}{a}\lambda\mathbf{F}(s)$$

namely,

$$\mathcal{L}_s\big[\mathbf{F}(s)\big] = \mathbf{F}^{\mathrm{Newt}}(s)$$

Recall that since $\mathbf{F}$ depends on s only, we have $\mathcal{L}_{\mathbf{X}}[\mathbf{F}] = \mathcal{L}_{\mathbf{s}}[\mathbf{F}]$, finally we obtain equation (4.22). This we completes the proof.

□

Table 4.1: Transformation relations between $(\mathbf{x}, t)$ and $(\mathbf{X}, s)$.

Time	$s = t$
Space	$\mathbf{X} = \dfrac{\mathbf{x} - \int_0^t \mathbf{U}(\xi)\ d\xi}{a(t)}$
Velocity	$\mathbf{u}^*(\mathbf{X}, s) = \dfrac{\mathbf{u}(\mathbf{x}, t) - \mathbf{U}}{a} - \dfrac{\dot{a}}{a}\mathbf{X}$
Pressure	$p^*(\mathbf{X}, s) = p(\mathbf{x}, t)$
Deviatoric stress tensor	$\mathcal{L}_{\mathbf{X}}\big[\tau^*\big(\mathbf{X}, s\big)\big] = \mathcal{L}\big[\tau\big(\mathbf{x}, t\big)\big] - 2\mu\dfrac{\dot{a}}{a}\mathbf{I}$
Stress tensor	$\mathcal{L}_{\mathbf{X}}\big[\sigma^*\big(\mathbf{X}, s\big)\big] = \mathcal{L}\big[\sigma\big(\mathbf{x}, t\big)\big] - 2\mu\dfrac{\dot{a}}{a}\mathbf{I}$
Time derivative	$\dfrac{\partial}{\partial t} = \dfrac{\partial}{\partial s} - \dfrac{1}{a}\big(\mathbf{U} + \dot{a}\mathbf{X}\big) \cdot \nabla_{\mathbf{X}}$
Spatial derivative	$\nabla = \dfrac{1}{a}\nabla_{\mathbf{X}}$

Table 4.2: Comparison between $(\mathbf{x}, t)$ and $(\mathbf{X}, s)$.

	Reference frame $(\mathbf{x}, t)$	Body frame $(\mathbf{X}, s)$
Operator $\mathcal{L}$	$\mathcal{L} = \mathbf{I}\big(1 + \lambda\frac{\partial}{\partial t}\big)$	$\mathcal{L}_{\mathbf{X}} = \mathbf{I}\Big[1 + \lambda\frac{\partial}{\partial s} - \frac{\lambda}{a}\big(\mathbf{U} + \dot{a}\mathbf{X}\big)\cdot\nabla_{\mathbf{X}}\Big]$
Equations	$-\mathcal{L}\big[\nabla p\big] + \mu\nabla^2\mathbf{u} = 0$ $\nabla\cdot\mathbf{u} = 0$	$-\mathcal{L}_{\mathbf{X}}\big[\frac{1}{a}\nabla_{\mathbf{X}}p^*\big] + \frac{\mu}{a}\nabla^2_{\mathbf{X}}\mathbf{u}^*(\mathbf{X}, s) = 0$ $\nabla_{\mathbf{X}}\cdot\mathbf{u}^*(\mathbf{X}, s) = -3\frac{\dot{a}}{a}$
Boundary condition	$\mathbf{u}(\mathbf{x}, t) = \mathbf{U}(t) + \dot{a}(t)\mathbf{n}$ $\quad$ at $\big\lvert\mathbf{x} - \mathbf{x}_0(t)\big\rvert = a(t)$ $\mathbf{u}(\mathbf{x}\to\infty, t) = 0$	$\mathbf{u}^*(\mathbf{X}, s) = 0 \quad$ at $\big\lvert\mathbf{X}\big\rvert = 1$ $\mathbf{u}^*(\mathbf{X} = \infty, s) = -\frac{1}{a}\mathbf{U}(s) - \frac{\dot{a}}{a}\mathbf{X}$

Chapter 5

Mechanics of 2D Low Reynolds Number Swimming

So far our works have been restricted to prescribed shape deformations. Yet in reality, microorganisms including cells use a variety of shape deformations to swim at low Reynolds number. Therefore we seek methods that allow us to study more general shape deformations. We start from 2D problems. In this Chapter we will present a review of mechanics of 2D infinite Stokes flows using the powerful mathematical tool of complex analysis. Based on this analytical framework, later in Chapter 6 we develop a method that could quickly provide us a large variety of shape deformations on which we could apply analysis and computation.

5.1 2D infinite Stokes flows

As assumed in Chapter 1, suppose that at time t the cell occupies a simply-connected compact region $\Omega = \Omega(t)$ in the body frame, and thus the corresponding fluid domain should be $\Omega(t)^c = \mathbb{C}/\Omega(t)$ with the boundary $\partial\Omega(t)$. At low Reynolds number, the fluid mechanics is governed by the Stokes equations (1.2). For $2D$ problems, the incompressibility condition $\nabla \cdot \mathbf{u} = 0$ in equation (1.2) implies that we may introduce a stream function $\Lambda(z, \overline{z}; t)$ [29, 65, 31] on the fluid domain $\Omega(t)^c$ such that

$$u = \nabla \times \Lambda = \frac{\partial \Lambda}{\partial y} - i\frac{\partial \Lambda}{\partial x}$$

Here we use $u \in \mathbb{C}$ to denote the velocity field (originally denoted by $\mathbf{u}$ in previous chapters) in the complex z-plane. Then the Stokes equations (1.2) imply that Λ is a biharmonic equation:

$$\Delta^2 \Lambda = 0 \tag{5.1}$$

The general solution of equation (5.1) can be expressed by Goursat's formula [29, 65, 31]:

$$\Lambda(z, \overline{z}; t) = -\Im\big[\bar{z}\phi(z;t) + \chi(z;t)\big] \tag{5.2}$$

where for any t, $\phi(z;t)$ and $\chi(z;t)$ are analytic functions on the fluid domain $\mathbb{C}/\Omega(t)$ and continuous on $\mathbb{C}/\text{int}\Omega(t)$, where int$\Omega$ denotes the interior of Ω. $\phi(z;t)$ and $\chi(z;t)$ are often called as the ***Goursat functions***. The following proposition gives the expressions of complex velocity field $u \in \mathbb{C}$, pressure $p \in \mathbb{R}$ and vorticity $\omega \in \mathbb{R}$ with respect to the Goursat functions, where we eliminate t and denote ∂_z by $'$ for simplicity.

Proposition 1.

$$u = \phi(z) - z\overline{\phi'(z)} - \overline{\chi'(z)} \tag{5.3}$$

$$p = -4\mu\Re\{\phi'(z)\} \tag{5.4}$$

$$\omega = -4\Im\{\phi'(z)\} \tag{5.5}$$

where the vorticity ω is defined as

$$\omega = \frac{\partial}{\partial y}\Re v - \frac{\partial}{\partial x}\Im v$$

As stated in [66], the stress force at a point $z \in \partial\Omega$ is

$$f = 4\mu\Re(\phi')n - 2\mu(z\overline{\phi''} + \overline{\chi''})\overline{n} \tag{5.6}$$

where $n = -idz/ds$ is the exterior normal on $\partial\Omega$ (pointing to the fluid domain), s denotes the arclength, traversed counterclockwise. The differential form fds can be written as

$$fds = -2i\mu\big[(\phi' + \overline{\phi'})dz + (z\overline{\phi''} + \overline{\chi''})d\bar{z}\big] = -2i\mu d\big(\phi + z\overline{\phi'} + \overline{\chi'}\big) \tag{5.7}$$

For $2D$ Stokes flow in the unbounded domain $\mathbb{C}/\Omega(t)$, in order for the components of stress to be bounded at infinity, it is shown in [61, 65] that the Goursat functions must take the general form

$$\phi(z;t) = -\frac{X(t)+iY(t)}{2\pi(1+\kappa(t))}\log z + \Gamma(t)z + \widetilde{\phi}(z;t) \tag{5.8}$$

$$\psi(z;t) = \chi'(z;t) = \frac{X(t)-iY(t)}{2\pi(1+\kappa(t))}\log z + \Gamma'(t)z + \widetilde{\psi}(z;t) \tag{5.9}$$

where $\Gamma(t)$ and $\Gamma'(t)$ are complex constants with respect to z, and $\widetilde{\phi}(z;t)$ and $\widetilde{\psi}(z;t)$ are single-valued and analytic on $\overline{\mathbb{C}}/\Omega$ (where $\overline{\mathbb{C}} = \mathbb{C}\cup\{\infty\}$). We require that the stress vanish at infinity, thus $\Gamma(t)$ and $\Gamma'(t)$ should be both zero. For the logarithmic terms, as stated in [61], $(X(t), Y(t))$ comes from the resultant vector of external forces acting on the whole boundary $\partial\Omega$. In particular for the self-propulsion problem we have:

Lemma 2. *At time t, the system is force-free (i.e., $\int_{\partial\Omega(t)} f ds = 0$) if and only if $X(t) = Y(t) = 0$ in equations (5.8,5.9), i.e., the logarithmic terms in $\phi(z;t)$ and $\psi(z;t)$ vanish.*

This result is given in [61], and the reason can be seen from the last equality in equation (5.7) since

$$\phi + z\overline{\phi'} + \overline{\chi'} = C\Big[\overline{\log z} - \log z\Big] + \Big[\widetilde{\phi} + z\overline{\big(-\frac{C}{z} + \widetilde{\phi}'(z)\big)} + \overline{\widetilde{\psi}(z)}\Big]$$

When we take the integral of $f ds$ over $\partial\Omega$, the integral

$$\int_{\partial\Omega} d\big(\widetilde{\phi} + z\overline{\big(-\frac{C}{z} + \widetilde{\phi}'(z)\big)} + \overline{\widetilde{\psi}(z)}\big)$$

vanishes while $C\int_{\partial\Omega} d(\overline{\log z} - \log z)$ does not unless $C = 0$. Thus to ensure the force-free condition $\int_{\partial\Omega} f ds = 0$, we need the logarithmic terms in equations (5.8,5.9) vanish. Lemma 2 indicates that for 2D swimming problems, the Goursat functions $\phi(z)$ and $\psi(z)$ should be single-valued and analytic on $\overline{\mathbb{C}}/\Omega$, hence they should have Laurent expansions at infinity of the following form:

$$\phi(z;t) = a_0(t) + \frac{a_{-1}(t)}{z} + \frac{a_{-2}(t)}{z^2} + \cdots \tag{5.10}$$

$$\psi(z;t) = b_0(t) + \frac{b_{-1}(t)}{z} + \frac{b_{-2}(t)}{z^2} + \cdots \tag{5.11}$$

Hence the boundary condition problem as described above becomes: find functions $\phi(z;t)$ and $\psi(z;t)$ that are analytic on $\overline{\mathbb{C}}/\Omega(t)$ and continuous on $\overline{\mathbb{C}}/\text{int}\Omega(t)$ such that

$$\phi(z;t) - z\overline{\phi'(z;t)} - \overline{\psi(z;t)} = V(z,\overline{z};t) \qquad (z \in \partial\Omega(t)) \tag{5.12}$$

where $V(z,\overline{z};t)$ for $z \in \partial\Omega(t)$ is the velocity boundary condition determined by the shape changes, namely, the complex form of $\mathbf{u}_{\text{shape}}$ as introduced in Chapter 1.

5.2 Pull-back of the boundary condition problem

The classic way that most existing numerical methods (such as the *boundary integral method* [67] and the *integral equation method* [65]) treat equation (5.12) is to apply a certain integral operator directly to equation (5.12) and then parameterize the integral boundary. However since the problem here has a moving boundary, these methods may require large computational effort since usually a new parameterization at each time step is needed. Here we approach this particular moving boundary problem from another direction, that is, we pull back the problem from the z-plane as described in Section 5.1 to a fixed complex computational ζ-plane. The idea is similar to that in Chapter 4, but here we need certain techniques from complex analysis to complete the pull-back process.

As we assumed in Section 5.1, suppose that at instant t, the cell occupies a simply connected compact region $\Omega(t)$ in the complex z-plane. Let $D = \{\zeta \in \mathbb{C} : |\zeta| < 1\}$ be the unit disk in the computational ζ-plane. When we consider the regions exterior to $\overline{D}$ and that to $\Omega(t)$ in the extended complex planes $\overline{\mathbb{C}}/\overline{D}$ and $\overline{\mathbb{C}}/\Omega(t)$, it is easily seen that they are both simply-connected (though $\mathbb{C}/\overline{D}$ and $\mathbb{C}/\Omega(t)$ are not). The *Riemann mapping theorem* then ensures the existence of a single-valued analytic conformal mapping $z = w(\zeta;t)$ which maps $\mathbb{C}/\overline{D}$ one-to-one and onto $\mathbb{C}/\Omega(t)$, and preserves the correspondence of infinity, i.e., $w(\infty;t) \equiv \infty$.

Theorem 1 (Riemann mapping theorem, [68], p.230)**.** *Given any simply connected open region R which is not the whole plane, and a point $z_0 \in R$, there exists a unique analytic function $f(z)$ in R, normalized by the conditions $f(z_0) = 0$, $f'(z_0) > 0$, such that $f(z)$ defines a one-to-one mapping of R onto the disk D.*

We need to extend $z = w(\zeta; t)$ to the boundary $\partial\Omega(t)$. To ensure that such extension exists, the boundary of the fluid domain must have certain nice properties. Though from biology, most microorganisms provide us "nice" boundaries to deal with, still we make it clear from mathematical sense: here we require that the boundary of the fluid domain $\partial\Omega$ satisfies the following condition [69]:

Condition 1. *For all $z \in \partial\Omega$ and any $\{z_n\} \subset \Omega$ that satisfies $\lim_{n\to\infty} z_n = z$, there always exists a curve*

$$\Gamma : \ [0, 1] \to \Omega \cup \{z\}$$

and a increasing sequence $\{t_n\} : \ 0 < t_1 < t_2 < \cdots < t_n < \cdots, \ t_n \to 1$, such that $\Gamma(t_n) = z_n \ (n = 1, 2, \cdots)$ and $\Gamma(t) \in \Omega \ (0 \le t < 1)$.

If $\partial\Omega$ satisfies Condition 1, then $z = w(\zeta; t)$ can be extended continuously to $\overline{\mathbb{C}}/D$, and w maps $\partial(\overline{\mathbb{C}}/D) = S^1$ to $\partial\Omega(t)$, as shown in Figure 5.1.

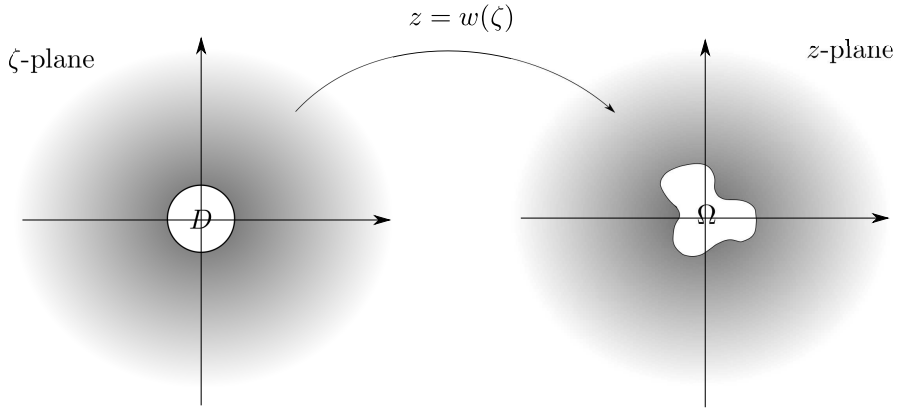

Figure 5.1: Conformal mapping from $\overline{\mathbb{C}}/D$ to $\overline{\mathbb{C}}/\Omega$.

Moreover, the conformal mapping $w(\zeta; t)$ has the property given in the following proposition.

Proposition 2. *Suppose that $\Omega(t)$ is a non-empty open bounded simply connected domain in $\mathbb{C}$, and that $z = w(\zeta; t)$ is the one-to-one and onto conformal mapping from the exterior of the unit disk D to the exterior of intΩ as we defined above. Then $w(\zeta; t)$ has a Laurent expansion of the form*

$$w(\zeta; t) = \alpha_1(t)\zeta + \alpha_0(t) + \frac{\alpha_{-1}(t)}{\zeta} + \frac{\alpha_{-2}(t)}{\zeta^2} + \cdots \frac{\alpha_{-n}(t)}{\zeta^n} + \cdots \tag{5.13}$$

where $\alpha_1(t) \neq 0$ *and* $|\zeta| > 1$.

This result is classic from complex analysis and in Section 5.5 we present a proof of it. Recall that we are considering in the body frame, hence $\Omega(t)$ which is determined by $w(\zeta;t)$ should be translation free and rotation free. We require $\alpha_0 = 0$ and $\alpha_{-1} \in \mathbb{R}$ in equation (5.13) so to fulfill these constraints [29, 31].

Though the Riemann mapping theorem theoretically ensures the existence of w, however, most of the time it is difficult to analytically find the corresponding conformal mapping of an arbitrary domain — even for some simple geometric domains — yet we could always numerically approximate it. The details of such numerical methods will be discussed in Chapter 8.

Assume that $w(\zeta;t)$ is the conformal mapping which maps $\overline{\mathbb{C}}/\overline{D}$ onto $\overline{\mathbb{C}}/\Omega(t)$ and $w(\infty;t) \equiv \infty$, then the boundary of the microorganism is given by $\partial\Omega(t) = \{z(t) = w(\sigma;t); \sigma \in S^1\}$. We suppose a no-slip boundary condition, and then the boundary condition is naturally given as

$$u\big(w(\sigma)\big)(t) = \frac{\partial}{\partial t} w(\sigma;t) \tag{5.14}$$

Suppose that $\phi(z;t)$ and $\psi(z;t)$ are the solutions to the boundary condition problem described by equation (5.12). Let

$$\Phi(\zeta;t) = \phi(w(\zeta;t);t), \qquad \Psi(\zeta) = \psi(w(\zeta;t);t) \qquad (|\zeta| \geq 1)$$

thus $\Phi(\zeta;t)$ and $\Psi(\zeta;t)$ are functions on ζ-plane which are analytic on $\mathbb{C}/\overline{D}$ and continuous on $\mathbb{C}/D$ at any time t. Hence on $|\zeta| \geqslant 1$, we have the Laurent expansion for Φ and Ψ as:

$$\Phi(\zeta;t) = A_0(t) + \frac{A_{-1}(t)}{\zeta} + \frac{A_{-2}(t)}{\zeta^2} + \cdots \tag{5.15}$$

$$\Psi(\zeta;t) = B_0(t) + \frac{B_{-1}(t)}{\zeta} + \frac{B_{-2}(t)}{\zeta^2} + \cdots \tag{5.16}$$

where A_k, B_k $(k = 0, -1, -2, \cdots)$ are continuous function from $[0, \infty]$ to $\mathbb{C}$.

If we substitute these expressions into equation (5.12) and omit the time index t, then the velocity field can be expressed as a function on the ζ-plane as

$$\widetilde{u}(\zeta, \overline{\zeta}) := u\big(w(\zeta), \overline{w(\zeta)}\big) = \Phi(\zeta) - \frac{w(\zeta)}{\overline{w'(\zeta)}} \overline{\Phi'(\zeta)} - \overline{\Psi(\zeta)} \tag{5.17}$$

where $'$ represents ∂_ζ. If we use $V(\sigma;t)$ to generally denote the boundary condition of the velocity, then the boundary condition problem stated previously can be generalized into the following equation:

$$\Phi(\sigma) - \frac{w(\sigma)}{\overline{w'(\sigma)}}\overline{\Phi'(\sigma)} - \overline{\Psi(\sigma)} = V(\sigma) \qquad (\sigma \in S^1). \tag{5.18}$$

In the swimming problem, the boundary condition is given as in equation (5.14), i.e., $V(\sigma;t) = \partial_t w(\sigma;t)$, however in the discussion below sometimes we will adopt a more general expression: $V(\sigma;t) = \sum_{n\neq 0} \lambda_n(t)\sigma^n$.

Hence the no-slip boundary condition problem can be generalized as follows: *Suppose that at time t, the microorganism occupies an simply connected compact domain $\Omega(t)$. $z = w(\zeta;t)$ is the conformal mapping which maps $\overline{\mathbb{C}}/\overline{D}$ to the fluid domain $\overline{\mathbb{C}}/\Omega(t)$ with $w(\infty;t) \equiv \infty$, and it can be extended continuously to $\overline{\mathbb{C}}/D$ so that the boundary of the microorganism/fluid at time t is given by $\partial\Omega(t) = \{w(\sigma;t); \sigma \in S^1\}$. Find $\Phi(\zeta;t)$ and $\Psi(\zeta;t)$ which are always single-valued and analytic on $\overline{\mathbb{C}}/\overline{D}$ and continuous on $\overline{\mathbb{C}}/D$, such that equation (*5.18*) holds for any t and the given velocity boundary condition $V(\zeta;t)$.*

5.3 Fredholm integral equation

The analysis of equation (5.18) can be found in [61]—though originally developed for the solution of problems in elasticity rather than the Stokes flows, the principle underlying are quite the same and in fact they end up with the same equation equation (5.18).

The analysis relies on the decomposition of the boundary condition $V(\sigma)$ derived from the following *Plemelj formula* [70, 71]:

Theorem 2 (Sokhotski, 1873, "Plemelj formula")**.** *Suppose $V(\sigma)$ is continuous on $S^1 = \{\sigma \in \mathbb{C}; |\sigma| = 1\}$ and, for a particular $\sigma_0 \in S^1$, satisfies the condition*

$$\big|V(\sigma) - V(\sigma_0)\big| \leq C\big|\sigma - \sigma_0\big|^\alpha, \qquad \sigma \in S^1 \tag{5.19}$$

for some positive constants C and α. Let

$$\widehat{V}(\zeta) = \frac{1}{2\pi i}\int_{S^1} \frac{V(\sigma)}{\sigma - \zeta} d\sigma \tag{5.20}$$

for $\zeta \in \mathbb{C}/S^1$. Then the limits

$$V^-(\sigma_0) := \lim_{r\to 1^-} \widehat{V}\big(r\sigma_0\big) \qquad \textit{and} \qquad V^+(\sigma_0) := \lim_{r\to 1^-} \widehat{V}(\sigma_0/r) \tag{5.21}$$

exist and moreover, $V^-(\sigma_0) - V^+(\sigma_0) = V(\sigma_0)$. Furthermore, the Cauchy principal-value integral

$$P.V. \int_{S^1} \frac{V(\sigma)}{\sigma - \sigma_0} d\sigma := \lim_{\varepsilon\to 0} \int_{|\sigma-\sigma_0|>\varepsilon} \frac{V(\sigma)}{\sigma - \sigma_0} d\sigma$$

exists and

$$V^+(\sigma_0) + V^-(\sigma_0) = \frac{1}{\pi i} P.V. \int_{S^1} \frac{V(\sigma)}{\sigma - \sigma_0} d\sigma$$

We assume that the boundary condition $V(\sigma)$ in the swimming problems satisfies the Hölder condition as in equation (5.19) for any $\sigma_0 \in S^1$. For the function $\widehat{V}(\zeta)$ defined in equation (5.20), let $V^+(\zeta) = \widehat{V}(\zeta)$ for $|\zeta| > 1$, and $V^-(\zeta) = \widehat{V}(\zeta)$ for $|\zeta| < 1$, then $V^-(\zeta)$ is analytic for $|\zeta| < 1$, while $V^+(\zeta)$ is analytic for $|\zeta| > 1$ with $V^+(\zeta) \to 0$ as $\zeta \to \infty$. Moreover, according to the Plemelj formula, both V^+ and V^- can be continuously extended to S^1 by equation (5.21), and we have the decomposition $V = V^- - V^+$ on S^1.

Before we continue, first we introduce a notation: for an analytic function $f(\zeta)$, we define $\overline{f}(\zeta)$ as $\overline{f}(\zeta) = \overline{f(\overline{\zeta})}$ [61]. With this notation, suppose that $f(\zeta)$ is analytic on $|\zeta| \geqslant R$ for some $R > 0$, then $\overline{f}(1/\zeta)$ is analytic on $|\zeta| \leqslant R$.

Proof. Without loss of generality, we assume that $f(\zeta)$ is analytic on $|\zeta| > R$, then on $|\zeta| > R$ we have the following Laurent expansion for $f(\zeta)$

$$f(\zeta) = f_0 + \frac{f_1}{\zeta} + \frac{f_2}{\zeta^2} + \cdots + \frac{f_n}{\zeta^n} + \cdots$$

Hence

$$f\big(\frac{1}{\zeta}\big) = f_0 + f_1\zeta + f_2\zeta^2 + \cdots + f_n\zeta^n + \cdots$$

which is easily seen to be analytic on $|\zeta| < R$. By definition of the function $\overline{f}$, we have

$$\overline{f}\big(\frac{1}{\zeta}\big) = \overline{f\big(\frac{1}{\overline{\zeta}}\big)} = \overline{f_0 + f_1\overline{\zeta} + f_2\overline{\zeta}^2 + \cdots + f_n\overline{\zeta}^n + \cdots} = \overline{f_0} + \overline{f_1}\zeta + \overline{f_2}\zeta^2 + \cdots + \overline{f_n}\zeta^n + \cdots$$

which is easily seen to be analytic on $|\zeta| < R$ as well. □

Now for $|\zeta| > 1$, apply the functional operator

$$\frac{1}{2\pi i}\int_{S^1} \frac{\bullet}{\sigma - \zeta} d\sigma$$

to both sides of equation (5.18). $\Phi(\zeta)$ is analytic on $|\zeta| > 1$, and continuous on $|\zeta| \geq 1$, so

$$\frac{1}{2\pi i}\int_{S^1} \frac{\Phi(\sigma)}{\sigma - \zeta} d\sigma = -\Phi(\zeta)$$

for $|\zeta| > 1$. Moreover, $\overline{\Psi}(1/\zeta)$ is analytic on $|\zeta| < 1$ and continuous on $|\zeta| \leq 1$, and thus

$$\frac{1}{2\pi i}\int_{S^1} \frac{\overline{\Psi(\sigma)}}{\sigma - \zeta} d\sigma = \frac{1}{2\pi i}\int_{S^1} \frac{\overline{\Psi}\big(1/\sigma\big)}{\sigma - \zeta} d\sigma = 0$$

On the other hand, for the right-hand side of equation (5.18) by Plemelj formula we have

$$\frac{1}{2\pi i}\int_{S^1} \frac{V(\sigma)}{\sigma - \zeta} d\sigma = V^+(\zeta)$$

Finally we get [61]:

$$\Phi(\zeta) + \frac{1}{2\pi i}\int_{S^1} \frac{w(\sigma)}{\overline{w'(\sigma)}} \frac{\overline{\Phi'(\sigma)}}{\sigma - \zeta} d\sigma = -V^+(\zeta) \qquad (|\zeta| \geq 1) \tag{5.22}$$

We refer to [61] for a combination of mathematical proof and physical explanation of the uniqueness and existence of the solution to equation (5.22). Knowing the solution Φ, equation (5.18) then yields Ψ immediately, and the whole problem is solved. Hence the uniqueness and existence of the solution to equation (5.22) ensures the uniqueness and existence of the solution to the boundary condition problem equation (5.18). Here "uniqueness" is in a sense that the constant terms A_0 and B_0 of Φ and Ψ as in equations (5.15,5.16) may vary yet the difference $A_0 - \overline{B_0}$ is uniquely determined. In fact $A_0 - \overline{B_0}$ gives the translation of the swimmer, as will be discussed in Section 5.4.

Generally speaking, equation (5.22) cannot be solved analytically except for some simple cases. Later in Chapter 6 we develop a way to approach it, which could help us understanding the swimming problem by providing a large variety of shape changes with a relatively low computational effort.

5.4 Physical Quantities

Before we end this Chapter, we would like to briefly discuss the physical quantities that people are relevant to a typical swimming problem. We scale the length by R and the time by T, where R usually corresponds to the radius of the cell when it is at a disk-shape, i.e., $\pi R^2 =$ Area of the cell.

At the end of this section, we present a list of these physical quantities in Table. 5.1 as a summary.

1. *Rigid motions (I): translation.*

   Following the approach set up in [29], let A^{rot} and A^{tr} be the rotational and translational components of the far field behavior, respectively. As stated in [29], A^{tr} is defined as the translation part of the velocity field at infinity:

   $$A^{\text{tr}} = \lim_{R\to\infty} \oint \frac{d\theta}{2\pi} u$$

   Also, it is shown in [29] that it can be expressed by the complex integral:

   $$A^{\text{tr}} = \lim_{R\to\infty} \frac{1}{2\pi i} \oint_{|z|=R} \frac{u(z,\overline{z})}{z} dz \tag{5.23}$$

   In general, we have

   Proposition 3.

   $$A^{tr} = a_0 - \overline{b_0} = A_0 - \overline{B_0} \tag{5.24}$$

   *where the a_0, b_0 are the leading order terms of ϕ and ψ as shown in equations (*5.10,5.11*), and A_0, B_0 are the leading order terms of Φ and Ψ as shown in equations (*5.15,5.16*).*

   Then the net translation of the swimmer at instant t should be

   $$Tr(t) = \int_0^t -A^{\text{tr}}(t)\ dt = \int_0^t \Big[-A_0(t) + \overline{B_0(t)} \Big]\ dt$$

   Naturally, the scale of Tr should be R. The mean velocity of the swimmer within a period should thus be $\overline{U} := Tr(T)/T$, scaled by R/T.

2. *Rigid motions (II): rotation.*

The rotation part A^{rot} is more complicated compared to A^{tr}. The strategy can be found in [29, 31]. The main idea is: the boundary condition is naturally given as $V(\sigma;t) = \partial_t w(\sigma;t)$, and it will result in a net torque denoted by $T(V;w)$, where the second variable w is to stress that the torque also relies on the shape of the microswimmer. We have to find a rotational flow with angular velocity A^{rot} which results in the same torque $T(V;w)$. In mathematical terms, let

$$V^{\text{rot}}(\sigma;t) = iw(\sigma;t)$$

then the boundary condition for the rotational flow is given by $A^{\text{rot}}(t)V^{\text{rot}}(\sigma;t)$, where A^{rot} satisfies

$$T\big(V - A^{\text{rot}}V^{\text{rot}};w\big) = T\big(\partial_t w - iA^{\text{rot}}w;w\big) \equiv 0$$

thus A^{rot} is given by

$$A^{\text{rot}} = \frac{T(V;w)}{T(V^{\text{rot}};w)} \tag{5.25}$$

It is difficult to find a general representation for A^{rot} similar to that for A^{tr}, however for the torque $T(V;w)$ we have [29, 31]

$$T(V;w) = 4\pi\mu \lim_{R\to\infty} \Im\Big[\frac{1}{2\pi i}\oint_{|z|=R} u(z,\overline{z})d\overline{z}\Big] = -4\pi\mu\Im b_{-1} \tag{5.26}$$

To determine $\Im b_{-1}$, from equation (5.11) it is easily seen that

$$b_{-1} = \frac{1}{2\pi i}\int_{\partial\Omega}\psi(z)dz$$

With $\partial\Omega = \{w(\sigma;t);\sigma\in S^1\}$, the above equation can be transformed into

$$b_{-1} = \frac{1}{2\pi i}\int_{S^1}\Psi(\sigma)w'(\sigma)d\sigma \tag{5.27}$$

Finally from equations (5.13,5.16,5.27) we have

$$b_{-1} = \frac{1}{2\pi i}\int_{S^1}\big(B_0 + \frac{B_{-1}}{\sigma} + \frac{B_{-2}}{\sigma^2} + \cdots\big)\big(\alpha_1 - \frac{\alpha_{-1}}{\sigma^2} - \frac{2\alpha_{-2}}{\sigma^3} - \cdots\big)d\sigma = B_{-1}\alpha_1$$

Equations (5.24, 5.26) first appear in [29] for the study of infinitesimal deformations of a circle, in which case these equations are trivial. Later they appear

in other literature for swimmers with more complicated geometry. It is true that these equations hold for general cases, yet they are not that obvious. In Section 5.5 we present a proof of these two equations.

3. *Force distribution.*

   From equation (5.3) and equation (5.7), we see that $fds = -2i\mu d(2\phi - V)$ on $\partial\Omega$. The pull-back of the force distribution is:

$$f(\sigma) = -2i\mu\big(2\Phi'(\sigma) - V'(\sigma)\big)\frac{d\sigma}{ds} = 2\mu\frac{\sigma\big(2\Phi'(\sigma) - V'(\sigma)\big)}{\big|w'(\sigma)\big|} \tag{5.28}$$

   It is easily seen that f is scaled by μ/T.

4. *Power expenditure.*

   The power expenditure is calculated by integrating the stress times the velocity on the surface of the swimmer[30, 62]:

$$\mathcal{P} = -\Re\oint_{\partial\Omega}\overline{u}f ds = -2\mu\Im\int_{S^1}\overline{V(\sigma)}\big(2\Phi'(\sigma) - V'(\sigma)\big)d\sigma$$

   With boundary condition generally given as $V(\sigma) = \sum_{n\neq 0}\lambda_n\sigma^n$, together with the expansion of $\Phi(\sigma)$ as given in equation (5.15), the integrand in the above equation can be expressed as

$$\overline{V(\sigma)}\big(2\Phi'(\sigma) - V'(\sigma)\big) = \Big(\sum_{m\neq 0}\overline{\lambda_{-m}}\sigma^m\Big)\Big(\sum_{n\geq 1}\frac{n\big(\lambda_{-n} - 2A_{-n}\big)}{\sigma^{n+1}} - \sum_{n\geq 1}n\lambda_n\sigma^{n-1}\Big)$$

   When we take the integral on S^1, only the σ^{-1} term does not vanish, and hence

$$\mathcal{P} = 4\pi\mu\sum_{n\geq 1}n\Big(\big|\lambda_n\big|^2 + 2A_{-n}\overline{\lambda_{-n}} - \big|\lambda_{-n}\big|^2\Big) \tag{5.29}$$

   Let $\overline{\mathcal{P}}$ be the average power expenditure within a period, i.e.,

$$\overline{\mathcal{P}} = \frac{1}{T}\int_0^T\mathcal{P}(t)dt \tag{5.30}$$

   also, we define the variance of the power as

$$Var(\mathcal{P}) := \frac{1}{T}\int_0^T[\mathcal{P}(t) - \overline{\mathcal{P}}]^2 dt \tag{5.31}$$

   which measures the fluctuation of $\mathcal{P}(t)$ within a period. $\mathcal{P}$ and $\overline{\mathcal{P}}$ are scaled by $\mu R^2/T^2$ and $Var(\mathcal{P})$ is scaled by $(\mu R^2/T^2)^2$.

5. *Efficiency.*

   For efficiency, we adopt the idea established by Lighthill [30] as in Chapter 2 and Chapter 3. Suppose that the average velocity and power are $\overline{U}$ and $\overline{\mathcal{P}}$, respectively. We define the efficiency to be

$$E = \frac{\overline{U}^2}{\overline{\mathcal{P}}} \tag{5.32}$$

   and E is scaled by $1/\mu$. This definition is a little different from equation 2.11 up to a constant. The reason why we do not follow equation 2.11 here is because that in Chapter 2 and Chapter 3 we are considering models consisting of spheres, in which case equation 2.11 is suitable. However in our 2D modeling we are considering more general shapes, hence a measure of power evaluated based on a spherical geometry might not be proper any more. But here E still measures the ratio of the power required for rigid translation with constant velocity $\overline{U}$ to the actual average power $\overline{\mathcal{P}}$. Also please be aware that E is scaled by $1/\mu$ while e by $1/R$ in equation 2.11.

6. *Area of the swimmer.*

   Finally I would like to say a few words about the incompressibility of the microswimmer. For cells swimming through a fluid by shape changes, to date there is no obvious evidence of material exchange between the cell and the surrounding fluid, hence we usually require mass conservation constraint for the swimming problem. In 2D it naturally becomes the area conservation constraint. Suppose that the shape changes of the microswimmer is given by equation (5.13), then the area of the microswimmer is [62]

$$\text{Area}(t) = \frac{1}{2}\Im \oint \overline{w} dw$$

   By a direct calculation we obtain

$$\text{Area}(t) = \pi\big(\big|\alpha_1\big|^2 - \big|\alpha_{-1}\big|^2 - 2\big|\alpha_{-2}\big|^2 - \cdots - n\big|\alpha_{-n}\big|^2 - \cdots\big) \tag{5.33}$$

   For incompressible swimmers, we require that $\text{Area}(t) \equiv \text{Constant}$. Area is naturally scaled by R^2.

Table 5.1: A list of physical quantities.

	Notation	Scale	Unit
Length		R	μm
Area		R^2	μm^2
Time	t	T	s
Mean velocity	$\overline{U}$	R/T	$\mu m/s$
Force density	f	μ/T	$pN/\mu m$
Mean power	$\overline{\mathcal{P}}$	$\mu R^2/T^2$	$pN \cdot \mu m/s$
Efficiency	E	$1/\mu$	$\mu m/(pN \cdot s)$
Variance of power	$Var(\mathcal{P})$	$(\mu R^2/T^2)^2$	$(pN \cdot \mu m/s)^2$

5.5 Appendix

5.5.1 Proof to Proposition 2

For simplicity we eliminate the notation of t. We start with a more general result:

Lemma 3. *[61][72] Ω, $\widetilde{\Omega}$ are open bounded simply connected domains in $\mathbb{C}$, $0 \in \Omega$, $\widetilde{\Omega}$ and $\infty \notin \Omega$, $\widetilde{\Omega}$. $z = w(\zeta)$ is a conformal mapping which maps $\mathbb{C}/\overline{\Omega}$ onto $\mathbb{C}/\overline{\widetilde{\Omega}}$, and $w(\infty) = \infty$, then the conformal mapping $z = w(\zeta)$ has the form*

$$w(\zeta) = \zeta \widetilde{w}(\zeta) \tag{5.34}$$

where both $\widetilde{w}(\zeta)$ and $1/\widetilde{w}(\zeta)$ are analytic functions on $\mathbb{C}/\overline{\Omega}$.

Or equivalently, under the assumption of Lemma 3, w has the form

$$w(\zeta) = C\zeta + w^*(\zeta) \tag{5.35}$$

where $C \neq 0$ is a constant, $w^*(\zeta)$ is analytic on $\mathbb{C}/\overline{\Omega}$.

Proof. First, let $\xi = 1/\zeta$, and consider the function

$$w_1(\xi) = \frac{1}{w(1/\xi)}$$

which, according to the assumption, maps $\Lambda = \{\xi \in \mathbb{C} : 1/\xi \in \mathbb{C}/\overline{\Omega}\}$ onto the domain $\widetilde{\Lambda} = \{w_1 \in \mathbb{C} : \exists \zeta \in \mathbb{C}/\overline{\Omega},\ s.t.\ w_1 = 1/w(\zeta)\}$. In particular, Λ, $\widetilde{\Lambda}$ are bounded domains

in $\mathbb{C}$ and $0 \in \Lambda$, $0 \in \widetilde{\Lambda}$. With $\xi = 0$ corresponding to $w_1 = 0$, the Laurent series of w_1 with respect to ξ at 0 has the form

$$w_1(\xi) = a_1\xi + a_2\xi^2 + \cdots + a_n\xi^n + \cdots \tag{5.36}$$

where $a_i \in \mathbb{C}$ and not all of a_i's equal 0. Now we have w_1 a conformal mapping from Λ to $\widetilde{\Lambda}$, which indicates that w_1 is univalent. Assume that $a_1 = \cdots = a_{N-1} = 0$, $a_N \neq 0$ for some $N \in \mathbb{Z}^+$, we only need to show that $N = 1$. Choose $\delta > 0$ so that equation (5.36) holds on $B(0;\delta) \subset \Lambda$. For $\xi \in \Lambda$, define

$$\varphi(\xi) = \begin{cases} \dfrac{w_1(\xi)}{\xi^N} & \xi \in \Lambda/\{0\} \\ a_N + a_{N+1}\xi + \cdots + a_{N+n}\xi^n + \cdots, & \xi \in B(0;\delta) \end{cases} \tag{5.37}$$

According to the discussion above, $\varphi(\xi)$ is well defined and analytic on Λ. w_1 is a conformal mapping and $w_1(0) = 0$, so $\xi = 0$ is the only zero of $w_1(\xi)$, hence the only possible zero of φ is $\xi = 0$. However, according to the definition of φ, obviously $\varphi(0) = a_N \neq 0$, so $0 \notin \varphi(\Lambda)$.

We may choose $\delta_1 \in (0, \delta)$, such that $B(0;\delta_1) \subset \Lambda$ and $\varphi(B(0;\delta_1))$ lies in some angular area $A_{(\theta_0,\theta_1)} = \{z \in \mathbb{C}; \theta_0 < \mathrm{Arg} z < \theta_0 + \theta_1\}$ where $0 < \theta_1 < 2\pi$, as is shown in Figure 5.2.

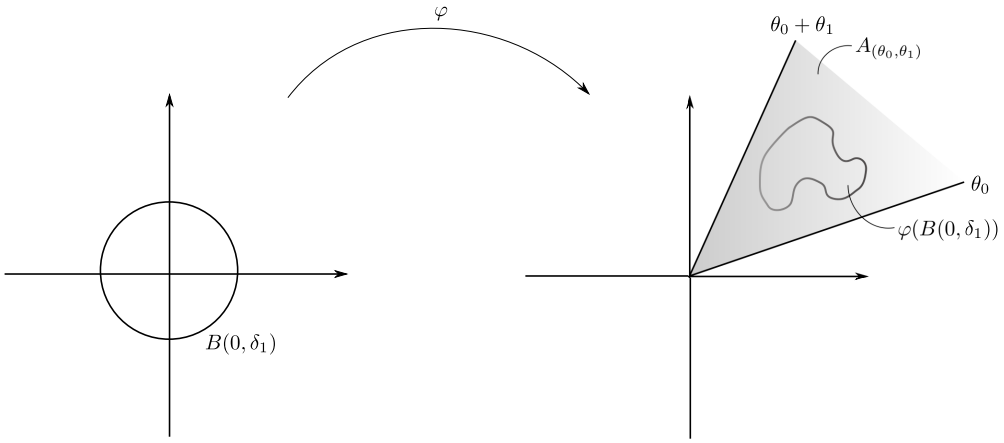

Figure 5.2: Proof of Lemma 3.

Define $\Phi(\xi) = \xi\varphi^{1/N}(\xi)$ for $\xi \in B(0;\delta_1)$. $0 \notin \varphi(B(0;\delta_1))$, so the function $z \mapsto z^{1/N}$ on $\varphi(B(0;\delta_1))$ is one-to-one and onto. In this case, it is easily seen that Φ is a conformal

mapping on $B(0;\delta_1)$ and $0 \in \Phi(B(0;\delta_1))$. If $N \geq 2$ the function $z \mapsto z^N$ is not univalent for any open neighborhood of 0, hence $w_1(\xi) = \Phi^N(\xi)$ is not univalent on $B(0;\delta_1)$, which is a contradiction to the assumption that w_1 is a conformal mapping on $\Lambda \supset B(0;\delta_1)$. This contradiction indicates that $N = 1$.

Now we have that on Λ, $w_1(\xi) = \xi\varphi(\xi)$. w_1 is a conformal mapping from Λ to $\widetilde{\Lambda}$, and $\infty \notin \Lambda$, $\infty \notin \widetilde{\Lambda}$, so w_1 is analytic. In this case, $\varphi(\xi) = w_1(\xi)/\xi$ is analytic on $\Lambda\backslash\{0\}$. On the other hand, by equation (5.37), $\varphi(0) = a_N \neq 0$ or ∞, so $\varphi(\xi)$ is analytic on Λ, and since $0 \notin \varphi(\Lambda)$, $1/\varphi(\xi)$ is also analytic on Λ.

Now we have

$$w(\zeta) = w(1/\xi) = \frac{1}{w_1(\xi)} = \frac{1}{\xi\varphi(\xi)} = \zeta\frac{1}{\varphi(1/\zeta)}$$

Let $\widetilde{w}(\zeta) = 1/[\varphi(1/\zeta)]$, then both $\widetilde{w}(\zeta)$ and $1/\widetilde{w}(\zeta)$ are analytic on $\mathbb{C}/\overline{\Omega}$.

□

With Lemma 3, Proposition 2 becomes obvious, as shown below:

Proof. According to Lemma 3, now we have a conformal mapping $z = w(\zeta)$ from $\mathbb{C}/\overline{D}$ onto $\mathbb{C}/\overline{\Omega}$ which has the form $w(\zeta) = \zeta\widetilde{w}(\zeta)$, where both $\widetilde{w}(\zeta)$ and $1/\widetilde{w}(\zeta)$ are analytic on $\mathbb{C}/\overline{D}$, then the Laurent expansion of $\widetilde{w}(\zeta)$ at ∞ should have the form

$$\widetilde{w}(\zeta) = \alpha_1 + \frac{\alpha_0}{\zeta} + \frac{\alpha_{-1}}{\zeta^2} + \frac{\alpha_{-2}}{\zeta^3} + \cdots$$

where $\alpha_1 \neq 0$ (otherwise $1/\widetilde{w}(\zeta)$ will not be analytic at ∞). Hence the Laurent expansion of $w(\zeta)$ at ∞ has the form

$$w(\zeta) = \alpha_1\zeta + \alpha_0 + \frac{\alpha_{-1}}{\zeta} + \frac{\alpha_{-2}}{\zeta^2} + \cdots \qquad (\alpha_1 \neq 0)$$

The above equation holds on some neighborhood $\{\zeta \in \mathbb{C}; |\zeta| > R\}$ of ∞. $w(\zeta)$ is analytic on $\mathbb{C}/\overline{D} = \{\zeta \in \mathbb{C}; |\zeta| > 1\}$, thus equation (5.13) holds on $\mathbb{C}/\overline{D}$, which completes the proof.

□

5.5.2 Proof of equation (5.24)

Proof. Choose $R > 0$ large enough so that ϕ, χ' are analytic on $|z| > R$, continuous up to $|z| \geq R$. Let $\xi = z/R$, by equations (5.3, 5.23),

$$A^{\mathrm{tr}} = \lim_{R\to\infty} \frac{1}{2\pi i} \oint_{|\xi|=1} \Big[\frac{\phi(R\xi)}{\xi} - R\overline{\phi'(R\xi)} - \overline{\frac{\chi'(R\xi)}{\xi}} \Big] d\xi \tag{5.38}$$

Let

$$\widetilde{\phi}(\xi) = \phi'(R\xi), \qquad \widetilde{\psi}(\xi) = \chi'(R\xi)$$

Obviously, $\widetilde{\phi}$, $\widetilde{\psi}$ are analytic on $|\xi| > 1$ (including infinity), continuous up to $|\xi| \geq 1$. Define

$$\overline{\widetilde{\phi}}(\xi) = \overline{\widetilde{\phi}(\bar{\xi})} \qquad \text{and} \overline{\widetilde{\psi}}(\xi) = \overline{\widetilde{\psi}(\bar{\xi})}$$

Then as functions of ξ, $\overline{\widetilde{\phi}}(1/\xi)$ and $\overline{\widetilde{\psi}}(1/\xi)$ are analytic on $|\xi| < 1$ and continuous up to $|\xi| \leq 1$, and on $|\xi| = 1$ we have:

$$\overline{\widetilde{\phi}}\big(\frac{1}{\xi}\big) = \overline{\widetilde{\phi}(\xi)}, \qquad \overline{\widetilde{\psi}}\big(\frac{1}{\xi}\big) = \overline{\widetilde{\psi}(\xi)}$$

Hence by Cauchy Integral Theorem,

$$\begin{aligned} \frac{1}{2\pi i} \oint_{|\xi|=1} \overline{\phi'(R\xi)} d\xi &= \frac{1}{2\pi i} \oint_{|\xi|=1} \overline{\widetilde{\phi}}\big(\frac{1}{\xi}\big) d\xi = 0 \\ \frac{1}{2\pi i} \oint_{|\xi|=1} \frac{\overline{\chi'(R\xi)}}{\xi} d\xi &= \frac{1}{2\pi i} \oint_{|\xi|=1} \frac{1}{\xi} \overline{\widetilde{\psi}}\big(\frac{1}{\xi}\big) d\xi = \overline{\widetilde{\psi}}\big(\frac{1}{\xi}\big)\Big|_{\xi=0} = \overline{\chi'(\infty)} = \overline{b_0} \end{aligned}$$

For the first term, by Residue Theorem,

$$\frac{1}{2\pi i} \oint_{|\xi|=1} \frac{\phi(R\xi)}{\xi} d\xi = a_0$$

Moreover, since the conformal mapping $z = w(\zeta)$ has the form equation (5.13), it is easily seen that $a_0 = A_0$ and $b_0 = B_0$. Hence we have proved equation (5.24).

□

5.5.3 Proof of equation (5.26)

Proof. The torque associated to the boundary condition $V(\sigma)$ is given by

$$T(V;w) = \lim_{R\to\infty} \Im \oint r \times f ds = \lim_{R\to\infty} \Im\Big[\int_{|z|=R} \overline{z} f ds\Big]$$

Observe equation (5.6), f is a sum of two parts: $4\mu(\Re\phi')n$ along the n direction and $-2\mu(z\overline{\phi''} + \overline{\chi''})\overline{n}$ along the $\overline{n}$ direction, where $n = -idz/ds$ is the exterior normal on $\partial\Omega$. This together with equation (5.7) indicate

$$\oint r \times \Big[4\mu\big(\Re\phi'\big)n\Big] ds = \int_{|z|=R} -2i\mu\overline{z}\big(\phi + \overline{\phi'}\big)dz = 0$$

and

$$\oint r \times f ds = -2i\mu \int_{|z|=R} \overline{z}\Big(z\overline{\phi''} + \overline{\chi''}\Big)d\overline{z}$$

hence

$$T(V;w) = -2\mu \lim_{R\to\infty} \Re \int_{|z|=R} \overline{z}\Big(z\overline{\phi''} + \overline{\chi''}\Big)d\overline{z}$$

On the other hand, from equation (5.3), we have

$$\frac{\partial u}{\partial \overline{z}} = -\big(z\overline{\phi''} + \overline{\chi''}\big)$$

so

$$\begin{aligned} T(V;w) &= 2\mu \lim_{R\to\infty} \Re \int_{|z|=R} \overline{z}\frac{\partial u}{\partial \overline{z}} d\overline{z} = 2\mu \lim_{R\to\infty} \Re\Big[- \int_{|z|=R} u d\overline{z}\Big] \\ &= 4\pi\mu \lim_{R\to\infty} \Im\Big[\frac{1}{2\pi i}\int_{|z|=R} u(z,\overline{z}) d\overline{z}\Big] \end{aligned}$$

Now we only need to calculate the complex integral in the above equation. Similar to that in the proof for A^{tr}, for R large enough, adopt the substitution $\xi = z/R$, by equation (5.3) we have

$$\frac{T(V;w)}{4\pi\mu} = \lim_{R\to\infty} \Im\Big[\frac{R}{2\pi i}\oint_{|\xi|=1} \Big(\phi(R\xi) - R\xi\overline{\phi'(R\xi)} - \overline{\chi'(R\xi)}\Big)d\overline{\xi}\Big]$$

On $|\xi| = 1$, we have $d\overline{\xi} = d\xi^{-1} = -\xi^{-2}d\xi$, so

$$\frac{T(V;w)}{4\pi\mu} = \lim_{R\to\infty} \Im\Big[- \frac{R}{2\pi i}\oint_{|\xi|=1} \Big(\frac{\phi(R\xi)}{\xi^2} - \frac{R}{\xi}\overline{\phi'(R\xi)} - \frac{1}{\xi^2}\overline{\chi'(R\xi)}\Big)d\xi\Big]$$

By the Residue Theorem

$$\frac{1}{2\pi i}\oint_{|\xi|=1}\frac{\phi(R\xi)}{\xi^2}d\xi = 0$$

By the Cauchy Integral Theorem

$$\frac{1}{2\pi i}\oint_{|\xi|=1}\frac{1}{\xi}\overline{\phi'(R\xi)}d\xi = \frac{1}{2\pi i}\oint_{|\xi|=1}\frac{1}{\xi}\overline{\tilde{\phi}}(\frac{1}{\xi})d\xi = \overline{\tilde{\phi}}(\frac{1}{\xi})\Big|_{\xi=0} = \overline{\phi'(\infty)} = 0$$

where $\overline{\phi'(\infty)} = 0$ because of the assumption to equation (5.10). Thus the first two terms vanish, as of the third term, also by Cauchy Integral Theorem,

$$\frac{1}{2\pi i}\oint_{|\xi|=1}\frac{1}{\xi^2}\overline{\chi'(R\xi)}d\xi = \frac{1}{2\pi i}\oint_{|\xi|=1}\frac{1}{\xi^2}\overline{\tilde{\psi}}(\frac{1}{\xi})d\xi = \frac{d}{d\xi}\Big[\overline{\tilde{\psi}}(\frac{1}{\xi})\Big]\Big|_{\xi=0} = \frac{d}{d\xi}\Big[\overline{\chi'(\frac{R}{\overline{\xi}})}\Big]\Big|_{\xi=0}$$

By equation (5.11), on $|\xi| \le 1$ we have

$$\overline{\chi'\Big(\frac{R}{\overline{\xi}}\Big)} = \frac{\overline{b_{-1}}}{R}\xi + \frac{\overline{b_{-2}}}{R^2}\xi^2 + \cdots + \frac{\overline{b_{-n}}}{R^n}\xi^n + \cdots$$

thus

$$\frac{d}{d\xi}\Big[\overline{\chi'(\frac{R}{\overline{\xi}})}\Big]\Big|_{\xi=0} = \frac{\overline{b_{-1}}}{R}$$

Finally we get

$$\frac{T(V;w)}{4\pi\mu} = \Im\Big[R\frac{\overline{b_{-1}}}{R}\Big] = -\Im b_{-1}$$

□

Chapter 6

Shapes of Conformal Mappings with Finitely Many Terms

As we mentioned earlier in Chapter 5, generally speaking the Fredholm integral equation (5.22) can not be solved analytically for an arbitrary conformal mapping $w(\zeta)$. However in the case that the conformal mapping $w(\zeta)$ has only finitely many terms, we find that equation (5.22) can be analytically simplified to a linear relation between the coefficients of Φ and V^+. Taking into account that any conformal mapping can be approximated by truncating its Laurent expansion, this method appears to be useful and reasonable in our study of 2D Stokes flow swimming problems.

This approach was first discussed by Muskhelishvili [61], and we follow his discussion.

6.1 Solving the Fredholm integral equation

As we explained in Section 5.2, generally the conformal mapping from $\mathbb{C}/D$ to the fluid domain $\mathbb{C}/\Omega$ for an arbitrary Ω should always have a Laurent expansion of the form given by equation (5.13). Here we consider a sequence of shape changes whose corresponding conformal mappings always have Laurent expansions up to $(-N)$-th order. In such case, we have

$$w(\zeta;t) = \alpha_1(t)\zeta + \alpha_0(t) + \frac{\alpha_{-1}(t)}{\zeta} + \frac{\alpha_{-2}(t)}{\zeta^2} + \cdots + \frac{\alpha_{-N}(t)}{\zeta^N} \tag{6.1}$$

Recall from Chapter 1 that we consider the problem in a body frame fixed to the swimmer. As discussed in Section 5.2 after Proposition 2, to ensure that the motions resulting from shape deformations prescribed by equation (6.1) are translation free and rotation free, we require that $\alpha_1 \in \mathbb{R}$ and $\alpha_0 \equiv 0$ — the former states that the shape changes are rotation free and the latter translation-free — so that $w(\zeta;t)$ corresponds to the intrinsic shape changes observed in the body frame.

The boundary condition is

$$V(\sigma;t) = \frac{\partial}{\partial t} w(\zeta;t) = \dot{\alpha}_1 \sigma + \frac{\dot{\alpha}_{-1}}{\sigma} + \frac{\dot{\alpha}_{-2}}{\sigma^2} + \cdots + \frac{\dot{\alpha}_{-N}}{\sigma^N} \tag{6.2}$$

However in the following discussion in this section, in order to obtain more general results, we assume $V(\sigma;t) = \sum \lambda_n(t)\sigma^n$ in general. Thus according to the Plemelj formula, the Laurent expansion of the corresponding $-V^+(\zeta;t)$ should be:

$$-V^+(\zeta;t) = \lambda_0(t) + \frac{\lambda_{-1}(t)}{\zeta} + \frac{\lambda_{-2}(t)}{\zeta^2} + \cdots + \frac{\lambda_{-n}(t)}{\zeta^n} + \cdots \qquad (\lambda_{-n}(t) \in \mathbb{C}) \tag{6.3}$$

First, we introduce the following general proposition, where the function $f_N(\zeta)$ is the analytic continuation of $\sigma^N w(\sigma)/\overline{w'(\sigma)}$ on S^1 to $|\zeta| < 1$:

Proposition 4. *Suppose that the conformal mapping $w(\zeta)$ is given by equation (6.1) and the boundary condition is given as $V(\sigma) = \sum \lambda_n \sigma^n$. If there exists a function $f_N(\zeta)$ analytic on $|\zeta| < 1$, continuous on $|\zeta| \leq 1$, and*

$$f_N(\sigma)\Big|_{\sigma \in S^1} = \sigma^N \frac{w(\sigma)}{\overline{w'(\sigma)}}$$

for some $N \in \mathbb{Z}^+$, $N \geq 2$, then for any $-V^+(\zeta)$ with Laurent series as in equation (6.3) such that $\lambda_{-1} = \lambda_{-2} = \cdots = \lambda_{-(N-2)} = 0$ ($N > 2$; in the $N = 2$ case, no restrictions for the coefficients), the solutions to the boundary value problem equation (5.18) are given by:

$$\begin{aligned} \Phi(\zeta) &= -V^+(\zeta) \\ \Psi(\zeta) &= \frac{\overline{w}(1/\zeta)}{w'(\zeta)} V^{+\prime}(\zeta) - \overline{V^-}(1/\zeta) \end{aligned}$$

for $|\zeta| \geq 1$.

In Proposition 4, the functions $\overline{w}$, $\overline{V^-}$ are defined in the following way: suppose that $f(\zeta)$ is any analytic function, then $\overline{f}$ is defined as $\overline{f}(\zeta) = \overline{f(\overline{\zeta})}$. Proposition 4 can be proved by direct calculation.

Proof. In this case, $-V^+$ has the representation

$$-V^+(\zeta) = \frac{\lambda_{-(N-1)}}{\zeta^{N-1}} + \frac{\lambda_{-N}}{\zeta^N} + \cdots + \frac{\lambda_{-n}}{\zeta^n} + \cdots$$

Take $\Phi(\zeta) = -V^+(\zeta)$. On S^1, we have

$$\overline{\Phi'(\sigma)} = -\sigma^N\big[(N-1)\overline{\lambda_{-(N-1)}} - N\overline{\lambda_{-N}}\sigma - \cdots - n\overline{\lambda_{-n}}\sigma^{n-N+1} - \cdots\big]$$

Now consider the integral term in equation (5.22):

$$\begin{aligned} & \frac{1}{2\pi i}\int_{S^1} \frac{w(\sigma)}{\overline{w'(\sigma)}}\frac{\overline{\Phi'(\sigma)}}{\sigma-\zeta}d\sigma \\ = & -\frac{1}{2\pi i}\int_{S^1} \frac{f_N(\sigma)}{\sigma-\zeta}\big[(N-1)\overline{\lambda_{-(N-1)}} - N\overline{\lambda_{-N}}\sigma - \cdots - n\overline{\lambda_{-n}}\sigma^{n-N+1} - \cdots\big]d\sigma \end{aligned}$$

Since $f_N(\zeta)[(N-1)\overline{\lambda_{-(N-1)}} - N\overline{\lambda_{-N}}\zeta - \cdots - n\overline{\lambda_{-n}}\zeta^{n-N+1} - \cdots]$ is analytic on $|\zeta| < 1$, continuous on $|\zeta| \le 1$, by Cauchy Integral Theorem, this integral term vanishes. Hence the left hand side of equation (5.22) reduces to $\Phi(\zeta) = -V^+(\zeta)$.

If we substitute this result into equation (5.18), and obtain the expression of Ψ as in the proposition.

□

With w given by equation (6.1) we have

$$\frac{w(\sigma)}{\overline{w'(\sigma)}} = \frac{\alpha_1\sigma + \alpha_0 + \alpha_{-1}\sigma^{-1} + \alpha_{-2}\sigma^{-2} + \cdots + \alpha_{-N}\sigma^{-N}}{\overline{\alpha_1} - \overline{\alpha_{-1}}\sigma^2 - 2\overline{\alpha_{-2}}\sigma^3 - \cdots - N\overline{\alpha_{-N}}\sigma^{N+1}}$$

hence naturally we may take

$$\begin{aligned} f_N(\zeta) &= \zeta^N\frac{\alpha_1\zeta + \alpha_0 + \alpha_{-1}\zeta^{-1} + \alpha_{-2}\zeta^{-2} + \cdots + \alpha_{-N}\zeta^{-N}}{\overline{\alpha_1} - \overline{\alpha_{-1}}\zeta^2 - 2\overline{\alpha_{-2}}\zeta^3 - N\overline{\alpha_{-N}}\zeta^{N+1}} \\ &= \frac{\alpha_{-N} + \alpha_{-(N-1)}\zeta + \cdots + \alpha_{-1}\zeta^{N-1} + \alpha_0\zeta^N + \alpha_1\zeta^{N+1}}{\overline{\alpha_1} - \overline{\alpha_{-1}}\zeta^2 - 2\overline{\alpha_{-2}}\zeta^3 - \cdots - N\overline{\alpha_{-N}}\zeta^{N+1}} \end{aligned} \tag{6.4}$$

If there is no singularity of f_N lies inside the unit disk $|\zeta| < 1$, then f_N is analytic on $|\zeta| < 1$ and we may apply Proposition 4 to obtain the solution of the boundary condition problem.

Now let us discuss a more general case. For any function $\Phi(\zeta)$ that is analytic on $|\zeta| > 1$, continuous on $|\zeta| = 1$, naturally its Laurent expansion has the form of equation (5.15). Let $\mathcal{S}$ be the set of all functions $\Phi(\zeta)$ whose coefficients of the Laurent expansion satisfy $\sum_{k\geq 1} k|A_{-k}| < +\infty$ and vanish at infinity. Namely,

$$\mathcal{S} = \Big\{\Phi(\zeta) = \frac{A_{-1}}{\zeta} + \frac{A_{-2}}{\zeta^2} + \frac{A_{-3}}{\zeta^3} + \cdots ; \sum_{k\geq 1} k|A_{-k}| < +\infty\Big\}$$

S is a Banach space endowed with the norm $\| \Phi \| = \sum_{k\geq 1} k|A_{-k}|$ [66].

Now with w given by equation (6.1), we define a conjugate linear operator $\mathbf{K}(w)$ on $\mathcal{S}$ as

$$\big[\mathbf{K}(w) \circ \Phi\big](\zeta) = \frac{1}{2\pi i} \int_{S^1} \frac{w(\sigma)}{\overline{w'(\sigma)}} \frac{\overline{\Phi'(\sigma)}}{\sigma - \zeta} d\sigma \tag{6.5}$$

Let $\mathcal{S}_0 = \{A_0 \in \mathbb{C}\}$, then $\mathbf{K}(w)$ can be extended to $\mathcal{S} \oplus \mathcal{S}_0$ such that $\mathbf{K}(w)|_{\mathcal{S}_0} \equiv 0$ in accordance with equation (6.5). Now for any $\Phi \in \mathcal{S} \oplus \mathcal{S}_0$, equation (5.22) can be written as

$$\big[\mathbf{I} + \mathbf{K}(w)\big]\Phi = -V^+$$

where $\mathbf{I}$ is the identity operator. For $n \in \mathbb{Z}^+$, let

$$\mathcal{S}_n^{\Re} = \big\{\frac{r}{\zeta^n}; r \in \mathbb{R}\big\} \qquad \text{and} \qquad \mathcal{S}_n^{\Im} = \big\{\frac{ir}{\zeta^n}; r \in \mathbb{R}\big\}$$

It is easily seen that $\mathcal{S}_n^{\Re}$'s and $\mathcal{S}_n^{\Im}$'s are real 1-dimensional linear subspaces of $\mathcal{S}$. With f_N given by equation (6.4), by Proposition 4, $\mathbf{K}(w)$ vanishes on each $\mathcal{S}_n^{\Re}$ and $\mathcal{S}_n^{\Im}$ for $n = N-1, N, N+1, \cdots$, and thus each $\mathcal{S}_n^{\Re}$ or $\mathcal{S}_n^{\Im}$ is invariant under the operator $\mathbf{I} + \mathbf{K}(w)$, i.e.,

$$\big[\mathbf{I} + \mathbf{K}(w)\big]\big|_{\mathcal{S}_n^{\Re}} = \mathbf{I}_{\mathcal{S}_n^{\Re}}; \qquad\qquad \big[\mathbf{I} + \mathbf{K}(w)\big]\big|_{\mathcal{S}_n^{\Im}} = \mathbf{I}_{\mathcal{S}_n^{\Im}}$$

Define

$$\mathcal{S}_N := \mathrm{Span}_{\mathbb{R}}\{\zeta^{-n}, i\zeta^{-n}\}_{n=-1}^{-(N-2)} = \bigoplus_{n=-1}^{-(N-2)} \big(\mathcal{S}_n^{\Re} \bigoplus \mathcal{S}_n^{\Im}\big)$$

which is a real $2(N-2)$-dimensional linear subspace of $\mathcal{S}$, and

$$\{\zeta^{-1}, \zeta^{-2}, \cdots, \zeta^{N-2}, i\zeta^{-1}, i\zeta^{-2}, \cdots, i\zeta^{N-2}\}$$

consists a basis of S_N. If f_N is analytic on $|\zeta| < 1$, then the action of $\mathbf{K}(w)$ on this basis can be expressed as:

$$\begin{aligned}
\big[\mathbf{K}(w)\big] \circ \zeta^{-n} &= -\frac{n}{2\pi i}\int_{\mathbb{T}} \frac{f_N(\sigma)}{\sigma-\zeta}\frac{1}{\sigma^{N-n-1}}d\sigma = \frac{n}{\zeta^{N-n-1}}\sum_{k=0}^{N-n-2}\frac{f_N^{(k)}(0)}{k!}\zeta^k \\
\big[\mathbf{K}(w)\big] \circ \big(i\zeta^{-n}\big) &= \frac{n}{2\pi}\int_{\mathbb{T}} \frac{f_N(\sigma)}{\sigma-\zeta}\frac{1}{\sigma^{N-n-1}}d\sigma = -\frac{in}{\zeta^{N-n-1}}\sum_{k=0}^{N-n-2}\frac{f_N^{(k)}(0)}{k!}\zeta^k
\end{aligned}$$

for $n = 1, 2, \cdots, N-2$. Notice that the sum in the above equations is simply the first $N-n-1$ terms of the Laurent expansion of $f_N(\zeta)$ at $\zeta = 0$. It is easily seen that on $\mathcal{S}_N$, the operator $\mathbf{K}(w)$ has a matrix representation as

$$\begin{aligned}
\big[\mathbf{K}(w)\big] \circ (\zeta^{-1}, \zeta^{-2}, \cdots, \zeta^{-(N-2)})^T &= K(w)\cdot(\zeta^{-1}, \zeta^{-2}, \cdots, \zeta^{-(N-2)})^T \\
\big[\mathbf{K}(w)\big] \circ (i\zeta^{-1}, i\zeta^{-2}, \cdots, i\zeta^{-(N-2)})^T &= -K(w)\cdot(i\zeta^{-1}, i\zeta^{-2}, \cdots, i\zeta^{-(N-2)})^T
\end{aligned}$$

where $K(w)$ is a $(N-2)\times(N-2)$ matrix with the form

$$K(w) = \begin{pmatrix}
\frac{f_N^{(N-3)}(0)}{(N-3)!} & \frac{f_N^{(N-4)}(0)}{(N-4)!} & \cdots & \cdots & \cdots & \frac{f_N''(0)}{2!} & \frac{f_N'(0)}{1!} & \frac{f_N(0)}{0!} \\
\frac{2f_N^{(N-4)}(0)}{(N-4)!} & \frac{2f_N^{(N-5)}(0)}{(N-5)!} & \cdots & \cdots & \cdots & \frac{2f_N'(0)}{1!} & \frac{2f_N(0)}{0!} & 0 \\
\frac{3f_N^{(N-5)}(0)}{(N-5)!} & \frac{3f_N^{(N-6)}(0)}{(N-6)!} & \cdots & \cdots & \cdots & \frac{3f_N(0)}{0!} & 0 & 0 \\
\vdots & \vdots & & & \cdot & 0 & 0 & \vdots \\
\vdots & \vdots & & \cdot & \cdot & \vdots & \vdots & \vdots \\
\vdots & \vdots & \cdot & \cdot & & \vdots & \vdots & \vdots \\
\frac{(N-3)f_N'(0)}{1!} & \frac{(N-3)f_N(0)}{0!} & 0 & \cdots & \cdots & 0 & 0 & 0 \\
\frac{(N-2)f_N(0)}{0!} & 0 & \cdots & \cdots & \cdots & 0 & 0 & 0
\end{pmatrix} \tag{6.6}$$

We conclude our results as:

Proposition 5. *Suppose that the conformal mapping $w(\zeta)$ is given by equation (6.1) and the boundary condition is given as $V(\sigma) = \sum \lambda_n \sigma^n$. If there exists a function $f_N(\zeta)$ analytic on $|\zeta| < 1$, continuous on $|\zeta| \le 1$, and*

$$f_N(\sigma)\Big|_{\sigma\in S^1} = \sigma^N \frac{w(\sigma)}{\overline{w'(\sigma)}}$$

for some $N \in \mathbb{Z}^+$, $N \ge 2$, then the integral equation equation (5.22) reduces to:

1. *For $n = 0$ or $n \geq N-1$, $A_{-n} = \lambda_{-n}$;*

2. *For $1 \leq n \leq N-2$:*

$$\begin{aligned}\big(I_{N-2} + K(w)\big)\big(\Re A_{-1}, \cdots, \Re A_{-(N-2)}\big)^T &= \big(\Re\lambda_{-1}, \cdots, \Re\lambda_{N-2}\big)^T \\ \big(I_{N-2} - K(w)\big)\big(\Im A_{-1}, \cdots, \Im A_{-(N-2)}\big)^T &= \big(\Im\lambda_{-1}, \cdots, \Im\lambda_{N-2}\big)^T\end{aligned}$$

where I_{N-2} is the $(N-2)$-identity matrix, and $K(w)$ is given by equation (6.6).

Here A_{-n} and λ_{-n} are coefficients of Φ and $-V^+$, respectively:

$$\begin{aligned}\Phi(\zeta) &= A_0 + \frac{A_{-1}}{\zeta} + \frac{A_{-2}}{\zeta^2} + \cdots + \frac{A_{-n}}{\zeta^n} + \cdots \\ -V^+(\zeta) &= \lambda_0 + \frac{\lambda_{-1}}{\zeta} + \frac{\lambda_{-2}}{\zeta^2} + \cdots + \frac{\lambda_{-n}}{\zeta^n} + \cdots\end{aligned}$$

Hence a typical algorithm for solving the Stokes equation of an infinite 2D Stokes flow when the shape deformations have finitely many terms in the conformal mapping $w(\zeta)$ is as follows:

1. With $w(\zeta)$ given by equation (6.1) and boundary condition given by equation (6.2), obtain

$$\Phi = (\mathbf{I} + \mathbf{K})^{-1} \circ (-V^+)$$

   by Proposition 5.

2. Obtain Ψ from equation (5.18):

$$\begin{aligned}\Psi(\zeta; t) &= -\frac{\dot\alpha_1}{\zeta} + \big(A_{-1} - \dot\alpha_{-1}\big)\zeta + \big(A_{-1} - \dot\alpha_{-2}\big)\zeta^2 + \cdots + \big(A_{-N} - \dot\alpha_{-N}\big)\zeta^N \\ &\quad \frac{\frac{\alpha_1}{\zeta} + \alpha_{-1}\zeta + \alpha_{-2}\zeta^2 + \cdots + \alpha_{-N}\zeta^N}{\alpha_1 - \frac{\alpha_{-1}}{\zeta^2} - \frac{2\alpha_{-2}}{\zeta^3} - \cdots - \frac{N\alpha_{-N}}{\zeta^{N+1}}}\Big(\frac{A_{-1}}{\zeta^2} + \frac{2A_{-2}}{\zeta^3} + \cdots + \frac{NA_{-N}}{\zeta^{N+1}}\Big) \quad (6.7)\end{aligned}$$

3. With Φ and Ψ fully solved, obtain the physical quantities according to Section 5.4.

6.2 An example

For $N = 0$, which is the circular case, we refer to [29] for a full detailed discussion, and [31] provides the $N = 1$, which corresponds to ellipses. In [62] Avron *et.al.* discussed

the $N = 2$ case. Observing Proposition 4, we may see that when $N \leq 2$ the problem becomes trivial in the sense that $\Phi \equiv -V^+$. In this section we show the analysis of the simplest non-trivial case, i.e., the $N = 3$ case, so as to illustrate the ideas and techniques introduced in Section 6.1.

In such case, the conformal mapping corresponding to the fluid domain at time t is given by:

$$z = w(\zeta; t) = \alpha_1(t)\zeta + \frac{\alpha_{-1}(t)}{\zeta} + \frac{\alpha_{-2}(t)}{\zeta^2} + \frac{\alpha_{-3}(t)}{\zeta^3} \tag{6.8}$$

where $\alpha_j \in \mathbb{C}$ for $j = 1, -1, -2, -3$. Notice that this is not a rotation free swimmer since we assume $\alpha_1 \in \mathbb{C}$ instead of $\alpha_1 \in \mathbb{R}$, however this does not effect our discussion below and we may obtain more general results.

The velocity boundary condition is

$$V(\sigma) = \dot{\alpha}_1(t)\sigma + \frac{\dot{\alpha}_{-1}(t)}{\sigma} + \frac{\dot{\alpha}_{-2}(t)}{\sigma^2} + \frac{\dot{\alpha}_{-3}(t)}{\sigma^3}$$

for $\sigma \in S^1$. Decompose $V(\sigma)$ by the Plemelj formula and we get

$$\begin{aligned} V^-(\zeta) &= \dot{\alpha}_1\zeta && (|\zeta| \leq 1) \\ -V^+(\zeta) &= \frac{\dot{\alpha}_{-1}}{\zeta} + \frac{\dot{\alpha}_{-2}}{\zeta^2} + \frac{\dot{\alpha}_{-3}}{\zeta^3} && (|\zeta| \geq 1) \end{aligned}$$

Take

$$f_3(\zeta) = \frac{\alpha_{-3} + \alpha_{-2}\zeta + \alpha_{-1}\zeta^2 + \alpha_1\zeta^4}{\overline{\alpha_1} - \overline{\alpha_{-1}}\zeta^2 - 2\overline{\alpha_{-2}}\zeta^3 - 3\overline{\alpha_{-3}}\zeta^4}$$

We require that

$$\big|\alpha_1\big| > \big|\alpha_{-1}\big| + 2\big|\alpha_{-2}\big| + 3\big|\alpha_{-3}\big| \tag{6.9}$$

which necessarily rules out the singularities of f_3 inside the unit disk. Hence $f_3(\zeta)$ is continuous on $|\zeta| \leq 1$.

The solution of the fluid velocity field is:

$$\begin{aligned} \Phi(\zeta) &= \frac{\lambda}{\zeta} + \frac{\dot{\alpha}_{-2}}{\zeta^2} + \frac{\dot{\alpha}_{-3}}{\zeta^3} \\ \Psi(\zeta) &= -\frac{\overline{\alpha_{-3}}}{\alpha_1}\lambda\zeta - \frac{\overline{\dot{\alpha}_1}}{\zeta} + \frac{\overline{\alpha_{-3}}\zeta + \overline{\alpha_{-2}} + \dfrac{\overline{\alpha_{-1}}}{\zeta} + \dfrac{\overline{\alpha_1}}{\zeta^3}}{\alpha_1 - \dfrac{\alpha_{-1}}{\zeta^2} - \dfrac{2\alpha_{-2}}{\zeta^3} - \dfrac{3\alpha_{-3}}{\zeta^4}}\Big(\lambda + \frac{2\dot{\alpha}_{-2}}{\zeta} + \frac{3\dot{\alpha}_{-3}}{\zeta^2}\Big) \end{aligned}$$

where $\lambda \in \mathbb{C}$ satisfying $\lambda + \alpha_{-3}\overline{\alpha_1^{-1}\lambda} = \dot{\alpha}_{-1}$. As $\zeta \to \infty$, it is easily seen that $\Phi(\zeta) \sim O(\zeta^{-1})$ and

$$\begin{aligned}\Psi(\zeta) &= -\frac{\overline{\alpha_{-3}}}{\alpha_1}\lambda\zeta + \frac{\overline{\alpha_{-3}}}{\alpha_1}\zeta\Big(\lambda + 2\frac{\dot{\alpha}_{-2}}{\zeta}\Big) + \frac{\overline{\alpha_{-2}}}{\alpha_1}\lambda + O(\frac{1}{\zeta}) \\ &= 2\frac{\overline{\alpha_{-3}}}{\alpha_1}\dot{\alpha}_{-2} + \frac{\overline{\alpha_{-2}}}{\alpha_1}\lambda + O(\frac{1}{\zeta})\end{aligned}$$

Hence by equation (5.24),

$$A^{\mathrm{tr}} = \Phi(\infty) - \overline{\Psi(\infty)} = -2\frac{\alpha_{-3}}{\overline{\alpha_1}}\overline{\dot{\alpha}_{-2}} - \frac{\alpha_{-2}}{\overline{\alpha_1}}\overline{\lambda}$$

A^{rot} is much more difficult to calculate. According to Section 5.4, we have

$$T(V; w) = -4\pi\mu\Im(B_{-1}\alpha_1)$$

To determine B_{-1}, notice that

$$\begin{aligned}\zeta\Psi(\zeta) &= -\frac{\overline{\alpha_{-3}}}{\alpha_1}\lambda\zeta^2 - \overline{\dot{\alpha}_1} + \frac{\overline{\alpha_{-3}}\zeta^2 + \overline{\alpha_{-2}}\zeta + \overline{\alpha_{-1}} + \dfrac{\overline{\alpha_1}}{\zeta^2}}{\alpha_1 - \dfrac{\alpha_{-1}}{\zeta^2} - \dfrac{2\alpha_{-2}}{\zeta^3} - \dfrac{3\alpha_{-3}}{\zeta^4}}\Big(\lambda + \frac{2\dot{\alpha}_{-2}}{\zeta} + \frac{3\dot{\alpha}_{-3}}{\zeta^2} \\ &= -\frac{\overline{\alpha_{-3}}}{\alpha_1}\lambda\zeta^2 - \overline{\dot{\alpha}_1} + \frac{1}{\alpha_1}\Big(\overline{\alpha_{-3}}\zeta^2 + \overline{\alpha_{-2}}\zeta + \overline{\alpha_{-1}} + \frac{\overline{\alpha_1}}{\zeta^2}\Big)\Big(\lambda + \frac{2\dot{\alpha}_{-2}}{\zeta} + \frac{3\dot{\alpha}_{-3}}{\zeta^2}\Big)\cdot \\ &\qquad \Big[1 + \Big(\frac{\alpha_{-1}}{\alpha_1\zeta^2} + \frac{2\alpha_{-2}}{\alpha_1\zeta^3} + \frac{3\alpha_{-3}}{\alpha_1\zeta^4}\Big) + \Big(\frac{\alpha_{-1}}{\alpha_1\zeta^2} + \frac{2\alpha_{-2}}{\alpha_1\zeta^3} + \frac{3\alpha_{-3}}{\alpha_1\zeta^4}\Big)^2 + \cdots\Big] \\ &= \frac{1}{\alpha_1}\Big[(\overline{\alpha_{-1}} + \frac{\overline{\alpha_{-3}}\alpha_{-1}}{\alpha_1})\lambda + 2\overline{\alpha_{-2}}\dot{\alpha}_{-2} + 3\overline{\alpha_{-3}}\dot{\alpha}_{-3} - \alpha_1\overline{\dot{\alpha}_1}\Big] + B_0\zeta + O(\frac{1}{\zeta})\end{aligned}$$

so

$$T(V; w) = -4\pi\mu\Im\Big[(\overline{\alpha_{-1}} + \frac{\overline{\alpha_{-3}}\alpha_{-1}}{\alpha_1})\lambda + 2\overline{\alpha_{-2}}\dot{\alpha}_{-2} + 3\overline{\alpha_{-3}}\dot{\alpha}_{-3} - \alpha_1\overline{\dot{\alpha}_1}\Big]$$

similarly we have

$$T(V^{\mathrm{rot}}; w) = -4\pi\mu\Re\Big[-i\big(\overline{\alpha_{-1}} + \frac{\overline{\alpha_{-3}}\alpha_{-1}}{\alpha_1}\big)\lambda^{\mathrm{rot}} + 2\overline{\alpha_{-2}}\alpha_{-2} + 3\overline{\alpha_{-3}}\alpha_{-3}\big) + \alpha_1\overline{\alpha_1}\Big]$$

where $\lambda^{\mathrm{rot}} \in \mathbb{C}$ satisfying $\lambda^{\mathrm{rot}} + \alpha_{-3}\overline{\alpha_1^{-1}\lambda^{\mathrm{rot}}} = i\alpha_{-1}$. Then according to Section 5.4, we may obtain A^{rot} by equation (5.25).

Finally for the power expenditure, we have

$$\mathcal{P} = 4\pi\mu\Big[\big|\dot{\alpha}_1\big|^2 + \big|\dot{\alpha}_{-1}\big|^2 + 2\big|\dot{\alpha}_{-2}\big|^2 + 3\big|\dot{\alpha}_{-3}\big|^2 - 2\Re\Big[\alpha_{-3}\overline{\alpha_1^{-1}\lambda\dot{\alpha}_{-1}}\Big]\Big]$$

Chapter 7

General Symmetric Shape Deformations

Low Reynolds number swimming is of interest not only to biologists and mathematicians, but also to those who study robotics. The former group studies observed shape deformations from experiments to understand the biophysics, while the latter are more interested in designing shape deformations so as to obtain optimal swimming, which helps them design aquatic mini-robots. In this Chapter, using the techniques that were introduced and developed in Chapter 5 and Chapter 6, we generate a large variety of symmetric shapes and study the resulting swimming behaviors in Stokes flows. The numerical experiments are described and discussed in Section 7.1. In Section 7.2, we analyze a simple example to illustrate and validate the results in Section 7.1. Finally in Section 7.3 and Section 7.4 we formulate the frameworks of two optimal problems based on our experimental designs in Section 7.1.

7.1 General symmetric shape deformations of an incompressible swimmer

Before we design our experiments we would like to introduce another constraint which will be used in this chapter only. Suppose that we have a sequence of shapes that can be described by a conformal mapping $w(\zeta;t)$, and we suppose that the Laurent expansion

of $w(\zeta;t)$ always has finitely many terms up to $(-N)$-th order, i.e., $w(\zeta;t)$ has the form of equation (6.1). As we discussed in Section 6.1, in order to apply Proposition 5 to the given shape deformations, we need f_N to be analytic on $|\zeta|<1$. From equation (6.4) one sees that if

$$|\alpha_{-1}|+2|\alpha_{-2}|+\cdots+N|\alpha_{-N}|<|\alpha_1| \tag{7.1}$$

then f_N is analytic on $|\zeta|<1$. Later in Chapter 8 we see that this condition is too strong, and when N is large, because of this strong condition, the prescribed shape deformations are restricted to be small. However in this chapter we will keep this condition, despite its disadvantage it still allows us obtain a lot of valuable analytical and computational results.

We consider periodic shape deformations that are mathematically prescribed by conformal mappings with the following form:

$$\begin{aligned} w(\zeta;t) &= C(t)\zeta+\frac{1}{M}\Big[\sin\Big(\frac{2\pi t}{T}\Big)\frac{a_1}{\zeta}+\sin\Big(\frac{2\pi t}{T}+\varphi\Big)\frac{a_2}{2\zeta^2}+\sin\Big(\frac{2\pi t}{T}+2\varphi\Big)\frac{a_3}{3\zeta^3}+\cdots \\ &\quad +\sin\Big(\frac{2\pi t}{T}+(N-1)\varphi\Big)\frac{a_N}{N\zeta^N}\Big] \end{aligned} \tag{7.2}$$

where we call φ the *phase difference*. M and $C(t)$ are chosen or calculated so to satisfy both equation (7.1) and the area conservation constraint as explained below. Moreover, at this point we consider symmetric shape deformations only, and hence we require that all the coefficients in equation (7.2) are real.

Comparing equation (7.2) with equation (6.1),we have

$$\alpha_1(t)=C(t),\qquad \alpha_{-k}(t)=\frac{a_k}{kM}\sin\big(\frac{2\pi t}{T}+(k-1)\varphi\big)\quad (k=1,2,\cdots,N)$$

We take $M=\sum_{k=1}^{N}|a_k|$, hence

$$\begin{aligned} &\big|\alpha_{-1}\big|+2\big|\alpha_{-2}\big|+\cdots+N\big|\alpha_{-N}\big| \\ =\;& \frac{1}{M}\Big(\big|a_1\sin(\frac{2\pi t}{T})\big|+\big|a_2\sin(\frac{2\pi t}{T}+\varphi)\big|+\cdots+\big|a_N\sin(\frac{2\pi t}{T}+(N-1)\varphi)\big|\Big) \\ <\;& \frac{1}{M}\Big(\big|a_1\big|+\big|a_2\big|+\cdots+\big|a_N\big|\Big)=1 \end{aligned} \tag{7.3}$$

On the other hand, we take

$$C(t)=\sqrt{1+\frac{1}{M^2}\Big(a_1^2\sin^2(\frac{2\pi t}{T})+\frac{1}{2}a_2^2\sin^2(\frac{2\pi t}{T}+\varphi)+\cdots+\frac{1}{N}a_N^2\sin^2(\frac{2\pi t}{T}+(N-1)\varphi)\Big)} \tag{7.4}$$

First, from equation (7.3) and equation (7.4) we have that

$$\big|\alpha_{-1}\big| + 2\big|\alpha_{-2}\big| + \cdots + N\big|\alpha_{-N}\big| < 1 < |\alpha_1| = C(t)$$

Hence equation (7.1) is satisfied. Next, from equation (5.33), the area of the microswimmer is

$$\text{Area}(t) = \pi\Big[C^2(t) - \frac{1}{M^2}\sum_{k=1}^{N}\frac{1}{k}a_k^2\sin^2\big(\frac{2\pi t}{T} + (k-1)\varphi\big)\Big] \equiv \pi$$

Hence equation (7.2) which prescribes our design is well-defined.

Our numerical experiments are designed as follows:

1. For each $N \geq 3$, we take $\varphi = \pi/2$ and test 200 randomly generated $\mathbf{a}_N \sim \mathcal{N}(0,5)^N$ (normal distribution with mean 0 and standard deviation 5), where $\mathbf{a}_N = (a_1, a_2, \cdots, a_N)$ is the coefficient vector in equation (7.2). For each randomly generated $\mathbf{a}_N$ we test its corresponding $Var(\mathcal{P}) \sim E$ relation, where $Var(\mathcal{P})$ and E are defined in equations (5.31, 5.32). The results for $3 \leq N \leq 10$ are shown in Figure 7.1 and Figure 7.2.

2. Next for each N we choose the most efficient $\mathbf{a}_N^e$ and one inefficient $\mathbf{a}_N^i$ obtained from the above experiments and let φ vary between 0 and 2π. We examine the relation of mean velocity $\overline{U}$, mean power $\overline{\mathcal{P}}$ and efficiency E to the phase difference φ . The results are shown in Figure 7.3 and Figure 7.4, also for $3 \leq N \leq 10$. In Table 7.1 we record the values of the coefficient vector $\mathbf{a}_N^e$ used in Figure 7.3, and in Table 7.2 the coefficient vector $\mathbf{a}_N^i$ used in Figure 7.4.

From these computational results, we observe that:

1. From Figure 7.1, we notice that there seems to be a contour that figures the upper boundary of the $Var(\mathcal{P}) \sim E$ distribution. This is especially clear in the $N = 3$ case. We generalize this behavior as:

$$\lim_{Var(\mathcal{P})\to\infty} \sup E = 0 \tag{7.5}$$

That is to say, as the power $\mathcal{P}(t)$ fluctuates more dramatically within a period, the highest efficiency that can be achieved by shape deformations prescribed by

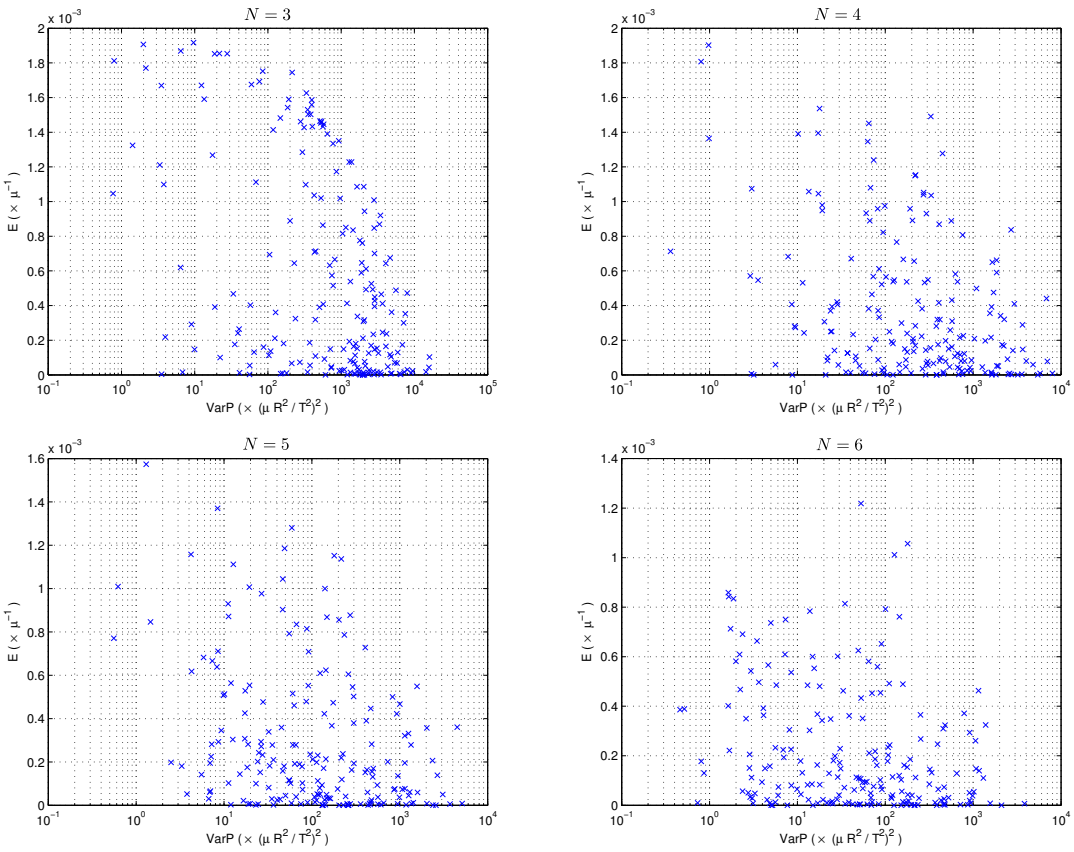

Figure 7.1: Relation between $Var(\mathcal{P})$ and E for $3 \leq N \leq 6$ with $\varphi = \pi/2$. In each panel we test 200 randomly generated $\mathbf{a}_N \sim \mathcal{N}(0,5)^N$.

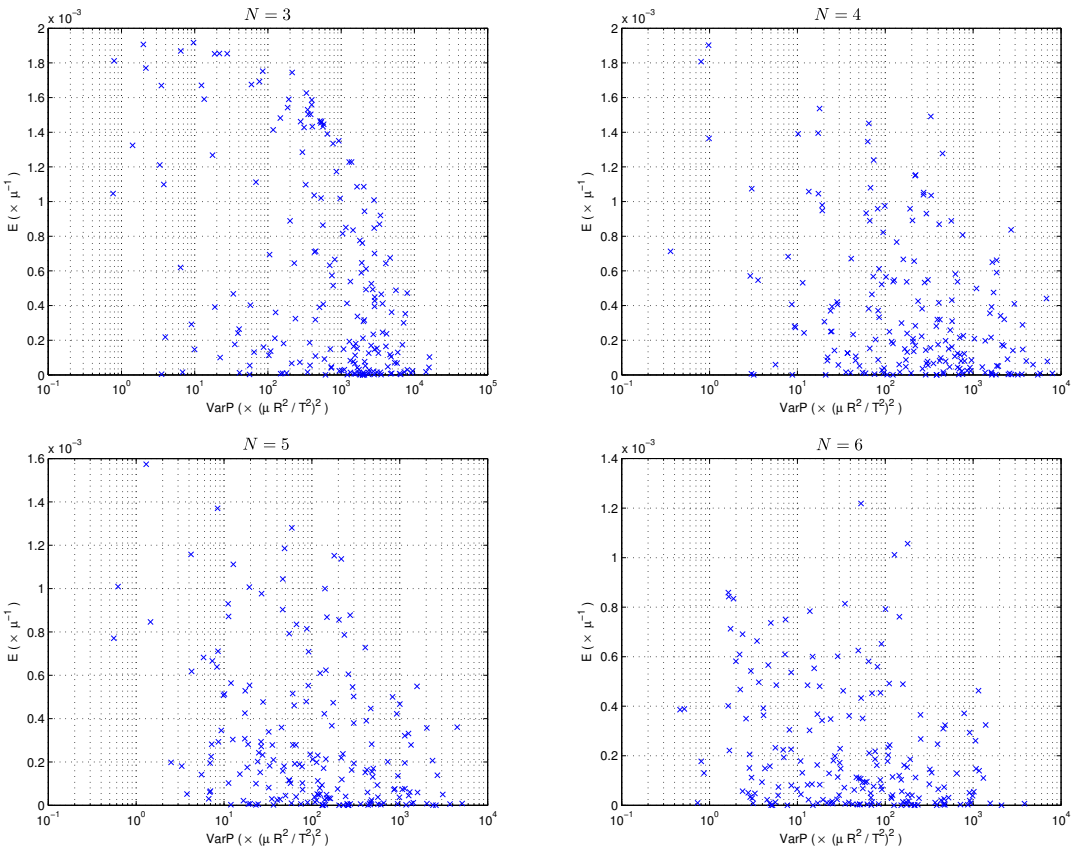

Figure 7.2: Relation between $Var(\mathcal{P})$ and E for $7 \leq N \leq 10$ with $\varphi = \pi/2$. In each panel we test 200 randomly generated $\mathbf{a}_N \sim \mathcal{N}(0,5)^N$.

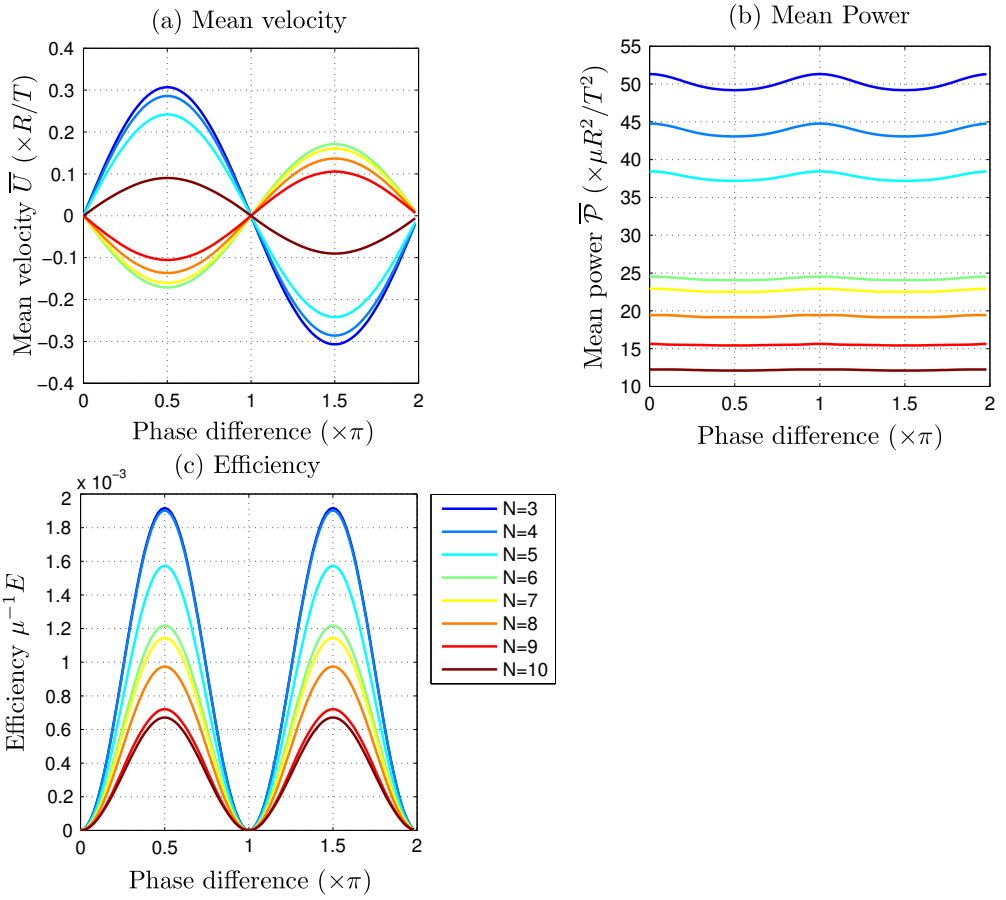

Figure 7.3: Effects of the phase difference φ on the efficient swimmers: (a) Mean velocity $\overline{U} \sim$ phase difference φ; (b) Mean power $\overline{\mathcal{P}} \sim$ phase difference φ; (c) Efficiency $E \sim$ phase difference φ.

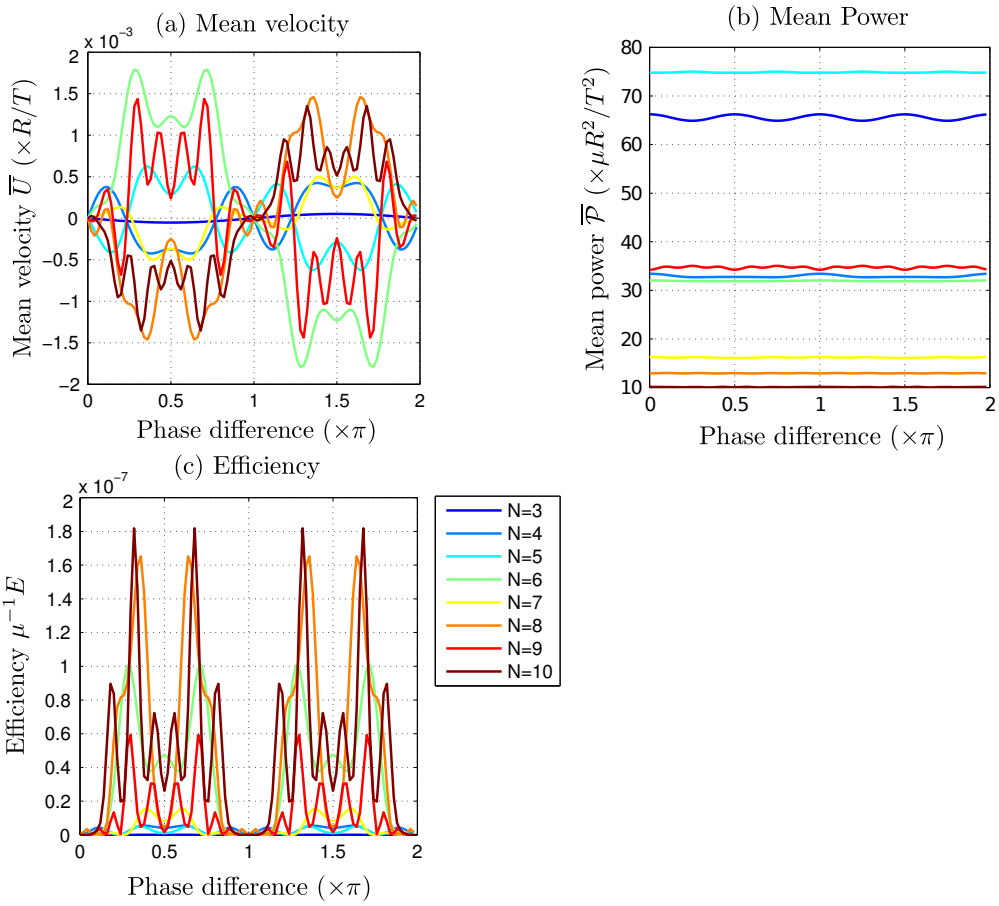

Figure 7.4: Effects of the phase difference φ on the inefficient swimmers: (a) Mean velocity $\overline{U} \sim$ phase difference φ; (b) Mean power $\overline{\mathcal{P}} \sim$ phase difference φ; (c) Efficiency $E \sim$ phase difference $\varphi \sim$.

Table 7.1: Coefficients $\mathbf{a}_N^e$ used in Figures. 7.3

	$\mathbf{a}_N^e$
$N = 3$	$(5.0934, 9.2930, 5.7184)$
$N = 4$	$(2.4410, 4.6241, 3.7978, 0.2649)$
$N = 5$	$(3.1385, 8.0197, 8.1800, -0.0111, -1.4334)$
$N = 6$	$(0.1628, -8.3208, 9.0443, -11.7976, 1.5308, -0.9356)$
$N = 7$	$(0.1628, -8.3208, 9.0443, -11.7976, 1.5308, -0.9356, 1.1064)$
$N = 8$	$(0.1628, -8.3208, 9.0443, -11.7976, 1.5308, -0.9356, 1.1064, -2.9718)$
$N = 9$	$(0.1628, -8.3208, 9.0443, -11.7976, 1.5308, -0.9356, 1.1064, -2.9718, -4.5435)$
$N = 10$	$(-1.3894, -0.8842, -0.3461, -6.0163, -7.4015, -2.9306, -1.0783, -1.3936, -0.2542, 0.6914)$

Table 7.2: Coefficients $\mathbf{a}_N^i$ used in Figures. 7.4

	$\mathbf{a}_N^i$
$N = 3$	$(-0.8869, 0.0002, -3.2860)$
$N = 4$	$(3.6270, -4.3786, -3.2841, -3.8885)$
$N = 5$	$(-5.7398, -0.1223, -3.0843, 0.3901, -2.0733)$
$N = 6$	$(1.7509, -12.4844, -2.0945, -1.6267, 1.5415, 7.9863)$
$N = 7$	$(-3.0016, -3.4558, 2.1998, 3.4503, -5.1842, 1.0265, -1.5188)$
$N = 8$	$(-5.3444, -4.7398, 3.0007, -6.8076, 1.3890, -8.3127, 0.0317, -8.6945)$
$N = 9$	$(-5.7398, -0.1223, -3.0843, 0.3901, -2.0733, -0.5829, -0.3772, 0.3797, -4.2718)$
$N = 10$	$(-5.5882, 4.7035, 2.5986, 3.6379, 1.4710, 1.2260, -0.7697, 7.5406, 11.2303, -3.1129)$

equation 7.2 decreases. This result indicates that in order to obtain relatively efficient swimming behavior, the swimmer should avoid dramatic fluctuation of the power expenditure.

At this point we do not have an explanation or proof to equation (7.5). Moreover, the conditions to the numerical experiments from which we obtain equation (7.5) are very limited: first we restrict shape deformations to the form of equation (7.2) only, next the coefficient vectors $\mathbf{a}_N$ are generated from $\mathcal{N}(0, 5)^N$. We do not know if relaxing these conditions will have any effect on equation (7.5). However

we did test shape deformations prescribed by the following equation:

$$\begin{aligned} w(\zeta;t) &= C(t)\zeta + \frac{1}{M}\Big[\sin\Big(\frac{2\pi t}{T}\Big)\frac{a_1}{\zeta} + \sin\Big(\frac{2\pi t}{T}+\varphi_1\Big)\frac{a_2}{2\zeta^2} + \sin\Big(\frac{2\pi t}{T}+\varphi_2\Big)\frac{a_3}{3\zeta^3} + \cdots \\ &\quad + \sin\Big(\frac{2\pi t}{T}+\varphi_{N-1}\Big)\frac{a_N}{N\zeta^N}\Big] \end{aligned}$$

that is, shape deformations with more general phase differences, and the numerical results show that equation (7.5) still holds.

2. From Figure 7.3 and Figure 7.4 we see that for fixed $\mathbf{a}_N$, functions $\overline{U}_{\mathbf{a}_N}(\varphi)$, $\overline{\mathcal{P}}_{\mathbf{a}_N}(\varphi)$ and $E_{\mathbf{a}_N}(\varphi)$ are all periodic functions with period 2π. Within $[0, 2\pi]$, $\overline{\mathcal{P}}_{\mathbf{a}_N}(\varphi)$ and $E_{\mathbf{a}_N}(\varphi)$ are symmetric with respect to the line $\varphi = \pi$, while $\overline{U}_{\mathbf{a}_N}(\varphi)$ is symmetric with respect to the point $(\pi, 0)$. This is not surprising and could be predicted from physics, since replacing φ by $-\varphi$ simply leads to the same swimming process but in the opposite direction.

3. From Figure 7.3 (a) and (c) we see that for those efficient swimmers, $\overline{U}_{\mathbf{a}_N}(\varphi)$ and $E_{\mathbf{a}_N}(\varphi)$ exhibit nice sinusoidal behavior. And we have an estimate of them:

$$\overline{U}_{\mathbf{a}_N}(\varphi) = A(\mathbf{a}_N)\sin\varphi \tag{7.6}$$

$$E_{\mathbf{a}_N}(\varphi) = B(\mathbf{a}_N)\big(1-\cos 2\varphi\big) \tag{7.7}$$

where $A(\mathbf{a}_N)$ and $B(\mathbf{a}_N)$ are constants depend on $\mathbf{a}$ only. Hence $\max_{\varphi\in[0,2\pi]}|\overline{U}_{\mathbf{a}_N}(\varphi)|$ and $\max_{\varphi\in[0,2\pi]}|E_{\mathbf{a}_N}(\varphi)|$ can be obtained at around $\varphi = \pi/2$ or $\varphi = 3\pi/2$. Equations (7.6, 7.6) provide us possible necessary conditions that an optimal swimmer should possess. Also from Figure 7.3 (b) we see that the power does not fluctuate much with respect to phase difference for those efficient swimmers. Finally as a remark, people may argue that from Figure 7.3 (a) (c) that both the mean velocity and the efficiency decreases as N increases. However keep in mind that we require an additional mathematical constraint given by equation (7.1), which necessarily limits the amplitude of shape deformations for higher order of N. Hence we can not make any conclusion related to N.

   For inefficient swimmers, things are more complicated as can be seen from Figure 7.4 and we do not have a definite conclusion at this point. It is true that the power does not fluctuate much as well, as can be seen from Figure 7.4 (b), however

if we observe Figure 7.1 we may see that there are a large variety of inefficient swimmers ranging from small $Var(\mathcal{P})$ to very large $Var(\mathcal{P})$, hence here we would not make any conclusion about the power behavior for inefficient swimmers.

7.2 Analysis of a simple example

In this section we analyze a simple example so as to illustrate and validate the conclusions in Section 7.1. We consider a compressible cell whose shape deformations are given by

$$w(\zeta;t) = C\zeta + \frac{a_{N-1}(t)}{(N-1)\zeta^{N-1}} + \frac{a_N(t)}{N\zeta^N} \tag{7.8}$$

where $N \geq 2$ and C is a constant. The swimmer has only two degrees of freedom, determined by modes $\zeta^{-(N-1)}$ and ζ^{-N}. $a_{N-1}(t)$ and $a_N(t)$ are both periodic functions with period T, and we assume that $\forall\ t \in [0,T]$, the following inequality (which comes from equation (7.1)) holds:

$$|a_{N-1}(t)| + |a_N(t)| < |C|$$

With the shape deformations given by equation (7.8), the boundary velocity is given by

$$V(\sigma;t) = \frac{\dot{a}_{N-1}(t)}{(N-1)\zeta^{N-1}} + \frac{\dot{a}_N(t)}{N\zeta^N} \tag{7.9}$$

The Plemelj decomposition of V is:

$$\begin{aligned} V^-(\zeta;t) &= 0 \\ -V^+(\zeta;t) &= \frac{\dot{a}_{N-1}(t)}{(N-1)\zeta^{N-1}} + \frac{\dot{a}_N(t)}{N\zeta^N} \end{aligned}$$

It is easy to calculate the function f_N in Proposition 5 and we find that:

$$f_N(\zeta;t) = \frac{\frac{a_N}{N} + \frac{a_{N-1}}{N-1}\sigma + C\sigma^{N+1}}{C - a_{N-1}\sigma^N - a_N\sigma^{N+1}}$$

According to Section 6.1, the Goursat functions are:

$$\begin{aligned} \Phi(\zeta;t) &= -V^+(\zeta;t) = \frac{\dot{a}_{N-1}(t)}{(N-1)\zeta^{N-1}} + \frac{\dot{a}_N(t)}{N\zeta^N} \\ \Psi(\zeta;t) &= \frac{\frac{C}{\zeta} + \frac{a_{N-1}(t)}{N-1}\zeta^{N-1} + \frac{a_N(t)}{N}\zeta^N}{C - \frac{a_{N-1}(t)}{\zeta^N} - \frac{a_N(t)}{\zeta^{N+1}}}\Big[\frac{\dot{a}_{N-1}(t)}{\zeta^N} + \frac{\dot{a}_N(t)}{\zeta^{N+1}}\Big] \end{aligned}$$

Moreover, we have explicit expressions for the following quantities.

1. *Translation*: The translation is the time integral of the conjugate of the leading term of Ψ:

$$Tr(t) = \frac{1}{CN}\int_0^t a_N(t)\dot{a}_{N-1}(t)\ dt$$

and hence the mean velocity within one period should be

$$\overline{U} = \frac{Tr(T)}{T} = \frac{1}{CNT}\int_0^T a_N(t)\dot{a}_{N-1}(t)\ dt$$

2. *Force distribution*:

$$f(\sigma) = -\frac{2\mu}{|w'(\sigma)|}\Big[\frac{\dot{a}_{N-1}(t)}{\sigma^{N-1}} + \frac{\dot{a}_N(t)}{\sigma^N}\Big]$$

where

$$\big|w'(\sigma)\big|^2 \quad = \quad C^2 + a_{N-1}^2 + a_N^2 + 2a_{N-1}a_N\Re\sigma - 2C\Big(a_{N-1}\Re\sigma^N + a_N\Re\sigma^{N+1}\Big)$$

3. *Power expenditure*:

$$\mathcal{P}(t) = 4\pi\mu\Big[\frac{\dot{a}_{N-1}^2}{N-1} + \frac{\dot{a}_N^2}{N}\Big]$$

Without loss of generality, we may take $C \equiv 1$. Now let us consider the energy optimization and performance optimization problems. First for the energy optimization in which we want to maximize E, according to [62], we need to solve the Euler-Lagrange equations with respect to the Lagrangian $\mathcal{L} = \mathcal{L}[a_{N-1}, a_N, \dot{a}_{N-1}, \dot{a}_N]$:

$$\mathcal{L}[a_{N-1}, a_N, \dot{a}_{N-1}, \dot{a}_N] = 4\pi\mu\Big[\frac{\dot{a}_{N-1}^2}{N-1} + \frac{\dot{a}_N^2}{N}\Big] + \frac{\lambda}{N}a_N\dot{a}_{N-1} \tag{7.10}$$

where λ is a Lagrange multiplier, together with the constraint

$$\max_{t\in[0,T]}\Big(\big|a_{N-1}(t)\big| + \big|a_N(t)\big|\Big) \le 1 \tag{7.11}$$

The Euler-Lagrange equations reduce to

$$\begin{cases} 8\pi\mu\dfrac{\ddot{a}_{N-1}}{N-1} + \dfrac{\lambda}{N}\dot{a}_N = 0 \\ 8\pi\mu\dfrac{\ddot{a}_N}{N} - \dfrac{\lambda}{N}\dot{a}_{N-1} = 0 \end{cases}$$

If we require the initial condition to be $a_{N-1}(0) = 0$, then the solutions are given by

$$\begin{cases} a_{N-1}(t) = M\sqrt{N-1}\sin\dfrac{2k\pi t}{T} \\ a_N(t) = M\sqrt{N}\cos\dfrac{2k\pi t}{T} \\ \lambda = -\dfrac{16k\pi^2\mu}{T}\sqrt{\dfrac{N}{N-1}} \end{cases} \qquad (k = 0, \pm1, \pm2, \cdots) \tag{7.12}$$

where M is a constant. Taking into account of equation (7.11), we may take $M = \sqrt{N-1} + \sqrt{N}$. If we take $k = 1$, then we have that for fixed N,

$$\max E = E\big(\frac{|a_{N-1}|}{|a_N|} = \frac{\sqrt{N-1}}{\sqrt{N}}, \varphi = \pm\frac{\pi}{2}\big) = \frac{N-1}{16\pi\mu N}\frac{1}{(\sqrt{N}+\sqrt{N-1})^2} \tag{7.13}$$

and correspondingly,

$$\begin{aligned} \overline{\mathcal{P}} &= \frac{16\pi^3\mu}{T^2}\frac{1}{(\sqrt{N}+\sqrt{N-1})^2} \\ \overline{U} &= \frac{\pi}{NT}\frac{\sqrt{N(N-1)}}{(\sqrt{N}+\sqrt{N-1})^2} \\ \mathcal{P}(t) &\equiv \overline{\mathcal{P}} \\ Var(\mathcal{P}) &\equiv 0 \\ \text{Area}(t) &\equiv \pi\Big[1 - \frac{1}{(\sqrt{N-1}+\sqrt{N})^2}\Big] \end{aligned}$$

Especially notice that in such case:

1. the area does not vary, which means that in this case the swimmer is actually an incompressible swimmer;

2. the power does not vary, which means that it requires constant energy expenditure.

As for the performance optimization in which we are to maximize $\overline{U}$, Euler-Lagrange equations result in minimization instead of maximization. Hence we approach it by Fourier series instead. We suppose that

$$a_{N-1}(t) \sim \frac{a^0_{N-1}}{2} + \sum_{k=1}^{\infty}\Big[a^k_{N-1}\cos\frac{2k\pi t}{T} + \widetilde{a}^k_{N-1}\sin\frac{2k\pi t}{T}\Big] \tag{7.14}$$

$$a_N(t) \sim \frac{a^0_N}{2} + \sum_{k=1}^{\infty}\Big[a^k_N\cos\frac{2k\pi t}{T} + \widetilde{a}^k_N\sin\frac{2k\pi t}{T}\Big] \tag{7.15}$$

Then the performance optimization problem reduces to

$$\text{maximize} \quad \overline{U} = \frac{\pi}{NT}\sum_k k\Big(a_{N-1}^k \widetilde{a}_N^k - a_N^k \widetilde{a}_{N-1}^k\Big)$$

subject to the constraint equation (7.11). There is no definite maximal solution to this problem, however if we only allow the first K modes in the Fourier expansions of $a_{N-1}(t)$ and $a_N(t)$ in equations (7.14,7.15), then the kinematic optimized solutions are given by:

$$a_{N-1}(t) = \widetilde{a}_{N-1}^K \sin\frac{2K\pi t}{T}, \qquad a_N(t) = a_N^K \cos\frac{2K\pi t}{T} \tag{7.16}$$

where $|\widetilde{a}_{N-1}^K| = |a_N^K|$.

In particular, if we take $K = 1$, then for fixed N,

$$\max \overline{U} = \overline{U}\big(|a_{N-1}| = |a_N|, \varphi = \pm\frac{\pi}{2}\big) = \pm\frac{\pi}{4NT} \tag{7.17}$$

Correspondingly,

$$\begin{aligned}
\overline{\mathcal{P}} &= \frac{2\pi^3\mu}{T^2}\Big(\frac{1}{N-1} + \frac{1}{N}\Big) \\
E &= \frac{N-1}{32\pi\mu N(2N-1)} \\
\mathcal{P}(t) &= \overline{\mathcal{P}} + \frac{2\pi^3\mu}{(N-1)NT^2}\cos\frac{4\pi t}{T} \\
Var(\mathcal{P}) &= \frac{2\pi^6\mu^2}{(N-1)^2N^2T^4} \\
\text{Area}(t) &= \pi\Big[1 - \frac{\sin^2\left(\frac{2\pi t}{T}\right)}{4(N-1)} - \frac{\cos^2\left(\frac{2\pi t}{T}\right)}{4N}\Big]
\end{aligned}$$

This is a compressible swimmer, and we have the following estimate for the variation of the area:

$$\Delta\text{Area} \le \frac{\pi}{N(N-1)}$$

Below for $N = 3$ and $N = 10$, we show the energy and performance optimized shape deformations within one period and their translation $Tr(t)$ and power $\mathcal{P}(t)$ within five periods.

1. $N = 3$. The performance optimized sequence of shape deformation is given by

$$w(\zeta;t) = \zeta + \frac{1}{4\zeta^2}\sin\frac{2\pi t}{T} + \frac{1}{6\zeta^3}\cos\big(\frac{2\pi t}{T}\big) \tag{7.18}$$

and $\overline{U}$, $\overline{\mathcal{P}}$ and E are:

$$\begin{aligned}
\overline{U} &= \frac{\pi R}{12T} \approx 0.2618\frac{R}{T} \\
\overline{\mathcal{P}} &= \frac{5\pi^3\mu R^2}{3T^2} \approx 51.6771\frac{\mu R^2}{T^2} \\
E &= \frac{1}{240\pi\mu} \approx 1.3263\times 10^{-3}\frac{1}{\mu}
\end{aligned}$$

The energy optimized sequence of shape deformation is given by

$$w(\zeta;t) = \zeta + \frac{1}{\sqrt{2}+\sqrt{3}}\Big[\frac{1}{\sqrt{2}\zeta^2}\sin\big(\frac{2\pi t}{T}\big) + \frac{1}{\sqrt{3}\zeta^3}\cos\big(\frac{2\pi t}{T}\big)\Big] \tag{7.19}$$

and $\overline{U}$, $\overline{\mathcal{P}}$ and E are:

$$\begin{aligned}
\overline{U} &= \frac{\sqrt{6}\pi R}{3(5+2\sqrt{6})T} \approx 0.2591\frac{R}{T} \\
\overline{\mathcal{P}} &= \frac{16\pi^3\mu R^2}{(5+2\sqrt{6})T^2} \approx 50.1163\frac{\mu R^2}{T^2} \\
E &= \frac{1}{24(5+2\sqrt{6})\pi\mu} \approx 1.3398\times 10^{-3}\frac{1}{\mu}
\end{aligned}$$

2. $N = 10$. The performance optimized sequence of shape deformation is given by

$$w(\zeta;t) = \zeta + \frac{1}{18\zeta^9}\sin\frac{2\pi t}{T} + \frac{1}{20\zeta^{10}}\cos\big(\frac{2\pi t}{T}\big) \tag{7.20}$$

and $\overline{U}$, $\overline{\mathcal{P}}$ and E are:

$$\begin{aligned}
\overline{U} &= \frac{\pi R}{40T} \approx 7.8540\times 10^{-2}\frac{R}{T} \\
\overline{\mathcal{P}} &= \frac{19\pi^3\mu R^2}{45T^2} \approx 13.0915\frac{\mu R^2}{T^2} \\
E &= \frac{9}{6080\pi\mu} \approx 4.7118\times 10^{-4}\frac{1}{\mu}
\end{aligned}$$

The energy optimized sequence of shape deformations is given by

$$w(\zeta;t) = \zeta + \frac{1}{\sqrt{9}+\sqrt{10}}\Big[\frac{1}{\sqrt{9}\zeta^9}\sin\big(\frac{2\pi t}{T}\big) + \frac{1}{\sqrt{10}\zeta^{10}}\cos\big(\frac{2\pi t}{T}\big)\Big] \tag{7.21}$$

and $\overline{U}$, $\overline{\mathcal{P}}$ and E are:

$$\begin{aligned}
\overline{U} &= \frac{3\pi R}{\sqrt{10}(19+6\sqrt{10})T} \approx 7.8485\times 10^{-2}\frac{R}{T} \\
\overline{\mathcal{P}} &= \frac{16\pi^3\mu R^2}{(19+6\sqrt{10})T^2} \approx 13.0643\frac{\mu R^2}{T^2} \\
E &= \frac{9}{160(19+6\sqrt{10})\pi\mu} \approx 4.7151\times 10^{-4}\frac{1}{\mu}
\end{aligned}$$

From these analytical and computational results, we may see that the swimming behaviors of performance and energy optimized shape deformations for each N are actually quite the same.

Now let us consider the $Var(\mathcal{P}) \sim E$ relation given by equation (7.5). Compare equation (7.2) with equation (7.8), to make a reasonable comparison, here we only consider shapes prescribed by

$$w(\zeta;t) = \zeta + \frac{1}{M}\Big[\frac{a_{N-1}\sin(\frac{2\pi t}{T})}{(N-1)\zeta^{N-1}} + \frac{a_N\sin(\frac{2\pi t}{T}+\varphi)}{N\zeta^N}\Big] \tag{7.22}$$

It is easy to obtain the following results by direct calculation:

$$\overline{U} = \frac{2\pi a_{N-1}a_N}{NM^2T^2}\int_0^T \sin(\frac{2\pi t}{T}+\varphi)\cos(\frac{2\pi t}{T})\,dt = \frac{\pi a_{N-1}a_N}{NM^2T}\sin\varphi \tag{7.23}$$

$$E = \frac{\sin^2\varphi}{8\pi\mu N^2M^2}\Big[\frac{1}{(N-1)a_N^2}+\frac{1}{Na_{N-1}^2}\Big]^{-1} \tag{7.24}$$

$$Var(\mathcal{P}) = \frac{1}{2}\overline{\mathcal{P}}^2 - \frac{128\pi^4\mu^2}{T^2}\frac{N}{N-1}\overline{U}^2 \tag{7.25}$$

Equations (7.23, 7.24) readily validate equations (7.6, 7.7). As for the $Var(\mathcal{P}) \sim E$ relation, recall that the efficiency is defined as $E = \overline{U}^2/\overline{\mathcal{P}}$, from equation (7.25) it is easily seen that $Var(\mathcal{P}) \to \infty$ naturally leads to $E \to 0$ in this case.

Chapter 8

Swimming Dictyostelium Amoebae

As mentioned in Chapter 1, to date most studies of cell swimming have been restricted to ciliated motions. A lot has been done for cells with a fixed shape and coated with a thin layer of cilia. By coordinately propagating waves of the cilia, the cell propels itself through the fluid. For detailed discussion of ciliated motions of spherical and cylindrical cells we refer to [29, 30], and for that of elliptical cells we refer to [31]. In these literature, the authors use an asymptotic approach to solve the problem. However, such an approach necessarily requires that the shape deformations are small comparing to the length scale of the cell. Hence such an approach is not suitable for amoeboid cells swimming which involves large shape deformations.

In this Chapter we use the method developed in Chapter 6 to model swimming Dictyostelium amoebae. As we said earlier, introducing conformal mappings to describe the shapes of the cell allows us to obtain a large variety of shapes quickly. However, there exists a problem: how do we find the conformal mapping for an arbitrarily given shape? Unfortunately, for most arbitrarily given shapes it is difficult to figure out the corresponding conformal mapping. However any $2D$ contour can be approximated by an n-polygon, and for a polygon, the mapping problem can be solved by the *Schwarz-Christoffel formula*. Hence for a given sequence of shape changes of a cell, we may first use a sequence of n-polygons to approximate them and then truncate the Laurent

expansion of the conformal mappings leaving only finitely many terms, on which we could finally apply the algorithm developed in Chapter 6.

This Chapter is organized as follow: in Section 8.1 we briefly introduce the Schwarz-Christoffel formula; in Section 8.2 we model swimming Dictyostelium amoebae, and in Section 8.3 and Section 8.4 we discuss how different cell shapes affect the swimming behaviors of the cell.

8.1 Schwarz-Christoffel formula

Suppose that we have an n-polygon Γ in the z-plane with vertices $z_1, \cdots, z_n$, and the corresponding exterior angles are $\theta_1, \cdots, \theta_n$. Let Ω be the interior region bounded by Γ. The conformal mapping from the exterior of the unit disk D in the ζ-plane to Ω^c is given by the following Schwarz-Christoffel (SC) formula [68, 73]:

$$z = w(\zeta) = A + C \int^{\zeta} \frac{1}{\xi^2} \prod_{k=1}^{n} \left(\xi - \zeta_k\right)^{\theta_k - 1} d\xi \tag{8.1}$$

where $z_k = w(\zeta_k)$ and we call ζ_k the *prevertex* to the vertex z_k under the conformal mapping f, as shown in Figure 8.1. Also, the angles should satisfy the following condition:

$$\sum_{k=1}^{n} \theta_k = n + 2$$

In general for an arbitrary polygon, it is impossible to calculate the prevertices analytically, and we obtain them numerically using the SC toolbox from

http://www.math.udel.edu/~driscoll/SC/

To fully solve a 2D low Reynolds number swimming problem, we may follow the following steps:

1. use the Schwarz-Christoffel formula to obtain the conformal mapping $w(\zeta; t)$ of the sequence of n-polygons that approximates the objective sequence of shapes;

2. truncate the Laurent expansion of the conformal mapping $w(\zeta; t)$ obtained from the first step after $(-N)$-th order so that we obtain a sequence of finitely many terms conformal mapping $w_N(\zeta; t)$;

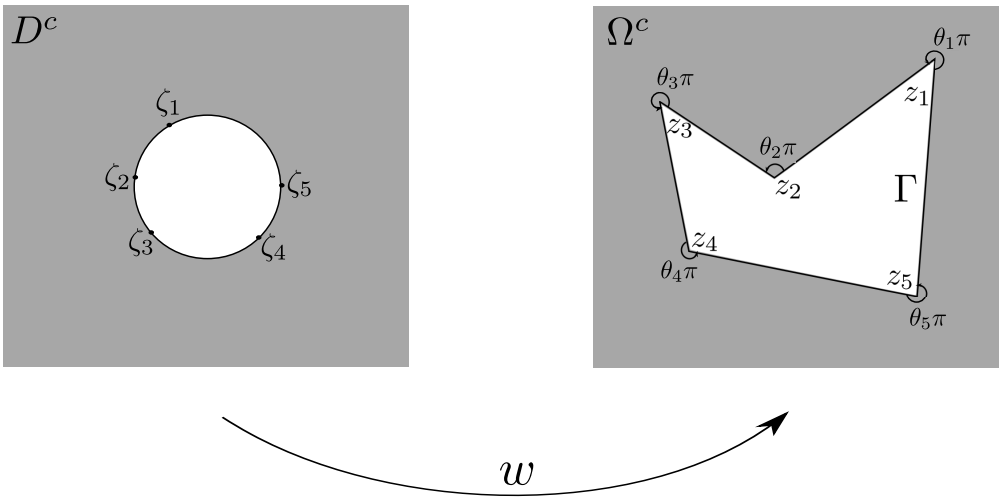

Figure 8.1: Conformal mapping for the exterior region of a polygon from that of the unit disk.

3. apply Proposition 5 developed in Chapter 6 to $w_N(\zeta;t)$ and solve the swimming problem.

However notice that there exists a problem in applying Proposition 5 to the conformal mapping $w_N(\zeta;t)$ obtained from the first two steps: we need to ensure the existence of the function f_N as introduced in Proposition 5. That is to say, there should not be any zero of $\overline{w'_N}(\zeta)$ inside the unit disk D, where

$$\overline{w'_N}(\zeta) = \overline{w'_N(\bar{\zeta})} = \overline{\alpha_1} - \overline{\alpha_{-1}}\zeta^2 - 2\overline{\alpha_{-2}}\zeta^3 - \cdots - N\overline{\alpha_{-N}}\zeta^{N+1}$$

and the α_j's are the coefficients of w_N as given in equation (6.1). Previously in Chapter 7 we require equation (7.1) so as to exclude all zeros of $\overline{w'(\sigma)}$ from the unit disk. However, this condition appears to be too strong and as a result it restricts the shape deformations to small ones around a disk for larger N as discussed in Chapter 7.

To overcome this obstacle, observe that from equation (8.1)

$$w'(\zeta) = \frac{C}{\zeta^2}\prod_{k=1}^{n}(\zeta-\zeta_k)^{\theta_k-1}$$

Thus the zeros of $w'(\zeta)$ only come from the prevertices that lie along the unit circle as shown by ζ_k's in Figure 8.1, and hence the same is true for $\overline{w'}(\zeta)$. When we truncate

the Laurent expansion of $w(\zeta)$ to $w_N(\zeta)$ leaving only finitely many lower order terms, such truncation will result in that the zeros of $\overline{w'_N}(\zeta)$ distribute near the unit circle. Then we slightly increase the amplitude of C in equation (8.1), which is the coefficient of the leading order term in w'_N and hence we move all zeros of $\overline{w'_N}(\zeta)$ outside the unit disk.

8.2 Modeling of swimming Dictyostelium amoebae

As we discussed in Chapter 1, recently it was found that Dictyostelium amoebae can swim by rapid shape changes without attaching to any substratum. In such processes usually the cell body is elongated, and multiple protrusions moving rapidly from the front to the rear of the cells are observed: in [1] an average of three protrusions are reported, as illustrated by the cartoon model in Figure 8.2 (a); while from Figure 8.2 (b) which was originally from [2] showing the swimming process of a typical swimming Dictyostelium, we see that one bump travels along one side of the cell and disappears at the rear of the cell, then another protrusion appears on the other side and repeats the same process.

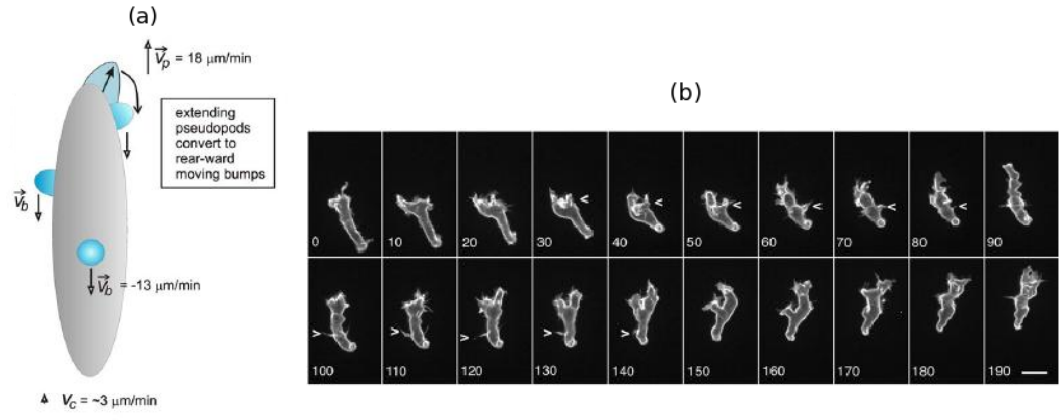

Figure 8.2: Amoebae swim by protrusions: (a) a swimming cell with 3 protrusions [1]; (b) the shape of an amoeboid as it swims [2].

In our modeling of such swimming mode by traveling protrusions, to reduce the analytical and computational efforts, we start from symmetric shape deformations by

considering a slender cell body in the plane with 2 protrusions moving to the rear of the cell simultaneously. To build up the geometry of the amoeboid, first we prescribe a sequence of polygons as the "inner skeletons", as shown by the blue contours in Figure 8.3, where the regions enclosed by the polygons are cross-like, and we use semi-circles at the ends of the crosses and each semi-circle is approximated by five line segments. Then we use the SC formula to obtain the conformal mappings to these "inner skeletons". Moreover, as explained in Section 8.1, we move the contour outward a small amount so as to exclude the zeros of $\overline{w_N'}(\zeta)$ from the unit disk and hence the existence of the function f_N is guaranteed. The black contours in Figure 8.3 show the images of the unit circle under the conformal mapping $w_N(\zeta;t)$, where we take $N = 15$.

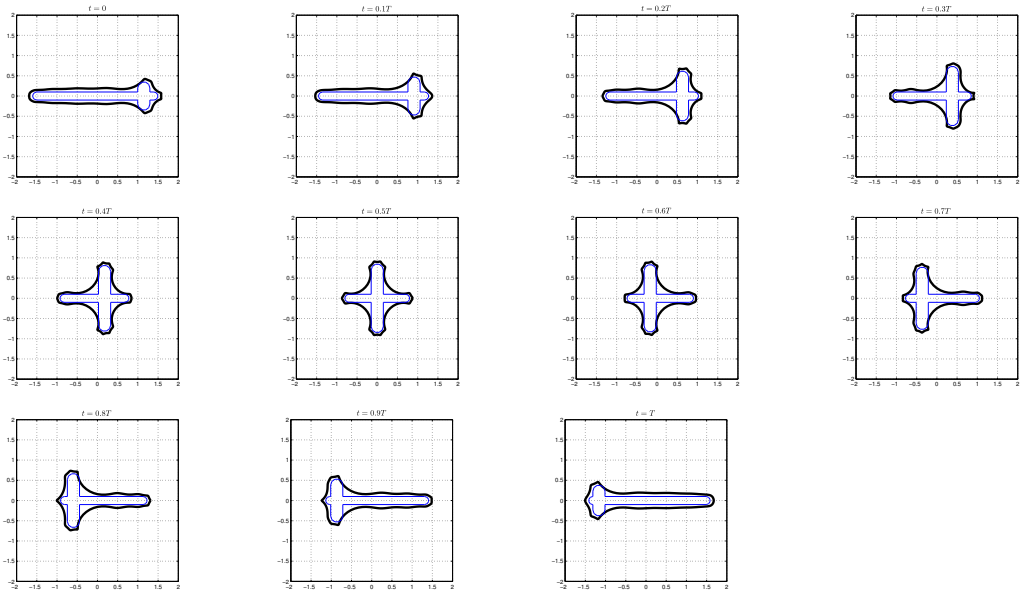

Figure 8.3: Illustration of building up the geometry of the swimming amoeboid model: the blue contours give the "inner skeletons" and the black contours give the images of the unit circle under $w_N(\zeta;t)$ with $N = 15$.

Moreover, in our modeling of swimming amoebae we do not require strict area conservation, instead we require that the area changes are restricted within a small range. Within one period, we define the ratio of area change to be:

$$\text{Ratio of area change} = \frac{\text{Maximum of area} - \text{Minimum of area}}{\text{Average of area}}$$

We require that the ratio ≤ 0.1.

We use the data for swimming amoebae from [1, 2], and for simplicity we will refer to them as "Haastert's cell" (Figure 8.2 (a)) and "Barry's cell" (Figure 8.2 (a)) from now on.

8.2.1 Haastert's cell

First let us consider Haastert's cell. As we said earlier, instead of three protrusions moving one by one along a $3D$ slender body as illustrated in Figure 8.2 (a), we design our model as a slender $2D$ body with two protrusions moving simultaneously so to preserve the symmetry. We collect the data from [1] as shown in Table 8.1.

Table 8.1: Experimental data for Haastert's cell [1].

Maximum cell body length:	$\sim 25\mu m$
Average cell body width:	$\sim 6\mu m$
Maximum protrusion height:	$\sim 2\mu m$
Average protrusion width:	$\sim 2\mu m$
Period:	$\sim$ 1min

We generate a sequence of inner skeletons based on data given in Table 8.1, from which we obtain sequences of finitely many terms conformal mappings $w_N(\zeta; t)$ as explained in Section 8.1 for $N = 10, 20, 40, 60, 80$. The numerical results are recorded in Table 8.2. Figures 8.4 (a) - (e) show the shape changes within one period (= 1min) for different N, the circles in the center mark the centers of the cell at each time step, from which we could observe the cell's translation. Figure 8.4 (f) shows the power changes within one period.

8.2.2 Barry's cell

Next we turn to the modeling of Barry's cell as shown in Figure 8.2 (b). There is no detailed data given for the cell's sizes in [2], and we estimate the data from Figure 8.2 (b) as listed below in Table 8.3.

As in the modeling of Haastert's cell, we also assume two symmetric protrusions on both sides of the $2D$ cell body. Comparing Table 8.1 and Table 8.3, we see that Barry's cell is more slender and with higher protrusions. Since we have larger protrusions here, we try to include the process of the protrusions generating at the front of the cell body

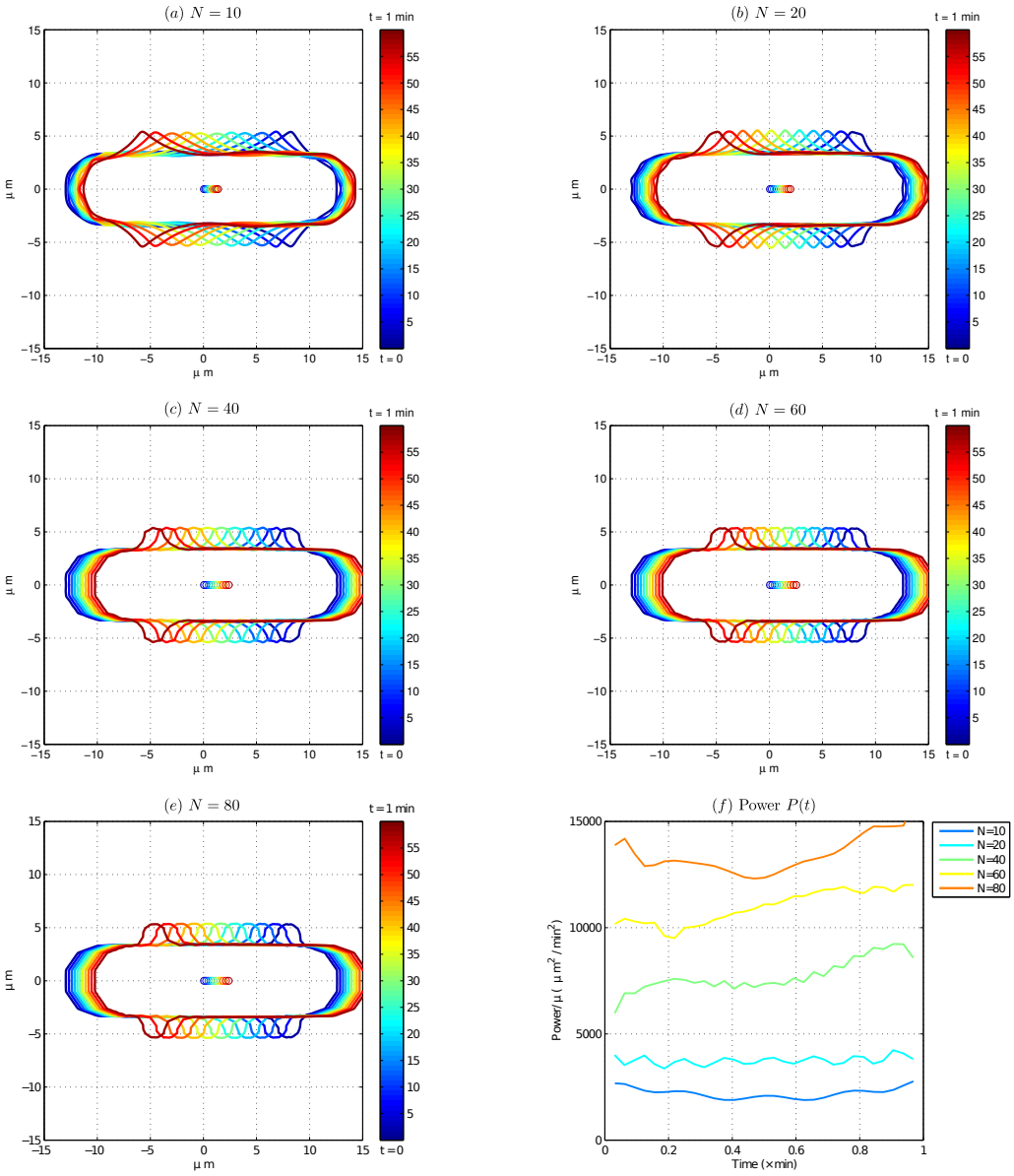

Figure 8.4: (a) - (e) Swimming of Haastert's cell for different N. (f) Power $\mathcal{P}(t)$ of Haastert's cell for different N.

Table 8.2: Numerical results for Haastert's cell.

Haastert	$N = 10$	$N = 20$	$N = 40$	$N = 60$	$N = 80$
Mean velocity (μm/min)	1.36	1.97	2.38	2.52	2.37
Mean power ($\mu \times \mu m^2/\text{min}^2$)	2209.59	3757.70	7649.91	10967.88	13446.66
Variance of power ($\mu^2 \times 10^4 \mu m^4/\text{min}^4$)	5.71	3.72	55.98	59.83	76.85
Efficiency ($\mu^{-1} \times 10^{-4}$)	8.39	10.36	7.40	5.80	4.2
Ratio of area change	0.0075	0.0033	0.0012	0.0017	0.0017
Average area (μm^2)	173.87	172.38	171.21	170.84	170.69

Table 8.3: Experimental data for Barry's cell [2].

Maximum cell body length:	$\sim 22\mu m$
Average cell body width:	$\sim 4\mu m$
Maximum protrusion height:	$\sim 4\mu$
Average protrusion width:	$\sim 2\mu m$
Period:	$\sim$ 1.5min

and later disappearing at the rear in our models as well. Unlike in the modeling of Haastert's cell where we keep the protrusion heights as a constant, here we allow the protrusion heights to change so to model the growing and disappearing processes of the protrusions. Meanwhile, we change the length of the cell body so as to compensate the volume change caused by the change of protrusion heights.

Finally we would like to make another comment of the period of shape changes. Originally the period is defined as a full cycle which ends up with the identical starting shape. According to such definition, observe Figure 8.2 (b) and it should be $T \sim 3$min. However since here we assume two symmetric protrusions instead of only one on one side of the cell body as shown in Figure 8.2 (b), to keep accordance with this symmetry assumption we take $T = 1.5$min.

As illustrated in the modeling of Haastert's cell, we generate a sequence of inner

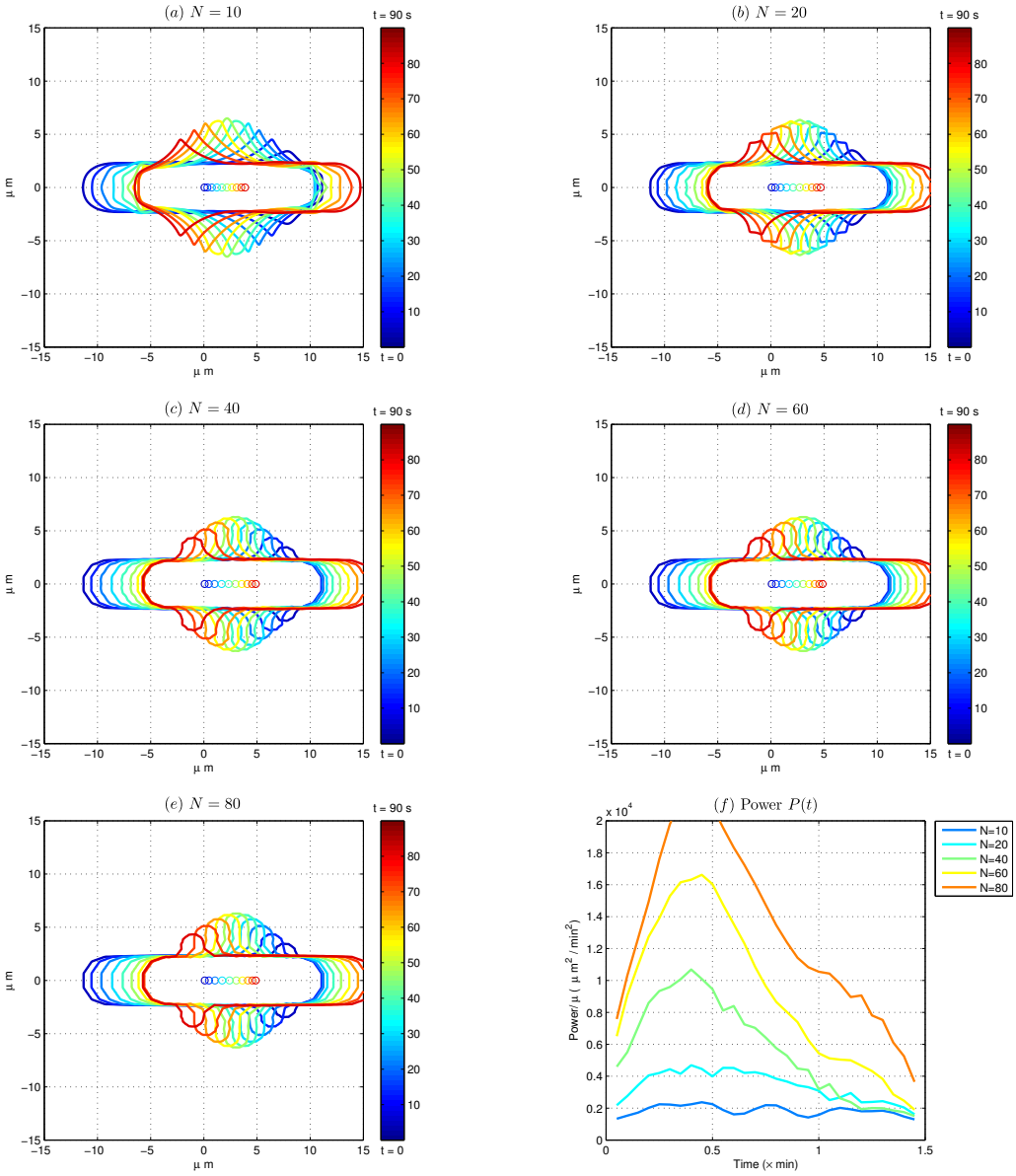

Figure 8.5: (a) - (e) Swimming of Barry's cell for different N. (f) Power $\mathcal{P}(t)$ of Barry's cell for different N.

skeletons based on data given in Table 8.3, then we obtain sequences of finitely many terms conformal mappings $w_N(\zeta;t)$ as explained in Section 8.1 for $N = 10, 20, 40, 60, 80$. The numerical results are recorded in Table 8.4. Figures 8.5 (a) - (e) show the shape changes within one period (= 1.5min) for different N, with circles in the center marking the centers of the cell at each time step. Figure 8.5 (f) shows the power changes within one period.

Table 8.4: Numerical results for Barry's cell.

Barry	$N = 10$	$N = 20$	$N = 40$	$N = 60$	$N = 80$
Mean velocity (μm/min)	2.63	3.18	3.31	3.29	3.30
Mean power ($\mu \times \mu m^2/\text{min}^2$)	1852.41	3396.66	5686.09	9161.44	13155.73
Variance of power ($\mu^2 \times 10^4 \mu m^4/\text{min}^4$)	8.87	80.72	895.60	2194.40	2774.47
Efficiency ($\mu^{-1} \times 10^{-4}$)	37.46	29.72	19.24	11.84	8.29
Ratio of area change	0.015	0.023	0.0044	0.0019	0.0041
Average area (μm^2)	103.61	105.35	103.91	103.42	103.18

8.2.3 Conclusions

Below we present our observations and conclusions from numerical simulations in Section 8.2.1 and Section 8.2.2.

1. First let us consider how the number of terms N in the conformal mappings w_N effects the shapes of the swimmers. From Figures 8.4 (a) - (e) and Figures 8.5 (a) - (e), we see that swimmers corresponding to w_N with larger N have more rounded heads in the protrusions, while those corresponding to w_N with smaller N tend to have sharper heads; another important difference in the shapes of the protrusions is that the connecting parts between the cell body and the protrusions are smoother for smaller N while more abrupt for larger N. To provide a better

visualization of these differences, we show the enlarged view of the bump areas in both models with different N in Figure 8.6.

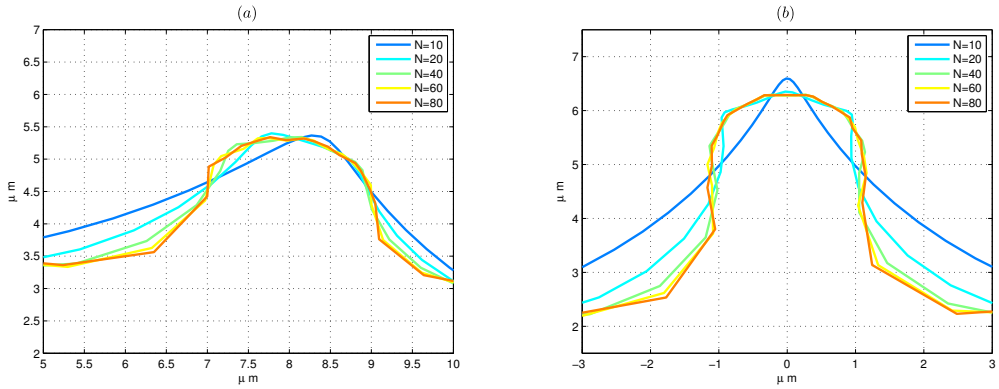

Figure 8.6: Bump areas in the models of Haastert's and Barry's cells for different N: (a) Haastert's cell; (b) Barry's cell.

2. Observing the mean velocity of both cells, we see that for small N, the mean velocity within one period increases as N increases. Yet after some point the mean velocity seems to reach a supreme: from Table 8.2 and Table 8.4 we see that for $N \geq 40$, the mean velocity of Haastert's cell fluctuates within a range $2.37-2.52\mu m/\text{min}$ while for Barry's cell the mean velocity $\sim 3.30\mu m/\text{min}$. Taking into account of our last conclusion for the relation between N and protrusion shapes, our observation for the mean velocity from both models indicates that abrupt protrusions with rounded heads may enhance the swimming speed.

3. For power expenditure, either from Figure 8.4 and Figure 8.5 or Table 8.2 and Table 8.4, we see that the power keeps increasing as N increases. Especially notice from Figure 8.6 that for $N = 60$ and $N = 80$ the shapes of the protrusions are quite similar to each other, which means that for approximating the desired shapes $N = 60$ should be enough, while from Figure 8.4 and Figure 8.5 we see that the power $\mathcal{P}(t)$ behaves quite differently for $N = 60$ and $N = 80$ in both models. Hence naturally a problem arises here: how do we guarantee the convergence of power in the algorithm as described in Section 8.1? So far we do not have a definite answer, yet it is true that power should always converges slower than shapes and translations. For further discussion related to this convergence problem, please

refer to Section 9.2.

4. For efficiency, from Table 8.4 we see that in the modeling of Barry's cell, the efficiency decreases as N increases, while from Table 8.2, for the Haastert's cell the efficiency reaches its maximum at around $N = 20$ and then decreases as N increases. Comparing with the first two conclusions, we find that smoother protrusions tend to lead to more efficient swimming though it might be slower. Moreover, if we compare the variance of power $Var(\mathcal{P})$ and the efficiency E as recorded in Table 8.2 and Table 8.4 we see that there is a reversed relation between $Var(\mathcal{P})$ and E, which coincides with the $Var(\mathcal{P}) \sim E$ relation as given by equation (7.5).

5. Now we compare our simulation results with the original experimental data from [1, 2]. It is reported in [1] that the swimming velocity of a typical Haastert's cell is $\sim 3\mu m/\text{min}$, while our model predicts $\sim 1.36 - 2.52\mu m/\text{min}$. Taking into account that in [1] an average of ~ 3 protrusions are observed while in our model we assume only 2 protrusions, our model works well here. As for Barry's cells, it is reported in [2] that the linear speed of the cells has a range of $2 - 8.4\mu m/\text{min}$ with an average of about $4.2\mu m/\text{min}$, comparing to a range of $\sim 2.63 - 3.31\mu m/\text{min}$ as predicted in our model. Yet considering that the cell has only 1 protrusion along one side of the cell body as shown in Figure 8.2 (b), the prediction of our model appears to be a little slow. However since the shape changes shown in Figure 8.2 (b) is more complicated than those in our simplified model, we claim that our prediction is still reasonable. Yet to fully understand the complicated swimming behavior of these cells we need more mature mathematical models.

6. Finally let us have a comparison between these two cells. Keep in mind that actually they are the same kind of Dictyostelium amoebae just there sizes are a little different. As we mentioned earlier, comparing to Haastert's cell, Barry's cell is more slender and with higher protrusions, and such difference leads to faster and more efficient swimming as can be seen either from the original data from [1, 2] or from our numerical results listed in Table 8.2 and Table 8.4. This inspires us to study how the sizes of the cell body and the protrusions affect the swimming behavior of the cell, which will be discussed in detail in Section 8.3 and Section 8.4.

8.3 Effects of the protrusion height to swimming

In this section we study the effects of the protrusion shape — more specifically the protrusion's height — to the swimming behavior of the Dictyostelium amoebae. We consider cells with fixed cell body shape and protrusions with fixed width, but allow heights of the protrusions to change.

First we use the data of maximum cell body length ($\sim 25\mu m$), average cell body width ($\sim 6\mu m$), average protrusion width ($\sim 2\mu m$) and period ($\sim$ 1min) for Haastert's cell as listed in Table 8.1. We still assume two protrusions generating at the front of the cell and moving simultaneously towards the rear of the cell body. As for the conformal mappings, we truncate them to $N = 30$ so as to provide us with protrusions that are neither too smooth nor too abrupt. Moreover, we change the cell body length at each time step so to compensate the area changes caused by the growing and disappearing of the protrusions and control the area change of the whole cell within a small range. Next we use the data of maximum cell body length ($\sim 22\mu m$), average cell body width ($\sim 4\mu m$), average protrusion width ($\sim 2\mu m$) and period ($\sim$ 1.5min) for Barry's cell as listed in Table 8.3. The assumption of protrusions and the order of the conformal mappings are the same as for Haastert's cell. We also change the cell body length at each time step so as to control the area change.

We test both models for different maximum protrusion heights, ranging from $1.5\mu m - 6\mu m$. In Figure 8.7 we depict the relation of mean velocity, mean power, efficiency to the maximum protrusion height for both Barry's and Haastert's cells, from which we see that in both models, all of mean velocity, mean power, efficiency increase as the maximum protrusion height increases.

At this point we would not make any further comparison between Barry's cell and Haastert's cells based on Figure 8.7, since Haastert's cell adopt faster shape changes than Barry's cell — it takes 1 min for Haastert's cell to complete a full cycle while 1.5 min for Barry's. Moreover, the sizes of the cells are quite different: according to Table 8.2 and Table 8.2, Haastert's cell has an average area $\sim 172\ \mu m^2$ comparing to $\sim 104\ \mu m^2$ to Barry's cell. Hence direct comparison between these two models based on the results from Figure 8.7 is not reasonable. For detailed discussion about how the shapes of cell body effect the swimming behavior, we refer to Section 8.4.

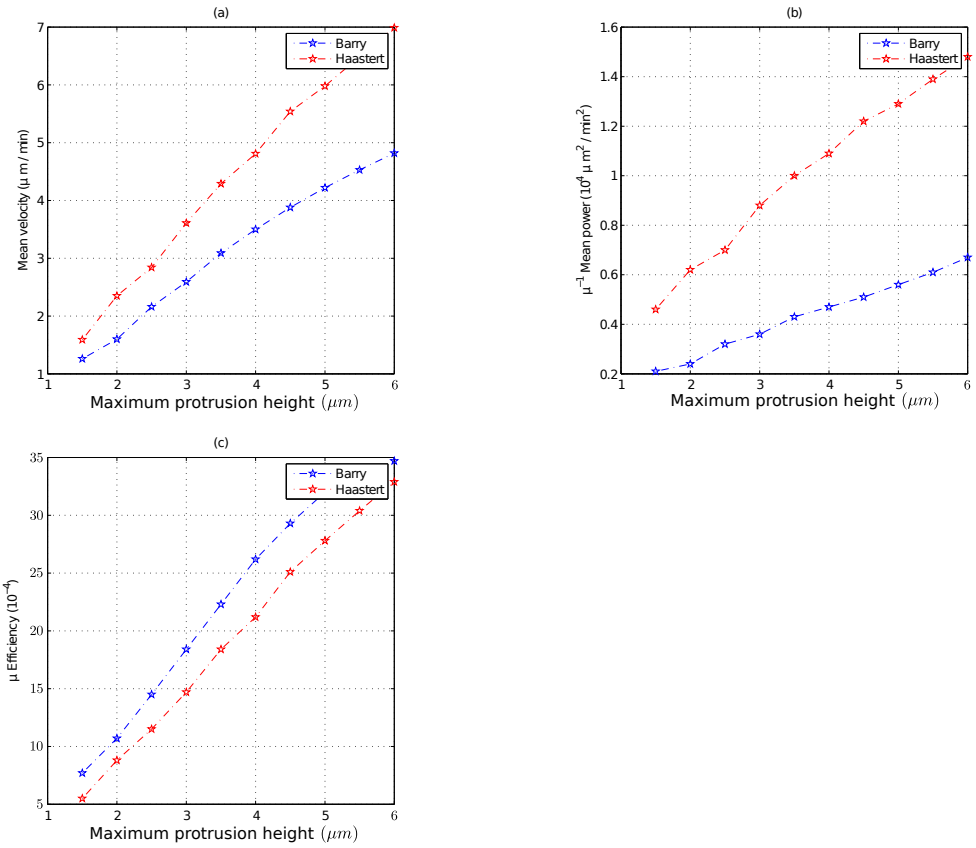

Figure 8.7: Effects of the protrusion height to swimming (I), for Haastert's and Barry's cell: (a): mean velocity $\sim$ maximum protrusion height; (b): mean power $\sim$ maximum protrusion height; (c): efficiency $\sim$ maximum protrusion height.

Moreover, we design another numerical experiment in which we consider a cell with very slender cell body and protrusions with height ranging from $2\mu m - 11\mu m$. In Table 8.5 we list the data used for this numerical experiment. As usual, we truncate the conformal mappings to $N = 30$. The experiment involves protrusions with extremely large heights. Although such monsters are not realistic from biology, they provide us with a better understanding of the relations between the protrusion heights and the swimming behavior.

Table 8.5: Data for testing the effects of the protrusion height to swimming.

Maximum cell body length:	$\sim 32\mu m$
Average cell body width:	$\sim 3\mu m$
Average protrusion width:	$\sim 2\mu m$
Number of protrusions:	2
Period:	$\sim$ 1min

In Figure 8.8 we depict the relations of mean velocity, mean power and efficiency to the maximum protrusion height. From Figure 8.8 (a), we see that the mean velocity increases as the maximum protrusion height increases, yet after certain point (maximum protrusion height $\sim 3\mu m$) the acceleration decreases. If such trend continues then there might be a maximum for the mean velocity. For the mean power, from Figure 8.8 (b) we see that it also increases as the maximum protrusion height increases. The acceleration behavior is more complicated, at this point we would not make any conclusion here. Finally from Figure 8.8 (c), we see that the efficiency first increases and reaches its maximum at maximum protrusion height $\sim 9\mu m$ then decreases.

Such behaviors do not show up in the models for Haastert's and Barry's cells, as can be seen from Figure 8.7. This might be because that here we are considering a cell more slender than both Haastert's and Barry's cells and with protrusions with extremely large heights. However if we observe Figure 8.7 (a) and (c) carefully, we do see that the accelerations for mean velocity and efficiency start to decrease at some point, which coincides with our observation in Figure 8.8 (a) and (c).

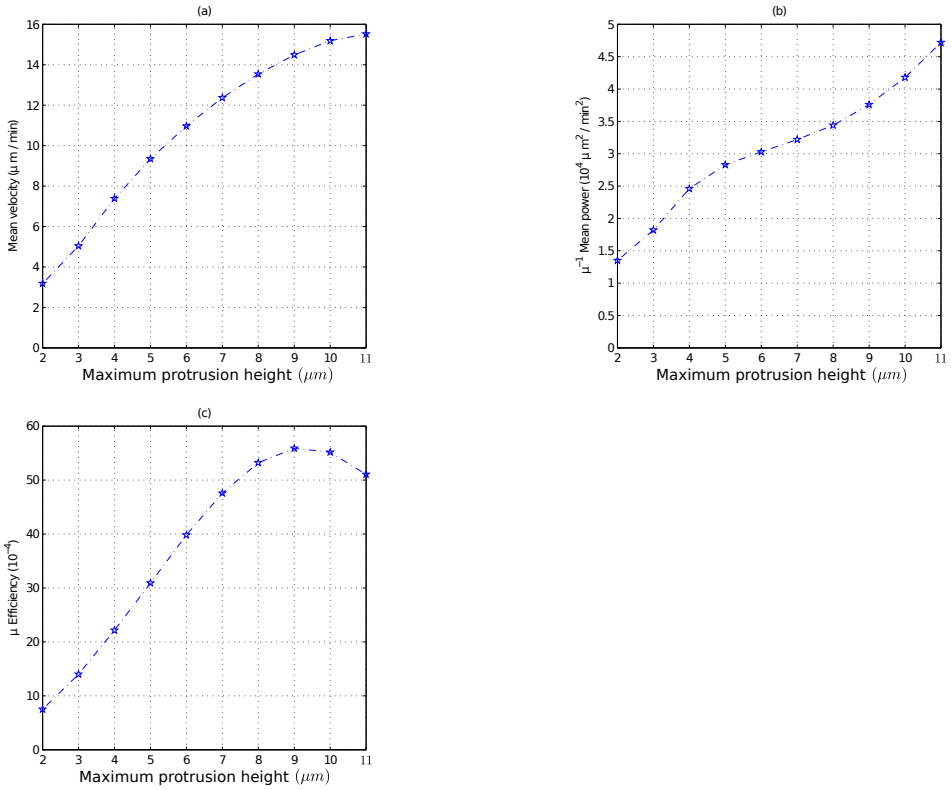

Figure 8.8: Effects of the protrusion height to swimming (II): (a): mean velocity $\sim$ maximum protrusion height; (b): mean power $\sim$ maximum protrusion height; (c): efficiency $\sim$ maximum protrusion height.

8.4 Effects of cell body shapes to swimming

Finally we consider the effects of the cell body shape to the swimming behaviors of Dictyostelium amoebae. We test cell bodies with different length and width. In our modeling, We consider protrusions with same height ($\sim 3\mu m$) and width ($\sim 2\mu m$) and let the shape deformations have the same period (= 1min). Moreover, to reduce the computational effort we keep the protrusion height to be a constant through the whole cycle, namely we do not consider the generating, growing and disappearing processes of the protrusions. Moreover, to make the comparison fair, we try to control the average area of each cell within a certain range ($\sim 176 - 205\mu m^2$).

Define the ratio of the cell body sizes R_s to be:

$$R_s = \frac{\text{Cell body length}}{\text{Cell body width}}$$

It is easily seen that large R_s corresponds to slender bodies while small R_s corresponds to rounded ones. Below in Table 8.6 are the numerical data for the cells' shapes. In Figure 8.9 we depict the relations of mean velocity, mean power and efficiency to the ratio of the cell body sizes R_s.

Table 8.6: Data for testing the effects of cell body shapes.

R_s:	10.09	8.12	6.71	5.67	4.88	4.26
Cell body length (μm):	40.36	36.55	33.57	31.20	29.29	27.72
Cell body width (μm):	4	4.5	5	5.5	6	6.5
Average area (μm^2):	204.86	198.29	193.48	189.72	186.70	184.28
Ratio of area change:	0.0025	0.0015	0.0020	0.0026	0.0020	0.0014
R_s:	3.78	3.38	3.06	2.79	2.57	2.38
Cell body length (μm):	26.43	25.36	24.47	23.72	23.10	22.58
Cell body width (μm):	7	7.5	8	8.5	9	9.5
Average area (μm^2):	182.33	180.75	179.39	178.17	177.02	174.98
Ratio of area change:	0.0016	0.0013	0.0013	0.0013	0.0018	0.0015

From Figure 8.9 we see that slender cells swim faster than rounded ones, yet they require more power expenditure and are less efficient.

As a summary to Section 8.3 and Section 8.4, we conclude that:

1. Within a reasonable range, protrusions with large height will result in faster and more efficient swimming;

2. slender cells swim faster yet are less efficient than those rounded ones.

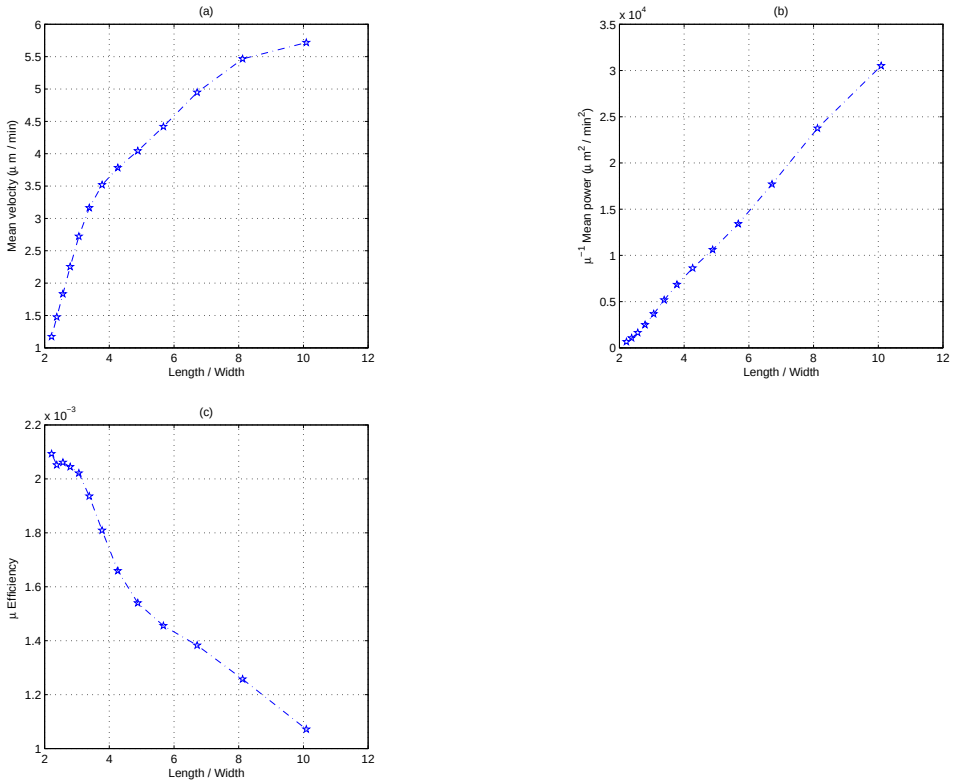

Figure 8.9: Effects of cell body shapes to swimming: (a): mean velocity $\sim R_s$; (b): mean power $\sim R_s$; (c): efficiency $\sim R_s$.

Chapter 9

Future Work

9.1 Linked spheres models in LMV flows

As we mentioned in Chapter 4, we want to apply the linked spheres model as introduced in Chapter 2 to LMV flows so to study the effects of viscoelasticity. Chapter 4 serves as a starting point that provides the fundamental analytical framework. Next step we apply the linear 3-spheres model in Chapter 2 to LMV flows, apply numerical simulations to certain prescribed loops, and compare the results with those in Chapter 2 based on the criteria given by equations (4.6, 4.22).

Moreover, we hope to obtain certain analytical results for more complicated shape changes in an LMV fluid. In Chapter 4 we considered translating spheres that can be deformable in the radial direction only. Next we may consider translating and deformable models whose shapes keep axial or cylindrical symmetry, as shown by Figure 9.1. Now the boundary Γ of the swimmer is determined by the radius R at x: $R = R(x;t)$. If we do not consider membrane flows, than the boundary condition can be written as:

$$\mathbf{u}(x,t) = \frac{\partial}{\partial t} R(x;t)\mathbf{e}_r + U(t)\mathbf{e}_z \tag{9.1}$$

9.2 Convergence problems in 2D swimming

As mentioned in Section 8.2.3, from Figure 8.4 (f) and Figure 8.5 (f) we see that the power keeps increasing as N increases. In fact not only for power, for all physical

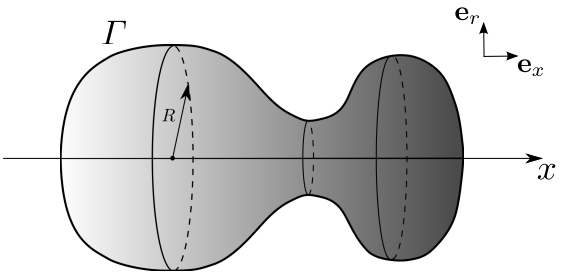

Figure 9.1: Shape with axial symmetry

quantities listed in Section 5.4 we need to verify their convergence when we truncate the Laurent expansions of the conformal mappings. Below we express the convergence problems of translation and power in mathermatical terms.

Suppose that at time t, the shape of the cell and the velocity boundary condition are described as $w(\zeta)$ and $V(\sigma)$. The corresponding translational velocity and power of the cell at time t are $-A^{\mathrm{tr}}$ and $\mathcal{P}$

1. *Convergence of translation:* $\forall\ \varepsilon_{\mathrm{tr}} > 0$, does there necessarily exist an $N_{\mathrm{tr}} \in \mathbb{Z}^+$ such that $\forall\ n > N_{\mathrm{tr}}$, when we truncate the Laurent expansion of w and V after $(-n)$-th order leaving finitely many terms w_n and V_n, we always have

$$\left| A^{\mathrm{tr}} - A_n^{\mathrm{tr}} \right| < \varepsilon_{\mathrm{tr}}$$

   where $-A_n^{\mathrm{tr}}$ is the translational velocity corresponding to the shape given by w_n with velocity boundary condition V_n?

2. *Convergence of power:* $\forall\ \varepsilon_{\mathcal{P}} > 0$, does there necessarily exist an $N_{\mathcal{P}} \in \mathbb{Z}^+$ such that $\forall\ n > N_{\mathcal{P}}$, when we truncate the Laurent expansions of w and V after $(-n)$-th order leaving finitely many terms w_n and V_n, we always have

$$\left| \mathcal{P} - \mathcal{P}_n \right| < \varepsilon_{\mathcal{P}}$$

   where $\mathcal{P}_n$ is the power corresponding to the shape given by w_n with velocity boundary condition V_n?

Finally we would like to make another comment here. Assume that both translation and power indeed converge, we have a natural guess that power converges slower than

shape or translation. This can be seen from equation (5.29) that $\pm n$-th order terms are weighted by n, i.e., higher order terms in the Laurent expansion of w play more important roles than those lower order terms though they must converge to zero because of the convergence of the conformal mapping w itself. This may explain that in Figure 8.4 and Figure 8.5 the power still behaves very differently while the shapes seem to be quite similar.

9.3 General shape deformations

Though we discussed a little about rotation in Section 5.4.1, all of our numerical simulation in Chapter 7 and Chapter 8 are restricted to symmetric shape deformations only, where there is no rotation involved. Naturally the next step would be to bring in rotation, from which we could greatly extend the application of the method we have built up. For example, it will enable us to analyze the swimming behavior of Dictyostelium amoebae as shown in Figure 8.2.

Since our method relies highly on the conformal mappings, so far it only applies to 2D problem. We seek a way to allow us approach 3D problems. Certainly there are existing numerical methods dealing with 3D Stokes flows, for example, the *boundary integral methods* [67]. Yet we want a way that inherited from our 2D framework which allows us quickly generating and dealing with a large variety of shapes. A reasonable start point may be to substitute Laurent expansions by Fourier series.

References

[1] P.J.M. Haastert and N.A. Hotchin. Amoeboid cells use protrusions for walking, gliding and swimming.

[2] N.P. Barry and M.S. Bretscher. Dictyostelium amoebae and neutrophils can swim. *Proceedings of the National Academy of Sciences*, 107(25):11376, 2010.

[3] F. Binamé, G. Pawlak, P. Roux, and U. Hibner. What makes cells move: requirements and obstacles for spontaneous cell motility. *Mol. BioSyst.*, 6(4):648–661, 2010.

[4] M.P. Sheetz, D. Felsenfeld, CG Galbraith, D. Choquet, et al. Cell migration as a five-step cycle. In *Biochemical Society symposium*, volume 65, page 233, 1999.

[5] J.V. Small, T. Stradal, E. Vignal, and K. Rottner. The lamellipodium: where motility begins. *Trends in cell biology*, 12(3):112–120, 2002.

[6] G.G. Martins and J. Kolega. Endothelial cell protrusion and migration in three-dimensional collagen matrices. *Cell motility and the cytoskeleton*, 63(2):101–115, 2006.

[7] N.V. Mantzaris, S. Webb, and H.G. Othmer. Mathematical modeling of tumor-induced angiogenesis. *Journal of Mathematical Biology*, 49(2):111–187, 2004.

[8] SS Suarez and AA Pacey. Sperm transport in the female reproductive tract. *Human Reproduction Update*, 12(1):23–37, 2006.

[9] H.C. Berg and R.A. Anderson. Bacteria swim by rotating their flagellar filaments. 1973.

[10] G. Lowe, M. Meister, and H.C. Berg. Rapid rotation of flagellar bundles in swimming bacteria. 1987.

[11] IR Gibbons. Cilia and flagella of eukaryotes. *The Journal of cell biology*, 91(3):107s–124s, 1981.

[12] M.A. Sleigh, J.R. Blake, and N. Liron. The propulsion of mucus by cilia. *American Journal of Respiratory and Critical Care Medicine*, 137(3):726–741, 1988.

[13] T. Lämmermann and M. Sixt. Mechanical modes of amoeboidcell migration. *Current opinion in cell biology*, 21(5):636–644, 2009.

[14] K. Wolf, I. Mazo, H. Leung, K. Engelke, U.H. Von Andrian, E.I. Deryugina, A.Y. Strongin, E.B. Bröcker, and P. Friedl. Compensation mechanism in tumor cell migration. *The Journal of cell biology*, 160(2):267–277, 2003.

[15] P. Friedl, K. Wolf, et al. Tumour-cell invasion and migration: diversity and escape mechanisms. *Nature Reviews Cancer*, 3(5):362–374, 2003.

[16] T. Lämmermann, B.L. Bader, S.J. Monkley, T. Worbs, R. Wedlich-Söldner, K. Hirsch, M. Keller, R. Förster, D.R. Critchley, R. Fässler, et al. Rapid leukocyte migration by integrin-independent flowing and squeezing. *Nature*, 453(7191):51–55, 2008.

[17] H. Blaser, S. Eisenbeiss, M. Neumann, M. Reichman-Fried, B. Thisse, C. Thisse, and E. Raz. Transition from non-motile behaviour to directed migration during early pgc development in zebrafish. *Journal of cell science*, 118(17):4027–4038, 2005.

[18] H. Blaser, M. Reichman-Fried, I. Castanon, K. Dumstrei, F.L. Marlow, K. Kawakami, L. Solnica-Krezel, C.P. Heisenberg, and E. Raz. Migration of zebrafish primordial germ cells: a role for myosin contraction and cytoplasmic flow. *Developmental cell*, 11(5):613–627, 2006.

[19] G. Salbreux, JF Joanny, J. Prost, and P. Pullarkat. Shape oscillations of non-adhering fibroblast cells. *Physical biology*, 4:268, 2007.

[20] O.T. Fackler and R. Grosse. Cell motility through plasma membrane blebbing. *The Journal of cell biology*, 181(6):879–884, 2008.

[21] E. Paluch, M. Piel, J. Prost, M. Bornens, and C. Sykes. Cortical actomyosin breakage triggers shape oscillations in cells and cell fragments. *Biophysical journal*, 89(1):724–733, 2005.

[22] A.J. Bae and E. Bodenschatz. On the swimming of dictyostelium amoebae. *Proceedings of the National Academy of Sciences*, 107(44):E165–E166, 2010.

[23] J. Happel and H. Brenner. *Low Reynolds number hydrodynamics: with special applications to particulate media*, volume 1. Springer, 1983.

[24] H. Lamb and S.H. Lamb. *Hydrodynamics*. Cambridge Univ Pr, 1997.

[25] S. Kim and S.J. Karrila. *Microhydrodynamics*. Butterworth-Heinemann New York, 1991.

[26] S. Childress. *Mechanics of swimming and flying*, volume 2. Cambridge Univ Pr, 1981.

[27] E. Lauga and T.R. Powers. The hydrodynamics of swimming microorganisms. *Reports on Progress in Physics*, 72:096601, 2009.

[28] E.M. Purcell. Life at low reynolds number. *Am. J. Phys*, 45(1):3–11, 1977.

[29] A. Shapere and F. Wilczek. Geometry of self-propulsion at low reynolds number. *Journal of Fluid Mechanics*, 198(1):557–585, 1989.

[30] A. Shapere and F. Wilczek. Efficiencies of self-propulsion at low reynolds number. *J. Fluid Mech*, 198:587–599, 1989.

[31] A. Cherman, J. Delgado, F. Duda, K. Ehlers, J. Koiller, and R. Montgomery. Low reynolds number swimming in two dimensions. *Hamiltonian systems and celestial mechanics (Pátzcuaro, 1998)*, 6:32–62, 2000.

[32] F. Alouges, A. DeSimone, L. Heltai, A. Lefebvre, and B. Merlet. Optimally swimming stokesian robots. *Arxiv preprint arXiv:1007.4920*, 2010.

[33] F. Alouges, A. DeSimone, and L. Heltai. Numerical strategies for stroke optimization of axisymmetric microswimmers. *Arxiv preprint arXiv:0906.4502*, 2009.

[34] F. Alouges, A. DeSimone, and A. Lefebvre. Optimal strokes for low reynolds number swimmers: an example. *Journal of Nonlinear Science*, 18(3):277–302, 2008.

[35] F. Alouges, A. DeSimone, and A. Lefebvre. Optimal strokes for axisymmetric microswimmers. *The European Physical Journal E: Soft Matter and Biological Physics*, 28(3):279–284, 2009.

[36] J. Koiller, MA Raupp, J. Delgado, KM Ehlers, and R. Montgomery. Spectral methods for stokes flows. *Computational and Applied Mathematics*, 17:343–372, 1998.

[37] J. Koiller, K. Ehlers, and R. Montgomery. Problems and progress in microswimming. *Journal of Nonlinear Science*, 6(6):507–541, 1996.

[38] S.D. Kelly. *The mechanics and control of robotic locomotion with applications to aquatic vehicles*. PhD thesis, California Institute of Technology, 1998.

[39] S.D. Kelly and R.M. Murray. Geometric phases and robotic locomotion. *Journal of Robotic Systems*, 12(6):417–431, 1995.

[40] S.D. Kelly. The mechanics and control of driftless swimming. *To appear, SIAM Journal on Control and Optimization*, 2011.

[41] J. Lighthill. Flagellar hydrodynamics: the john von neumann lecture, 1975. *SIAM review*, pages 161–230, 1976.

[42] GJ Hancock. The self-propulsion of microscopic organisms through liquids. *Proceedings of the Royal Society of London. Series A. Mathematical and Physical Sciences*, 217(1128):96–121, 1953.

[43] RE Johnson and CJ Brokaw. Flagellar hydrodynamics. a comparison between resistive-force theory and slender-body theory. *Biophysical journal*, 25(1):113–127, 1979.

[44] RG Cox. The motion of long slender bodies in a viscous fluid part 1. general theory. *Journal of Fluid mechanics*, 44(04):791–810, 1970.

[45] GK Batchelor. Slender-body theory for particles of arbitrary cross-section in stokes flow. *Journal of Fluid Mechanics*, 44(03):419–440, 1970.

[46] J.B. Keller and S.I. Rubinow. Slender-body theory for slow viscous flow. *J. Fluid Mech*, 75(4):705–714, 1976.

[47] R.E. Johnson. An improved slender-body theory for stokes flow. *Journal of Fluid Mechanics*, 99(2):411–431, 1980.

[48] MJ Lighthill. On the squirming motion of nearly spherical deformable bodies through liquids at very small reynolds numbers. *Communications on Pure and Applied Mathematics*, 5(2):109–118, 1952.

[49] JR Blake. A spherical envelope approach to ciliary propulsion. *J. Fluid Mech*, 46(1):199–208, 1971.

[50] JR Blake. Self propulsion due to oscillations on the surface of a cylinder at low reynolds number. *Bull. Austral. Math. Soc*, 3:255–264, 1971.

[51] LE Becker, SA Koehler, and HA Stone. On self-propulsion of micro-machines at low reynolds number: Purcell's three-link swimmer. *Journal of fluid mechanics*, 490(1):15–35, 2003.

[52] JE Avron and O. Raz. A geometric theory of swimming: Purcell's swimmer and its symmetrized cousin. *New Journal of Physics*, 10:063016, 2008.

[53] A. Najafi and R. Golestanian. A simplest swimmer at low reynolds number: Three linked spheres. *Arxiv preprint cond-mat/0402070*, 2004.

[54] R. Golestanian and A. Ajdari. Analytic results for the three-sphere swimmer at low reynolds number. *Arxiv preprint arXiv:0711.3700*, 2007.

[55] GP Alexander, CM Pooley, and JM Yeomans. Hydrodynamics of linked sphere model swimmers. *Journal of Physics: Condensed Matter*, 21:204108, 2009.

[56] D.J. Earl, CM Pooley, JF Ryder, I. Bredberg, JM Yeomans, et al. Modeling microscopic swimmers at low reynolds number. *Journal of Chemical Physics*, 126(6):64703–64703, 2007.

[57] R. Dreyfus, J. Baudry, and HA Stone. Purcells rotator: mechanical rotation at low reynolds number. *The European Physical Journal B-Condensed Matter and Complex Systems*, 47(1):161–164, 2005.

[58] JE Avron, O. Kenneth, and DH Oaknin. Pushmepullyou: An efficient micro-swimmer. *New Journal of Physics*, 7:234, 2005.

[59] A. Najafi and R. Zargar. Two-sphere low reynold's propeller. *Arxiv preprint arXiv:1009.5817*, 2010.

[60] Q. WANG, J. HU, and H. OTHMER. Models of low reynolds number swimmers inspired by cell blebbing.

[61] N.I. Muskhelishvili and JMR Radok. *Some basic problems of the mathematical theory of elasticity*, volume 15. Cambridge Univ Press, 1953.

[62] JE Avron, O. Gat, and O. Kenneth. Optimal swimming at low reynolds numbers. *Physical review letters*, 93(18):186001, 2004.

[63] M.P. Curtis and E.A. Gaffney. The effects of linear maxwell viscoelasticity on linked sphere swimmers. In proceeding.

[64] J. Magnaudet and D. Legendre. The viscous drag force on a spherical bubble with a time-dependent radius. *Physics of fluids*, 10:550–554, 1998.

[65] L. Greengard, M.C. Kropinski, and A. Mayo. Integral equation methods for stokes flow and isotropic elasticity in the plane. *Journal of Computational Physics*, 125(2):403–414, 1996.

[66] T. Chambrion and A. Munnier. Locomotion and control of a self-propelled shape-changing body in a fluid. *Journal of Nonlinear Science*, 21(3):325–385, 2011.

[67] C. Pozrikidis. *Boundary integral and singularity methods for linearized viscous flow*. Number 8. Cambridge Univ Pr, 1992.

[68] L.V. Ahlfors. Complex analysis, international series in pure and applied mathematics, 1978.

[69] Fang Qiqin. *Complex analysis*. Peking Univ Press, 1996.

[70] J. Cima, A. Matheson, and W. Ross. The cauchy transform. *Quadrature Domains and Their Applications*, pages 79–111, 2005.

[71] Y.W. Sokhotskii. On definite integrals and functions used in series expansions. *St. Petersburg*, 1873.

[72] Z. Nehari. Conformal mapping. 1952.

[73] TA Driscoll and LN Trefethen. Schwarz-christoffel mapping, ser. *Cambridge Monographs on Applied Computational Mathematics. Cambridge, UK: Cambridge University Press*, 2002.